NANYANG TECHNOLOGICAL UNIVERSITY

DEVELOPMENT OF FABRICATION PROCESS FOR EMBEDDED STRUCTURE IN MULTI-LAYER LOW TEMPERATURE CO-FIRED CERAMICS (LTCC) USING SACRIFICIAL CARBON BY PROCESS MODELLING AND SIMULATION

TAN YEOW MENG

SCHOOL OF MECHANICAL & AEROSPACE ENGINEERING

NANYANG TECHNOLOGICAL UNIVERSITY

2013

DEVELOPMENT OF FABRICATION PROCESS FOR EMBEDDED STRUCTURE IN MULTI-LAYER LOW TEMPERATURE CO-FIRED CERAMICS (LTCC) USING SACRIFICIAL CARBON BY PROCESS MODELLING AND SIMULATION

TAN YEOW MENG

SCHOOL OF MECHANICAL & AEROSPACE ENGINEERING

A thesis submitted to the Nanyang Technological University
in partial fulfilment of the requirement for the degree of
Doctor of Philosophy

2013

ACKNOWLEDGEMENTS

I am deeply indebted to my supervisor, Prof. Lam Yee Cheong, for his guidance and motivation rendered to me during the course of study. I am grateful to Dr Wang Zhiping, Research Programme Director & Programme Manager, MMP (Microfluidic Manufacturing Programme) and Dr Albert Lu, Programme Manager, LAP (Large Area Processing), SIMTech, for their support and alignment of my job activities due to the part time nature of this study. Not forgetting my former colleague, Dr Khoong Ling Eng, for his valuable advice on the research scope and participation on various research activities.

I would also like to thank the Agency for Science, Technology and Research (A*Star) for the project funding as well as the sponsorship for my study. Last but not least, my family for their understanding and supports.

TABLE OF CONTENTS

ABSTRACT

The evolution of Low Temperature Co-fired Ceramics (LTCC) allows the realisation of high speed electronic devices based on a ceramics multilayer platform. Its unique layered lamination and ease of 3D structuring also extend its applications beyond electronics to the areas of microsystems. To realise 3D structure in LTCC, the forming of embedded structures is inevitable. However, achieving good quality embedded structures with tight dimensional tolerance and free of defects remains a challenge.

The most promising method for the fabrication of embedded structure is by employing sacrificial material to support the structure and to retain its dimensional accuracy from the lamination to the sintering processes. Carbon as the fugitive material is of particular interest as it gasifies directly from solid to gas phase under oxidizing environment and the reaction accelerates at high temperature. It is chemically simple and left no trace of residue if the burn-off is complete. However, the detailed process characterisation with respect to carbon burn-off, particularly under embedded condition, has not been established. It is important to understand the competing kinetics between carbon burn-off and LTCC densification such that the process parameters could be optimised for having defect free embedded structures and an efficient production cycle.

Experimental kinetic analysis on the carbon tape using thermal analysis was conducted. Catalytic carbon burn-off was observed for carbon embedded with LTCC. Solid-catalysed effect is significant and varies with different LTCC systems. For a valid burn-off evaluation when the fugitive carbon is used for embedded structure

fabrication, complete reaction rate parameters for the carbon burn-off has to be conducted under LTCC embedded conditions. Carbon embedded sample configuration for TGA analysis was prepared and conducted. The kinetic rate parameters which were determined by isoconversion method with fitted first order reaction model for the pre-exponential factor could best describe the burn-off process under the influence of LTCC catalysts.

Experimental sintering kinetic analysis was also conducted on HL2000, the LTCC system selected for the study. It is a self constrained LTCC system that shrinks predominantly in the Z-direction during sintering. This provides better dimensional control for structure formation. LTCC sintering involves complex viscous flow with low temperature glass phase as it infiltrates and wets the ceramic filler. Reactive sintering occurred in HL2000 with alumina filler to form a stable crystallized phase to achieve low dielectric loss and better mechanical properties. The sintering mechanism is complex. In this study, a simple thermokinetic approach using 1^{st} order solid-state reaction model was determined from the TMA curves. A single value of activation energy and pre-exponential factor were determined by linear regression for a fitted linear equation over the experimental data obtained from multiple heating rates and various LTCC configurations. The obtained activation energy of 250 - 256 kJ/mol is comparable with the reported data in the literature.

Physical phenomena were identified for carbon burn-off process for embedded structure fabrication in LTCC ceramics system. An axisymmetric 2D multi-component chemical reactions mass transport model, which is coupled with pore evolution of LTCC with relation to the sintering parameters with 2 computation regions, was

developed for process characterisation. Mass transport related constants were determined by either physical measurements or empirical relationships, and experimental validations of the model were conducted. Competing kinetic was observed at the firing profile of 20 K/min in a 3-layer LTCC embedded structure, with incomplete carbon burn-off. The process model was further demonstrated in a practical application of optimising firing profile to minimise the distortion for a ∅ 32mm large embedded air cavity. The deformation of the cavity achieved is 75 ± 41 μm over a span of 32 mm. This large embedded cavity of minimum distortion is a significant achievement which is not reported elsewhere.

This study has provided a good understanding of the physical implication of using carbon as a fugitive material for embedded structure in LTCC. It has established a model for process characterisation which will be useful for the development of new products and for product improvement. The successful deployment of the process model will greatly reduce the time required for experimental trials and will improve the product quality in term of dimensional and shape consistency and tolerance. In addition, the developed model could be used in other ceramics based production involving burn-off processes.

LIST OF PUBLICATIONS

L E Khoong, Y M Tan, Y C Lam, "Overview on fabrication of three-dimensional structures in multi-layer ceramic substrate", Journal of the European Ceramic Society, 30, 1973–1987, 2010.

L E Khoong, Y M Tan, Y C Lam, "Carbon burnout and densification of self-constrained LTCC for fabrication of embedded structures in a multi-layer platform", Journal of the European Ceramic Society, 29, 457–463, 2009.

L E Khoong, Y M Tan, Y C Lam, "Study of deformation and porosity evolution of low temperature co-fired ceramic for embedded structures fabrication", Journal of the European Ceramic Society, 29, 2737–2745, 2009.

Y M Tan, L E Khoong, Y C Lam, S C Tan, R Paramasivam, "Process Development for Realization of Embedded Structures in Multi-Layer Ceramics Platform using Carbon Fugitive Material", 10th EPTC, 982-987, 2008.

L E Khoong, Y M Tan, Y C Lam, and C W Lu, "Multi-layer Lamination of Embedded Channels in Low Shrinkage Ceramics based Platform", 9th EPTC, 552-526, 2007.

Y M Tan, L E Khoong, Y C Lam and C W Lu, "Integration of Glass Layer for Meso and Micro-System Applications", 9th EPTC, 206-210, 2007.

LIST OF FIGURES

LIST OF TABLES

NOMENCLATURE

a, b, c, d	Stoichiometric coefficients of carbon burn-off reaction
a_0, b_0, c_0, d_0	Stoichiometric coefficients related to chemical reaction at reference conditions
a_T, b_T, c_T, d_T	Stoichiometric coefficients related to chemical reaction at reacting conditions
d	Diameter of pore size, (m)
d_L	Diameter of pore size, LTCC, (m)
g	Gravitational acceleration, $\left(\frac{m}{s^2}\right)$
j_i	Diffusion mass flux of species *i* relative to mass average velocity, $\left(\frac{kg}{m^2 s}\right)$
k_c	Reaction rate constant for carbon burn-off, $\left(\frac{1}{s}\right)$
k_c^*	Apparent reaction rate constant, $\left(\frac{m^3}{kg.s}\right)$
k_e	Effective thermal conductivity of porous medium, $\left(\frac{W}{m.K}\right)$
k_g	Thermal conductivity of gas mixture, $\left(\frac{W}{m.K}\right)$
k_i	Thermal conductivity of gas species *i*, $\left(\frac{W}{m.K}\right)$
k_L	Reaction rate constant related to LTCC sintering, $\left(\frac{1}{s}\right)$
k_s	Thermal conductivity of solid matrix i.e. carbon or LTCC, $\left(\frac{W}{m.K}\right)$
$kn0$	Characteristic parameter of pore geometry, (m)
m_c	Instantaneous mass of carbon during burn-off, (kg)
n_d	Number of solid grains per unit volume of porous solid
n_i	Total mass flux, $\left(\frac{kg}{m^2 s}\right)$

r_g	Radius of grain size of porous medium, (m)
v	Mass average velocity, $\left(\frac{m}{s}\right)$
v_i	Species velocity, $\left(\frac{m}{s}\right)$
w_i	Mass fraction of species, *i*
x_i, x_j	Molar fraction of species, *i* or *j* respectively
A_c^*	Apparent pre-exponential factor, $\left(\frac{m^3}{kg.s}\right)$
A_L	Pre-exponential factor for LTCC sintering, $\left(\frac{1}{s}\right)$
Ar_L	Area of geometry of LTCC layers
Ar_c	Area of geometry of the carbon layer
C_i	Molar concentration of species *i*, $\left(\frac{mol}{m^3}\right)$
C_p^e	Effective heat capacity of porous medium, $\left(\frac{J}{mol\ K}\right)$
C_{pi}	Heat capacity of gas species, *i*, $\left(\frac{J}{mol\ K}\right)$
$C_{p\_i\_0}$	Molar specific heats of reactant or product, *i* at reference conditions, $\left(\frac{J}{mol\ K}\right)$
$C_{p\_i\_T}$	Molar specific heats of reactants or products, *i* at reacting conditions, $\left(\frac{J}{mol\ K}\right)$
C_{ps}	Heat capacity of solid matrix, i.e carbon or LTCC, $\left(\frac{J}{mol\ K}\right)$
D_i^e	Effective diffusivity for multicomponent diffusion, $\left(\frac{m^2}{s}\right)$
$D_{i,j}$	Ordinary molecular diffusion for specific species *i* and *j*, $\left(\frac{m^2}{s}\right)$
$D_{i,j}^e$	Effective ordinary molecular diffusion for specific species *i* and *j*, $\left(\frac{m^2}{s}\right)$
$D_{i\,k}^e$	Effective diffusivity of species due to Knudsen diffusion, $\left(\frac{m^2}{s}\right)$

$D_{i\,m}^{e}$	Effective diffusivity of species due to molecular diffusion, $\left(\frac{m^2}{s}\right)$
E_c	Activation energy for carbon burn-off reaction, $\left(\frac{J}{mol}\right)$
E_L	Activation energy for LTCC sintering, $\left(\frac{J}{mol}\right)$
ΔH_r	Heat of reaction for chemical reaction, (J)
ΔH_1	Change in enthalpy to cool reactants from T to T_0, (J)
ΔH_2	Heats of formation or change in enthalpy to form products at standard condition of 298 K and 1 atm, (J)
ΔH_3	Change in enthalpy to heat products from T_0 to T, (J)
$H_{f\_i\_0}$	Heat of formation of reactants or products, i at reference conditions, (J)
L	Instantaneous sample length during sintering, (m)
L_0	Initial sample length before sintering, (m)
L_f	Sample length at completion of the sintering, (m)
N	Number of gas species in gas mixture
M_g	Molecular weight of gas mixture, $\left(\frac{kg}{mol}\right)$
M_i, M_j	Molecular weight of gas species i or j respectively, $\left(\frac{kg}{mol}\right)$
p_g	Total gas pressure in the system, (Pa)
Q	Heat source, $\left(\frac{W}{m^3}\right)$
R	Universal gas constant, $\left(\frac{J}{mol\,K}\right)$
R_v	Reaction mass rate due to chemical reaction, $\left(\frac{kg}{m^3 s}\right)$
R_i	Mass rate of generation of species i due to chemical reaction, $\left(\frac{kg}{m^3 s}\right)$
R_T	Total mass rate of generation of all species, $\left(\frac{kg}{m^3 s}\right)$
T_{iso}	Isothermal temperature under TGA, K

Greek Letters

α_c	Degree of carbon burn-off or degree of conversion for carbon burn-off
α_L	Fractional shrinkage related to LTCC sintering
β	Constant heating rate, $\left(\frac{K}{s}\right)$
γ	Pore shape factor
$\varepsilon, \varepsilon_c$	Porosity of porous medium and carbon respectively
ε_{c0}	Initial porosity of carbon before burn-off
ϵ	Pore shape factor exponent
η	Product ratio of carbon burn-off, $\left(\frac{CO}{CO_2}\right)$
κ	Gas permeability of solid, (m^2)
μ, μ_i, μ_j	Dynamics viscosity of fluid medium, gas species *i* or *j* respectively $(Pa.s)$
ρ_{cb}	Bulk density of carbon, $\left(\frac{kg}{m^3}\right)$
ρ_{ct}	True density of carbon
ρ_i	Mass concentration of species *i*, $\left(\frac{kg}{m^3}\right)$
ρ_g	Density of mixture or total gas phase, $\left(\frac{kg}{m^3}\right)$
ρ_s	Density of the solid phase, $\left(\frac{kg}{m^3}\right)$
τ	Tortuosity of porous medium
ϑ_i, ϑ_j	Molar diffusion volume for species *i* or *j* respectively, $\left(\frac{m^3}{mol}\right)$

Subscripts

c, O_2, CO_2, CO	Carbon, Oxygen, Carbon dioxide, Carbon monoxide respectively
g	Gas phase

s	Solid phase
i, j	Number of species
L	LTCC

Chapter 1

INTRODUCTION

Multilayer ceramics technology has advanced progressively since the introduction of multi-layered monolithic ceramic capacitor in the late 1950s. In the 1980s, the major effort was focused on the manufacturing of multilayered ceramic circuit substrate for electronic components and modules for computers, but lately the focus had shifted to high speed wireless applications [1]. Due to the impending requirements of low loss dielectric materials, low resistance wiring and high interconnect density, the substrate material systems have also evolved from the traditional High Temperature Co-fired Ceramics (HTCC) technology to Low Temperature Co-fired Ceramics (LTCC) technology. LTCC uses liquid phase sintering technology [2] to allow low temperature glass phase to densify the ceramic body at a lower temperature of about 1173 K. This allows the use of low melting but low electrical resistance metals as conductors, for example, Cu, Au and Ag. Other advanced LTCC systems also use glass-ceramics as the sintering medium. By controlling the crystallization phases, the physical properties of the sintering parts could be tailored to suit the specific applications [3]. The advantages of LTCC over HTCC may be summarised as:

- Low dielectric loss at high frequency i.e. glass-ceramics [4] as a dielectric medium;
- Low loss metallization i.e. Ag, Au, Cu, Ag-Pd, Ag-Pt conductors;
- Matching coefficient of thermal expansion with the chip material i.e. Si;
- Excellent reliability for high density board interconnection;
- Ease of integration with other materials i.e. integrated passives.

Due to the LTCC characteristic properties in electrical, mechanical and chemical, and also the ease of 3D structuring by layers lamination, the applications of LTCC technology have extended beyond electronics to the areas of chemical analyses, inertial systems, fluid handling and control, and distributed sensor and actuator networks [5-9]. LTCC has recently received significant attention for potential applications in Meso-scale Microsystems with a minimum feature size in the range of 10 μm to several hundreds of μm. Intensive research to develop a new breed of "Ceramics MEMS" is on-going. Examples of some of the recent developments in LTCC based micro- or meso-systems are shown in Figure 1-1.

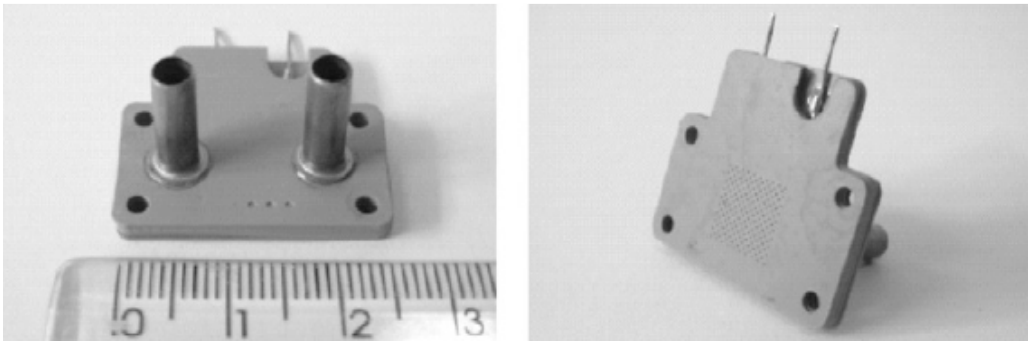

(a) LTCC based Microplasma Generator [10].

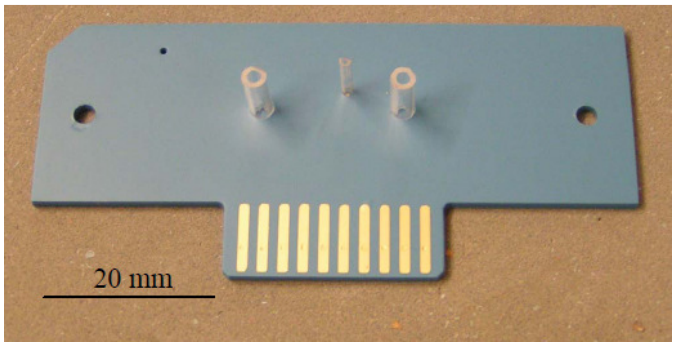

(b) LTCC based Electrochemical Cell [11].

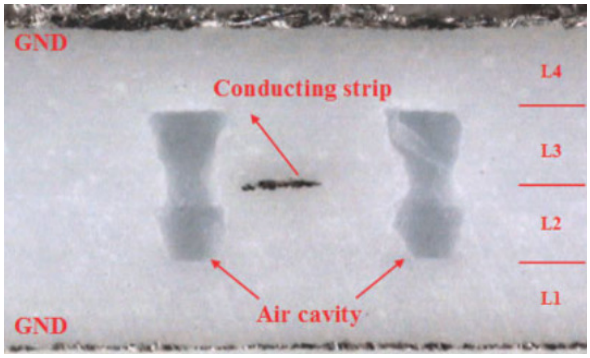

(c) LTCC based Stripline resonator with embedded air cavity [12].
Figure 1-1 Examples of LTCC based systems.

LTCC is designed as a multilayer technology which shares the common fabrication platform with HLCC but with entirely different material system sets. LTCC allows low temperature firing and provides much wider range of choice of materials to be incorporated into a ceramic substrate. Due to its low temperature processing and ease of structuring using layer additive processing, incorporating open and embedded structures becomes easier. Over the years, many structuring methods were developed and demonstrated. Approaches such as using shaped temporary inserts for simple open features to using fugitive and sacrificial layer for complex embedded structuring are available. A good structuring process should be able to retain dimensional accuracy throughout the fabrication processes which includes high pressure lamination and sintering process, but at the same time could be easily integrated into the existing fabrication processes of LTCC. Among the processes, use of a fugitive layer for structuring especially for fully embedded structure meets the above requirements. The fugitive material should be thermally decomposable with no or little residue left. The common fugitive materials are those thermally decomposable materials such as polymer or carbon based materials. Carbon was found to be suitable as its gasification temperature under an air environment is higher than the polymeric based fugitive materials to facilitate burn-off during LTCC sintering. Furthermore, carbon could be

easily purified by cycles of heat treatments to achieve low or no residue after complete burn-off.

1.1 Research Challenges

Various methods has been developed and demonstrated for the carbon fugitive process for embedded structuring; however, challenges and issues remain. The control of the reduced O_2 at mixed N_2/O_2 sintering environment, the effect of the heating rate for carbon burn-off, the competing kinetics between the carbon burn-off and sintering, the distortion of the structure due to pressure build up with gasification and the effects of gravitational structural body force, are some of the challenging issues. The process has not been fully established or characterised. Process characterisation is needed. It could be conducted experimentally or more rigorously by a physical phenomenon based process model. In this study, the formulation and the development of a process model for process characterisation and its practical use in a production environment will be explored.

1.2 Objective and Scope

The aim of this study is to understand the carbon fugitive material burn-off kinetics under embedded condition and to develop a theoretical/numerical model for optimising the embedded structure fabrication process using LTCC as a basic platform for microsystems and micro-wave applications. The followings will form parts of the scope of this study:

(i) Identifying carbon as fugitive material for embedded structure and its burn-off kinetics analysis using thermoanalytical tools.

(ii) LTCC sintering kinetics analysis using thermoanalytical tools.

(iii) Identifying major physical phenomena for embedded carbon burn-off under LTCC microsystem platform.

(iv) Development of a theoretical model for embedded carbon burn-off process under embedded condition by considering multicomponent mass transportation coupling with chemical reactions (carbon burn-off and LTCC sintering).

(v) Validation of the developed model experimentally by the scale-down samples under laboratory conditions.

(vi) Demonstration and optimisation of a fully embedded air cavity process for microsystem applications.

1.3 Novelty

A process model for fabrication of embedded structure in LTCC using fugitive carbon has been successfully developed. The complex process mechanisms of the interrelated kinetics of carbon burn-off and LTCC sintering have been successfully modelled by conventional mass diffusion and convection equations coupled with energy balance equations and kinetic rate equations of carbon burn-off and LTCC sintering. Simple experimental based methodologies which could be easily set up by using TGA and TMA for the determination of kinetic parameters of carbon burn-off and LTCC sintering have been established. This developed model could well be utilised for the optimisation of firing profile, with the potential to significantly reduce process setup time and to produce high quality large embedded structure in LTCC with less wastage in sample preparation. A usual trial and error approach in optimising sintering profile for LTCC embedded structure fabrication could then be eliminated.

1.4 Contributions

In this study, a specific physical phenomenological based process model, which has not been explored elsewhere, has been developed for embedded carbon burn-off in LTCC for embedded structure fabrication. Along with the model development, experimental kinetic analysis for carbon burn-off and LTCC sintering has been developed for quick kinetic parameters determination without the necessity to delve into the detailed kinetic processes.

Solid catalysed carbon burn-off has been established which hitherto has not been reported for fugitive carbon burn-off in LTCC. Both accelerated and retarded reaction rates, which depend on the type of LTCC tape used, have been observed.

By implementing the process model, multi-step firing profile has been demonstrated to reduce pressure build-up resulting in minimal swelling and sagging of the cavity. A near free distortion fully embedded cavity with average maximum cavity height variation of just 75 ± 41 μm over a span of 32 mm has been achieved. This is a notable achievement as it paves the way for the optimisation of processing conditions for carbon burn-off and LTCC sintering through simulation.

1.5 Outline of Dissertation

The thesis is organised as follows:

Chapter 1 introduces multi-layer ceramic technology and the evolution of LTCC technology and materials. Challenges and issues arose from the fabrication of embedded structure in LTCC lead to the objective and scope for the study. Chapter 2 presents a comprehensive review of the present embedded structure fabrication

technique of LTCC. Literature review is also conducted for exiting models leading to the development of embedded carbon burn off process model in LTCC involving both carbon burn-off and LTCC sintering. Chapter 3 describes the method of obtaining the kinetic rate parameters and the effect of carbon catalytic reaction introduced by the LTCC materials. Method of using thermoanalytical tools to obtain a simple sintering rate parameters required by the model is also introduced. Chapter 4 examines the physical phenomena of carbon burn-off in the embedded cavity of LTCC structure. This allows the development of an axisymmetric 2D model for carbon burn-off in embedded cavity based on multicomponent mass transport and chemical reactions of carbon-gas reactions coupled with LTCC sintering. The model is validated by rigorous TGA testing of scale-down samples under different sets of heating profiles. The modelled results based on averaged carbon burn-off curves are compared with the TGA measured results. Chapter 5 implements the process model for a large embedded air cavity suitable for microwave, microfluidic and MEMS applications. The sintering profile is optimised based on the internal total gas pressure to achieve a near distortion free cavity structure. Chapter 6 concludes the study and outlines future work for further investigation.

Chapter 2

LITERATURE REVIEW

Both LTCC and HTCC fabrication processes are multilayer technologies allowing individual layer processing before collating and co-fired to form a monolithic sintered structure. One of the major differences is the material system used. LTCC uses low temperature glass system as the major sintering medium which allows a sintering temperature of less than 1123 K, while HLCC uses majority of Alumina at about 1873 K. Understanding the LTCC multilayer fabrication processes and its material system with its sintering characteristics are essential to allow process advancement for structure formation in LTCC for both open and embedded structure.

2.1 LTCC Fabrication Technology

The LTCC multilayer substrate fabrication processes are shown in Figure 2-1, which include the following essential processes:

(i) Green sheet preparation: This involves the preparation of a slurry which is a mixture of powders (glass, ceramics, glass-ceramics) and binder. The formulation of a powder system is essentially proprietary and tailored to the specific applications. The green sheet is produced by tape casting [13]. LTCC green sheet is readily available commercially and the list of the major suppliers could be found in reference [1]. It comes with different blank sizes (100 mm – 300 mm) with various thicknesses (50 μm to 250 μm).

(ii) Via and structure forming: This involves the formation of via to provide interconnecting paths with the layers. Via is formed on each individual green sheet typically by a high speed mechanical punching system with a minimum via size of

about 50 μm. However, laser and chemical etching (solvent jetting) [7] systems had been developed for achieving a finer via size smaller than 25 μm. For cavities or special structures forming such as embedded channels for a fluidic system, it is not unusual for them to be created together with the vias using the same forming process. Structure could also be formed by overlap punching [14], CNC milling, laser machining and chemical etching process.

(iii) Via filling and pattern printing: These involve via filling with a conductive ink as well as the printing of circuitry and sometimes integrated components such as resistor paste. Generally, it is achieved by using the technique employing a hybrid screen printer with a doctor blade. The blade is usually a polymer squeegee shaped at a specific angle to the screen for an efficient transfer of ink. Via filling is achieved by printing ink over the carrier side of the green sheet with or without a stencil. Patterning (circuitry) on the green sheet is achieved by screen printing through the silk mask. Multiple printing is sometimes required to improve the ink deposition quality or integrated with other functionality inks. Ink has to be dried between each print at about 343 K for 10 min to 15 min. The typical line/space resolution is 75 μm/75 μm. For finer printing resolution, special ink formulation and finer screen mask have to be sought. Alternatively, photoimageable ink system such as Dupont Fodel® conductor system could be used in conjunction with the lithographic process for finer patterning.

(iv) Collating and laminating: This involves the registration of individual layers of green sheet after via/structure forming. The layers are collated, pre-tacked and laminated under pressure and temperature conditions. Lamination is achieved by either a hydro-isostatic or uniaxial laminator. Typical lamination conditions are in the pressure and temperature ranges of 100 kg/cm^2 – 250 kg/cm^2 and 333 K – 353 K respectively. At these conditions, the polymer binder in the green sheet fuses and

allows interpenetrating of powder across the layers' interfaces. Having uniform laminating pressure over the layers is a key requirement for a defect free product.

(v) Debinding and sintering: A pre-cut (for ease of de-panelisation) or trimming of LTCC laminate to shape is usually required before the debinding and sintering processes. Thermal debinding is normally employed to completely drive off the solvent and binder before the sintering process. It is achieved by heating the sample gradually (1 K/min to 2 K/min) to the binder decomposition temperature (673 K to 873 K). The sample might have to be soaked at the decomposition temperature for a sufficient length of time (several hours) if the sample is thick and large. This is followed by a faster heating rate (5 K/min to 10 K/min) to the sintering temperature (1073 K to 1223 K). The specific heating profile is very much dependent on the size of the samples, material systems and structure complexity.

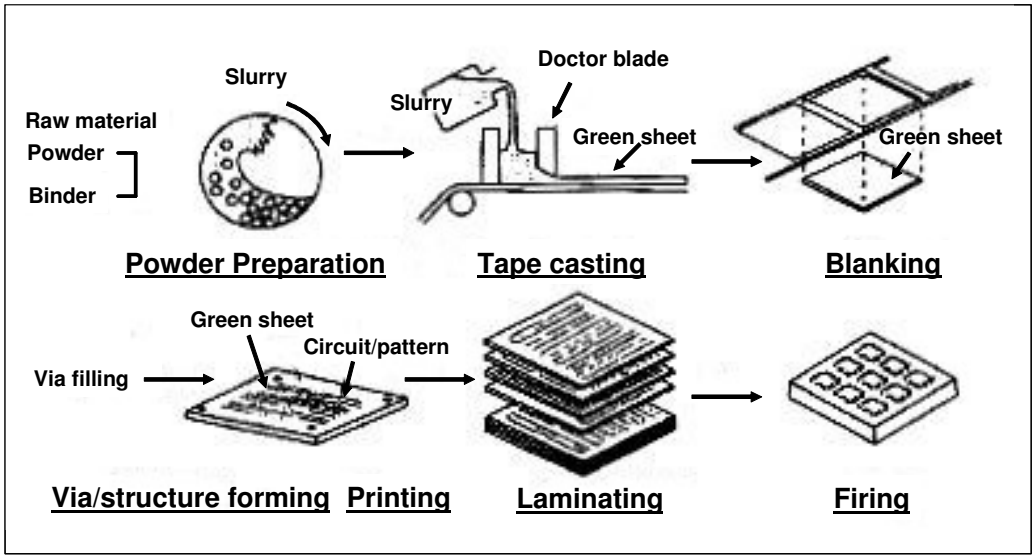

Figure 2-1 Typical LTCC process flow including structuring step [1].

2.2 LTCC Material Systems

LTCC, as its name implied, is a ceramics material system, designed to co-fire or co-sinter with the metal wire (for circuitry) at a lower temperature than the HTCC. This allows the use of high electrical conductive metals with melting points below 1273 K, such as Ag, Au, Ag-Pd and Ag-Pt. High conductive metals are necessary to provide the required electrical properties for high speed wireless application in which HTCC's metal systems are unable to accommodate. HTCC uses metals such as Mo, W, Mo-Mn which have very poor electrical conductivity but high melting point for co-firing at 1873 K.

To achieve densification of LTCC at this low temperature, it is common to use a glass system of amorphous glass or crystallised glass. They act as a binder for the glass ceramic composite and improve the sintered density at a reduced time by liquid phase sintering. Most recently, advanced crystallisable glass-ceramic systems had been developed and used commercially. Figure 2-2 shows the LTCC material systems used in practice. However, the common commercial systems are based mostly on ceramic-glass composite (CGC) and glass-ceramics (GC) which can provide low dielectric loss, high mechanical strength and matching thermal expansion coefficient for microelectronic packaging of high performance electronic modules. The typical commercial systems such as Dupont and Heraeus LTCC are based on GCC while Ferro LTCC is based on GC.

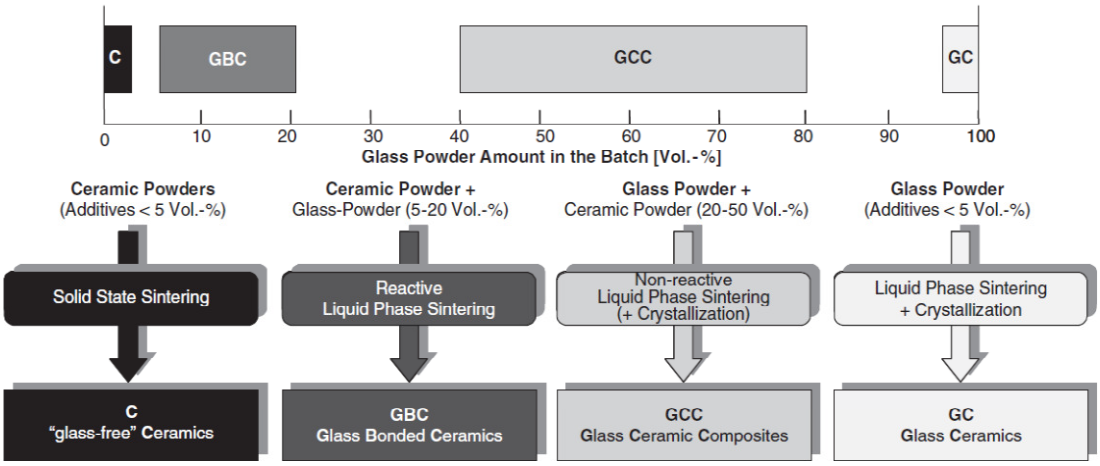

Figure 2-2 Common LTCC material systems used in applications with associated sintering mechanisms relative to glass content [15].

2.3 Sintering Shrinkage of LTCC

LTCC has a typical shrinkage of 8 % – 20 % in the X and Y directions and about 15 % in the Z direction after sintering. The shrinkage tolerance is ±0.15 % [16]. Post sintering processes, such as mechanical grinding/lapping and electro-plating processes, are sometimes required to improve the flatness of the multilayer substrate and also to enhance surface metallization for better wire bondability or solderability for subsequent assembly processes. Dimensional control and stability are difficult without many trial runs. The inherent sintering shrinkage has to be factored into the design for the various fabrication processes.

Constrained sintering processes had been developed to produce dimensionally accurate multilayer substrates. Many constrained processes were available. Mikeska et al [17] had incorporated external (bottom and top) sacrificial release layers to constrain the internal LTCC laminate by interfacial frictional forces between the sacrificial and LTCC layers during sintering. As the layers of the LTCC laminate nearer to the sacrificial layers are more constrained than the inner layers, the edges become concave

after constrained sintering. Thus, the maximum number of LTCC laminate was limited to about 25 layers (for 0.113 mm thick green tape) to have an acceptable dimensional tolerance [16]. Furthermore, the external release layers had to be removed by a mild removal process such as sand blasting, and post external metallization was required. In order to improve the process, self constrained laminate was developed to include permanently the "sacrificial layers" as part of the fired structure. However, it involved the proper arrangement of constraint layers within the LTCC laminate and might affect the overall physical properties of the LTCC structures [16].

In contrast, Lautzenhiser et al [18] developed a self constrained LTCC tape system by incorporating directly the constrained layer into the green tape via a novel tape casting method. Each individual self-constrained tape was a 3-layers structure consisting of a closely packed, near zero shrinkage (at LTCC sintering temperature) refractory constrained layer sandwiched by two LTCC layers. In contrast to the former constrained mechanism by a high interfacial friction force between the sacrificial and LTCC layers, the constrained effect of the self-constraint tape was by densifying the LTCC layers over the densely packed refractory porous layer. The glass phase from the LTCC layers softened and drew into the constrained layer by capillary force promoted by the wetting agent and the pore structure of the constrained layer. With this arrangement, the shrinkage in the X and Y directions was controlled in the range of 0.07 % - 0.10 %, with a tolerance of ±0.023 % [19]. Significant sintering shrinkage (25 % - 40 %) was restricted in the Z direction [16,19].

For exploring free structuring in LTCC for microsystem applications where dimensional control is important, a tape system which provides low or near zero

shrinkage in the X and Y directions is favoured. Low sintering shrinkage will likely to produce less cambering sample due to non-uniform shrinkage rates caused by the complex structuring. Thus, for this current investigation of embedded structure fabrication, commercial low shrinkage self-constrained tape system developed by Herarus Inc (HL2000) [19] was employed. HL2000 is a self-constrained tape system [18] where the removal of the release layers is not necessary. There is virtually no limitation in the number of tape layers that can be employed for the LTCC laminate.

2.4 Co-Sintering of LTCC

The major components of LTCC system, as indicated in Section 2.2, often consist of a ceramic filler such as Alumina in a glass matrix. The common defects such as cracking, delamination, voiding and distortion seen in most of the co-sintering of other systems are also existent in LTCC [147-151]. Inhomogeneity of ceramic filler size [151] from the tape casting process and subsequent layer lamination of heterogeneous powder compacts [150] could induce non-uniformity in sintering stresses within layers. Co-sintering of layers of powder compact having differences in green density and ceramic systems could result in band of void formation at the layer interface resulted from the viscous flow of glass composite and the effect of wetting of ceramic fillers. Mismatch in shrinkage and thermal expansion during heating and cooling of sintering cycle also induces layer delamination and distortion [149]. Co-sintering involving reactive sintering of glass with ceramic fillers accelerates the sintering cycle but complicates the process of producing defect free parts. Various models for co-sintering particularly for two powder systems were developed. Suri et al [153] presented the criteria for defect free co-sintering based on elastic-plastic empirical model of porous sintering metals by determining the induced stress resulted from difference in shrinkage

during sintering. The in-situ strength of the weaker material during sintering was taken into consideration in the model. Chang et al [152] had developed an in-situ camber measurement together with a viscous model to predict stress developed in the bi-layer glass-based LTCC systems. The predicted biaxial stresses could thus be used to predict defect free co-sintering.

LTCC is designed to co-sinter with conductive metal inks for electrical interconnection. The mating of shrinkage and thermal expansion between the LTCC and conductive metal system is critical. The in-situ camber methodology developed by Chang et al [152] could be applied in the development of co-fired silver based metallization for LTCC [154]. New LTCC systems will continuously face challenges in co-sintering issues with new glass system with acceptable low dielectric requirement for high speed RF applications.

2.5 Embedded Structure Fabrication

To realise 3D structure in LTCC for ceramic microsystems, forming of embedded structures is inevitable. Structures could be formed by various methods such as mechanical milling/punching/stamping, laser abrasion/cutting and chemical solvent etching/jetting. They could first form open structures on each individual green sheet or green sheet laminate. The structured green sheets are then laminated and co-fired to become a monolithic embedded structure. For RF millimetre wave application, it is essential to preserve and control the dimensional accuracy of the embedded structure such as a simple air via or cavity [19,20]. A drift of dimensional tolerances will critically affect the enclosed air volume and thus the overall effective dielectric constant gained from the embedded structure for the system. The unfilled suspended

structure (without lamination) of larger than ∅4 mm was reported to have severe sagging due to sintering induced deformation [9]. The embedded structure must be able to retain its dimensional accuracy from lamination and the subsequent sintering process. Many techniques particularly in the area of lamination processes were developed over the years and could be summarised as follows:

(i) Use of glue layer: Use of a glue layer, such as commercial polyacrylate based double coated pressure-sensitive adhesive film, between layers and structures to allow low (2.5 MPa – 5 MPa) or even zero pressure lamination [5,21-23]. This avoids the collapse or severe deformation of the structure during lamination. The glue layer is recommended to have a slightly higher melting point than the debinding temperature of the LTCC. The capillary force caused by the flow of the adhesive melt between the LTCC porous skeleton structures after debinding pulls the interfaces together to allow layers interpenetration during the sintering process. The lamination mechanism is as shown in Figure 2-3. This method was successfully used for the fabrication of vaporizing liquid microthruster for microspacecraft applications. However, it requires matching LTCC systems and no metallised interconnections are possible between layers [24].

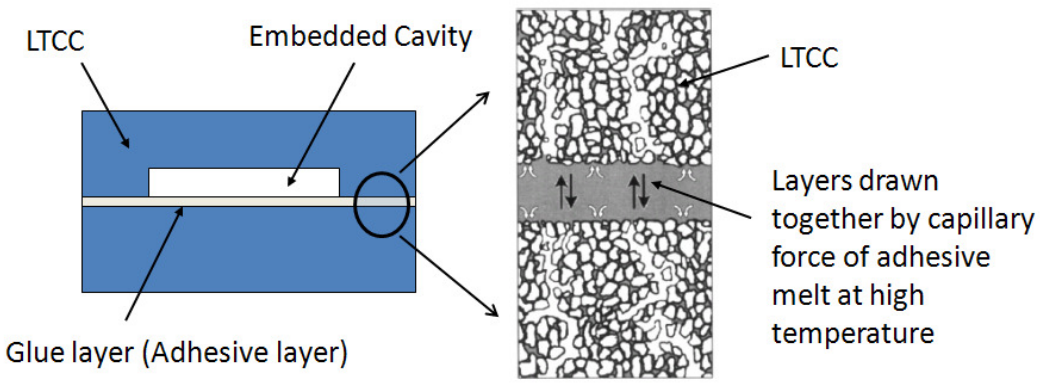

Figure 2-3 Use of adhesive layer as glue layer for low pressure lamination and its lamination mechanism [21].

Low temperature transfer tape (LTTT) could also be used as high temperature glue layer to permanently bond fired LTCC structures [25,10]. The fabrication steps closely resemble the conventional thick film processing, and bonding is achieved by post processing. The post-fire process steps for the fabrication of a microplasma generator are shown in Figure 2-4.

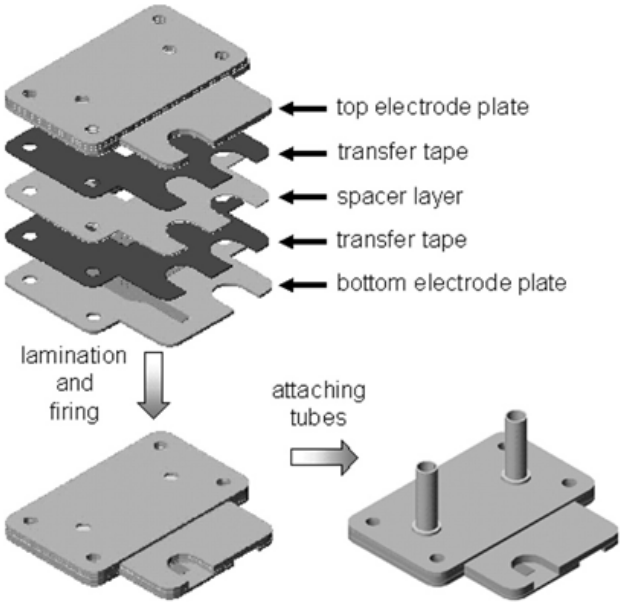

Figure 2-4 Use of LTTT as post-fire glue layer for the fabrication of embedded structure for microplasma generator [10].

(ii) Use of multi-step lamination: Another way of preventing severe deformation of structures during lamination is to pre-laminate the individual structure stack first at a lower lamination pressure before combining all stacks using the higher final lamination pressure to form the monolithic structure [26,27]. The thick layer over the structure will resist better the deformation and thus resulting in less deformation. The additional lamination steps are included in Figure 2-5.

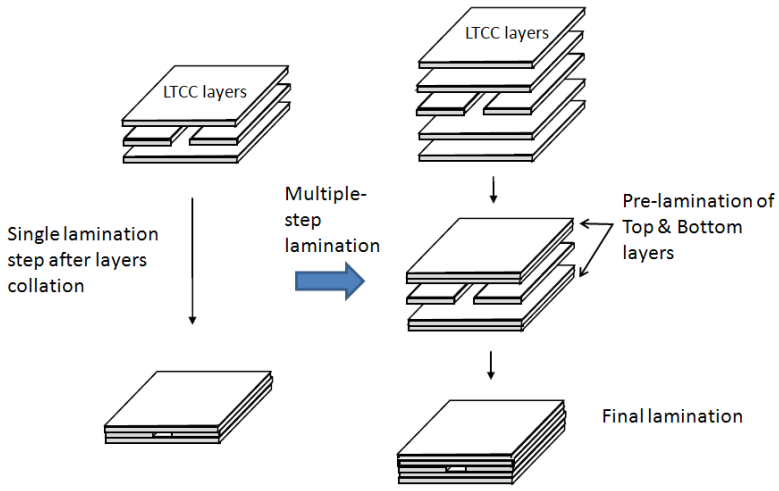

Figure 2-5 Improved inner layer cavity forming by multi-step lamination [27].

(iii) Use of stress compensating materials: Thick film materials, such as resistor or metal paste, have a higher coefficient of thermal expansion (CTE) than the LTCC tape. Using these thick film materials on the suspended structure will exert a compensating stress against the gravity induced sagging plastic deformation as shown in Figure 2-6. The material has to be properly selected to match the LTCC system so as to hold the structure together during sintering [28]. It is likely to be used in compliment with other techniques as the stress compensating material is not able to withstand the lamination pressure.

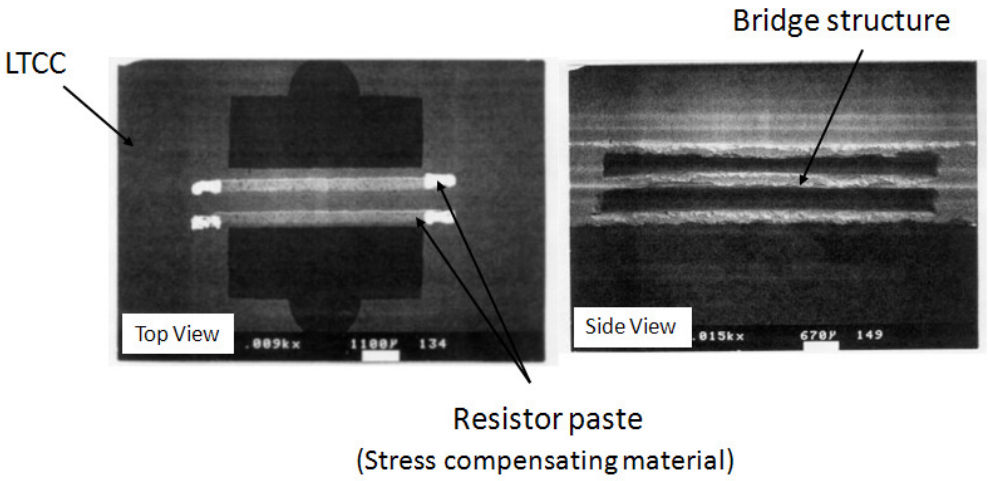

Figure 2-6 Use of screen printing resistor paste as a stress compensating materials for a bridge structure design embedded in LTCC [28].

(vi) Use of temporary insert: Shaped inserts made of wax or polymer as in Figure 2-7 have been used with or without cavity definitions to support the structure during lamination [26,29]. They are normally removed after lamination but could be burnt off during the sintering process. In some instances, cleaning of structure (micro-channels) may be required after sintering especially for fluidic applications [11,14]. Removal of insert after lamination may pose difficulty. However, for some low melting point inserts, it will be prudent to melt it and drain it out from the enclosure. It could not be used for a fully enclosed structure without access paths such as inlet and outlet ports.

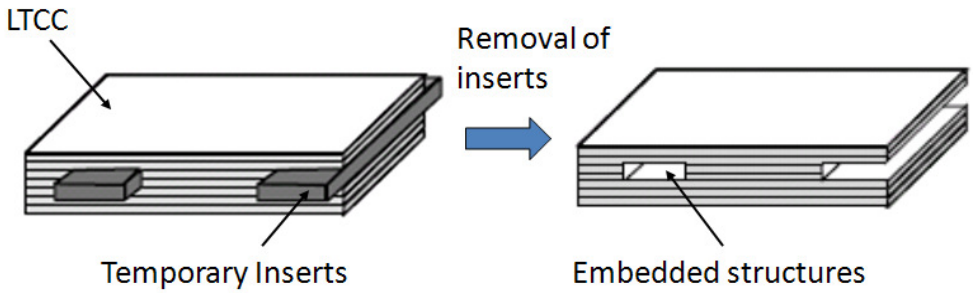

Figure 2-7 Use of temporary inserts for embedded structures [27].

(v) Use of sacrificial or fugitive materials: Use of glass, polymer and carbon based materials as the sacrificial or fugitive mediums that could be removed after sintering or during sintering is the most promising technique to retain the shape of the structure during lamination and possibly even during sintering. The fugitive materials which are in liquid, paste, tape and even shaped solid forms are normally filled in after the definition of the structure [30-33]. Glass based medium such as Pb bi-silicate, will remain after sintering. An intensive chemical process which involves the handling of hydrofluoric acid (HF) can be used to selectively remove the sacrificial medium [7,28]. In contrast, polymer and carbon based mediums provide support for the structure during lamination and can be decomposed or burn-off during sintering without the need of post

processing. By controlling the burn-off kinetics of carbon fugitive materials for a small cavity, it was reported that carbon can support the suspended structure throughout the sintering cycle without swelling or sagging for a Ø10 mm thin membrane [34]. Carbon burn-off rate could be retarded under a partial inert environment of air/nitrogen mixture. By adjusting the mixing ratio of air/nitrogen environment during sintering, the carbon fugitive material could decompose during densification while supporting the structure against sagging due to gravitational effect [9]. The effect on cavity forming using a controlled firing environment of O_2/N_2 is shown in Figure 2-8.

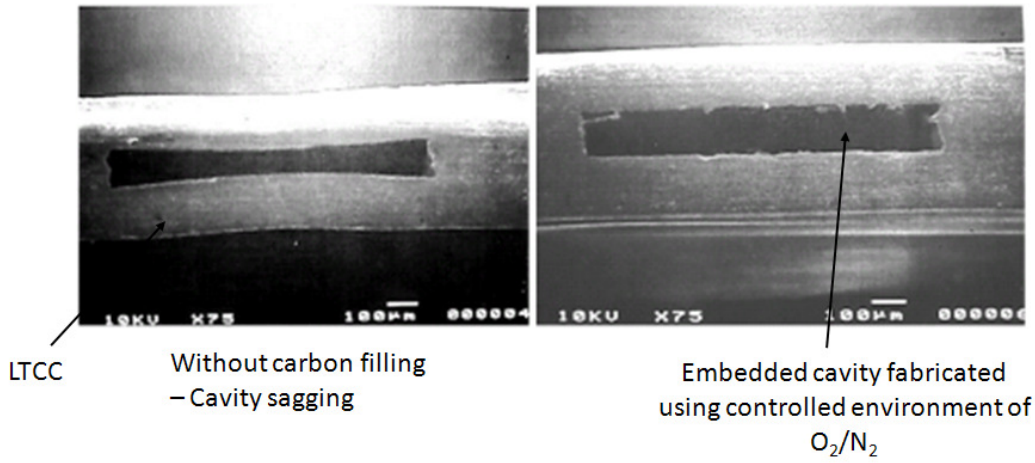

Figure 2-8 Use of carbon filling as fugitive structure supporting material firing under reduced ratio of O_2/N_2 [7].

As a summary, Table 2-1 compares the current techniques employed in the manufacturing of 3D LTCC structures.

Table 2-1 Comparison of current techniques in realising three-dimensional structures.

Technique	Advantages	Disadvantages
Lamination with insert	• Better dimensional control for surface structures • Support structures during lamination	• Limited to relatively large and simple structures • Tailored and removable inserts required • Difficulty in insert removal as sticking of green laminate to insert may occur • No support during sintering
Low pressure lamination (use of glue layer & multiple lamination steps)	• Complex 3D structures (with dimensions of 100 µm to 10 mm)	• Precise alignment between tapes or laminates is difficult • Delamination could occur between laminates • Required compatible adhesive and ceramic systems • Additional lamination steps required • Interconnection between sintered substrates is not feasible with adhesive layer • No support during sintering
Lamination with fugitive or sacrificial material	• Complex 3D structures and suspended thick film (with dimensions of 100 µm to 10 mm) • Could achieve full enclosed and embedded structures • Could provide support during lamination and sintering	• Relatively poor dimensional stability • Filling and patterning of fugitive or sacrificial materials are difficult • Post processing i.e. chemical etching may require
Gluing method (Post-firing)	• Relatively good dimensional control • Relatively large embedded structures (more than 10 mm)	• Precise alignment between sintered substrates is difficult • Interconnection between sintered substrates is not feasible • Post processing required for joining the sintered laminates. Could be tricky as the sintered laminates are fragile • Extra layers of “glue” required, needs properties matching
Co-firing of thick film	• Support structures during sintering	• No support during lamination • Location and volume of metallic loading are difficult to estimate

Though the fabrication of a 3D structure on LTCC, particularly on the structuring and lamination processes of LTCC green tape, was covered extensively in the literature, manufacturing of embedded structure is still in its infancy. The initial industry

adoption is still waiting for market demands. Typical industrial standards in term of physical properties and geometrical tolerances for mass ceramic based micro-system are not available. The requirements for material and process specifications are very much dependent on specific area of applications. In high speed RF applications, the dielectric constant required may be less than 6.0; this is achieved by careful selection of material systems. For microfluidic systems, the material system has to be leak-proof and resistance to chemical. This will require fully dense parts. The embedded channel will need to have dimensions of handling micro-litre fluid. Thus a LTCC system with small sintering shrinkage (typical value of 0.2 %) may be required. LTCC based microsystem is unique and applicable for meso-scale system that a traditional Si platform may not be economically viable. Some exploratory works on realizing microfluidic based systems and BioMEMS could possibly provide some insights on the process requirements.

- Design of embedded hydrogen peroxide catalyst combustion chamber for mini-satellite which is in the range of 10 – 50 kg will require 0.325 N thrust load. The combustion was obtained from reaction of continuous flow of reactant at 0.00025 kg/s within a 8 embedded channel chambers of 0.75 mm x 0.254 mm [157].

- Ceramic based BioMEMS which required continuous flow PCR with zone temperatures accuracy of +/- 1 °C were achieved by including embedded chain of channels of 0.5 mm x 0.5 mm and air cavity of 2 mm x 11 mm for thermal control. [158].

- Micro heat pipe was realized in LTCC with embedded porous wick structure of width 0.5 mm and thickness 0.05 – 0.1 mm with high capillary force and large liquid volume. The structure was demonstrated for power density devices of 160 W/cm^2 [159].

Embedded structuring process in ceramic composites particularly in LTCC is challenging and the process involved is complicated. The processing mechanisms are specific to each technique and material system, and could well be entirely different from each technique or material system.

Low lamination approach using novel PSA double coated adhesive makes use of intrinsic capillary force of the adhesive melt to result in inter-penetrating of adjacent ceramic layers for sintering. LTTT which is a high temperature glass/ceramic composite layer could act as a glue layer for post sintering parts. The main mechanism involved is co-sintering of the post fired parts and matching shrinkage stress resulted from the thermal expansion. Others utilized green powder strength to prevent sagging resulted from the high lamination pressure. Compensating layer makes use of differential shrinking stress from co-sintering to support the structure during the cooling stages. The most intricate mechanism involved is associated with a sacrificial layer with high temperature burn-off such as a carbon sacrificial layer. It involves competing kinetics between the carbon burn-off and LTCC sintering. The control of the process parameters could significantly affect the quality and success of the process. The process mechanism is complex, but as indicated in Table 2-1, it is the most promising method that could be used to retain the dimensional geometry tolerance among the technique reviewed.

By employing sacrificial material that is able to support the structure during both lamination and sintering. Carbon as the fugitive material is of particular interest as its burn-off mechanism is relatively simple as compared to the polymer based materials. Burn-off is likely to be present during the course of sintering or at least in the initial

stage of sintering. In contrast, polymeric based materials will be completely decomposed during the debinding phase of the sintering cycle without providing the necessary support during sintering. Carbon based material gasifies directly from a solid phase to a gas phase under an oxidizing environment and the reaction accelerates at high temperature. It is chemically simple and left no trace of residue if purified carbon is used and if the burn-off is complete. Furthermore, carbon powder is readily available and is supplied in various forms, such as in paste and tape system. Carbon powder which is specially tailored for use as a sacrificial medium is also available, and it is supposed to have better burn-off characteristic.

Open and embedded structures for potential microsystem applications had been successfully fabricated [5,7,8,11,14]. The respective fabrication techniques related to structuring, lamination and sintering were also well developed and implemented. However, detailed process characterisation with respect to carbon burn-off and LTCC sintering, particularly under a fully embedded condition, has not been established. The possible catalytic reaction of carbon burn-off with LTCC and its effect on burn-off kinetic on LTCC sintering is also not reported for such an embedded condition. The competing kinetics between carbon burn-off and LTCC densification has to be considered for the optimization of the LTCC sintering process to result in a successful complete burn-off with no residue. Thus, it is necessary to develop a process model for embedded carbon burn-off in LTCC based on physical phenomena. This model would allow the examination of the burn-off process and its implication in process optimisation. It will provide an added avenue for the advancement of the embedded structure manufacturing technology in LTCC.

2.6 Process Modelling

Process model is always unique to a specific process and has to be developed specifically. An effective and efficient approach for the development of a new process model is to adopt and to adapt well established and related formulations for specific steps or phenomena of the overall process, and to adapt and integrate these formulations into a model which could describe the overall process. As mentioned in Section 2.5, the most promising process for an embedded structure in LTCC is using carbon as a fugitive layer for structuring. In addition, the impact to the existing fabrication process of LTCC is very minimal, namely the requirement of having additional fugitive carbon structure layers. The process flow for the embedded structure in LTCC could be realised as shown in Figure 2-9.

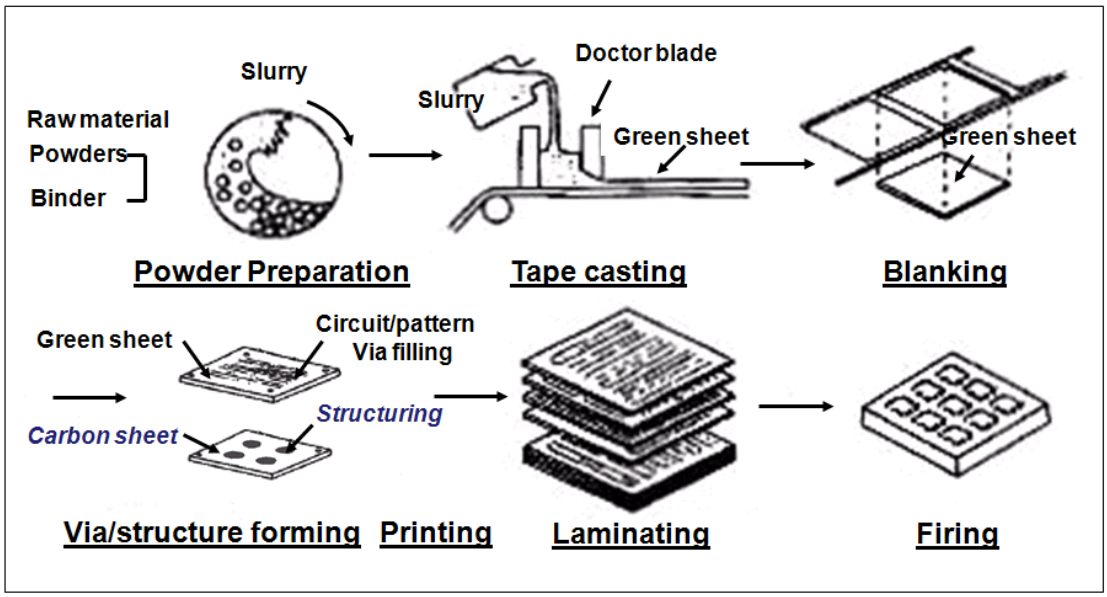

Figure 2-9 LTCC process flow including embedded fugitive carbon structuring step. Modified from Figure 2-1 [1].

The tape casting process of LTCC in the current study is specific for the HL2000 tape system. It is a self-constrained system which could provide better geometric tolerance than other systems. It uses proprietary wet on wet 3-layer casting technique. Some

insights of this process could be found in their patent [18]. The doctor blade tape casting employed and the final drying will affect the homogeneity of the final powder distribution. The inclusion of refractory layer as the constrained layer will also have a significant effect in the sintering stress uniformity over the laminates.

Structuring is done by using CO_2 laser ablation. Computer numerical controlled CO_2 laser allows omni-directional cutting for any required shape. It is a fast and contactless cutting process which uses high localized heating to decompose the polymer binder matrix. Hydro-isostatic hot lamination is used to compact the collated layers under high pressure at temperature near the T_g of the polymer binder so as to allow interpenetrating of the powder particles over the interfaces. It is similar to the conventional powder compaction process. The packing of laminate will affect the green density of the sample and may result in non-uniform sintering stress.

For embedded structure process using fugitive carbon process, the carbon fugitive layer will co-laminate with the LTCC layer to form parts of the monolithic structure. The selection of the polymer matrix for the carbon layer has to be matched or the same binder system with the LTCC system is to be used so as to aid the debinding process.

Debinding process involves drying and also decomposition of polymer matrix. It has received extensive research for an understanding of the physics of debinding for defect free sintering. The ultimate goal of a debinding process is to completely drive off the polymer binder but retain the geometrical shape before and after sintering. Improper control of a debinding process and incomplete debinding may result in severe voiding or even cracking during or after sintering.

The final process is the co-sintering of LTCC together with the fugitive carbon layer. It would encounter simultaneous carbon burn-off and LTCC sintering at some stage of sintering. The kinetics could be competing with the pore closure of LTCC blocking gas diffusion path for carbon burn-off.

It will not be possible to model all the process steps involved in the LTCC embedded structuring fabrication, and some of the less critical or significant steps or processes could be ignored without much loss of accuracy. Indeed, the most significant process is the focus of this study, namely the modelling of the sintering process where embedded fugitive carbon has to be burn-off during the sintering process. Competing kinetics between carbon burn-off and LTCC sintering are expected, which will seriously affect the success of the forming of an embedded structure. The various relevant models in the process are identified in Figure 2-10 and will be reviewed in the following sections.

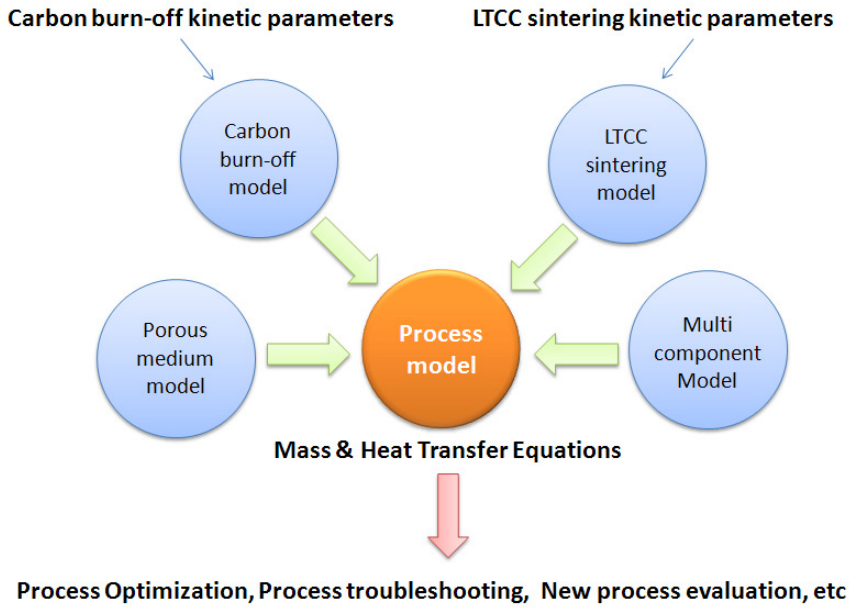

Figure 2-10 Integration of multiple process models for the LTCC embedded structure fabrication process using fugitive carbon.

2.6.1 Carbon Burn-off Model

Carbon burn-off, either under an embedded or open environment, is essentially a solid-gas reaction. As such, equations for solid-gas reaction are generally applicable. However, specific models or formulations closely related to carbon burn-off will have to be considered, and their appropriateness and applicability to LTCC embedded carbon have to be carefully evaluated. Most of the literatures are focused on a single particle or grain reaction. In principle, generalization of a single particle reaction to a particulate bulk of porous solid may be made [35]. Single particle reaction model could generally be classified into non-porous and porous solid reaction.

(i) Non-porous solid reaction

A solid is considered non-porous when it is impervious to gas diffusion. The solid-gas reaction could be assumed to occur at the surface of the solid. The common model based on geometry aspect is the shrinking core model developed by Yagi and Kuni [36]. They developed the specific basic characteristic and mass equations by including both the mass transfer resistance effect for the boundary film layer and the ash layer of a single carbon particle during combustion. Wen [37] has further generalised the equations so that the model could be applied for a wider situation where both heterogeneous and homogenous reactions with phase change of reactants could be represented. Wen has also introduced the effectiveness factor for solid-gas reaction to better examine the mass diffusion effect. The effectiveness factor employed for a solid-gas reaction for the maximum obtainable reaction rate is based on the concentration and temperature in the bulk fluid phase; while the common effectiveness factor for a catalytic reaction is based on the surface concentration and temperature at the surface of the catalyst [38].

For a compact pellet of non-porous grains, grain model or particle-pellet model developed by Szekely and Evans [39,40] was employed for the reduction of nickel oxides compact by hydrogen. Reaction starts at the surface of each grain according to the shrinking unreacted core model with a sharp interface between the product layer and the unreacted core. The governing diffusion equation requires the reaction rate expression to be established based on both the radius of the reacting grain and the global dimension of an idealised grain stacking structure. This presents some limitations in using the model practically where an idealised structure is not suitable. Thus, over the years, many modified grain models were developed but all are extensions of the structural models to cater for structure changes such as grain with various sizes and with changing surface area during reaction [35,41-43].

(ii) Porous solid reaction

A solid is considered porous if it consists of adequate voidage for fluid to flow freely within the body. If the solid reactant is uniformly distributed, then the reaction between the solid and fluid phases could be considered homogeneous. Thus, the reactions could be represented by a homogeneous volume reaction model [37] even though the reaction in nature is heterogeneous.

To describe the pore structure in the porous solid, Petersen [44] developed a pore model by assuming the pore structure as long cylindrical rods with random intersections. The reaction is assumed to take place at the pore wall with a continuous enlarging pore size. For model formulation, an idealized network of uniform cylindrical pore structure has to be assumed. The relationship between the reacting surface area and the radius of the pore has to be known. The limitations are that the pore structure assumed may not have

a good resemblance of the physical structure, and that there is no product layer formed during reaction. Pore coalescence observed in most of the porous solid reaction systems is also not included.

Bhatia and Perlmutter [45,46], utilised Avrami's theory [47] of growth in crystal aggregates, derived a random overlapping reacting surface as the basis for their random pore model. The initial structural parameters of pore volume, surface area and pore length were identified to be adequate for the characterisation of any porous sample of arbitrary pore size distribution. The formulation for the reacting surface was only based on the initial structural parameters for the reaction to be implemented in the grain model. The structure parameters could be physically measured using available techniques such as mercury porosimeter for pore size distribution and gas adsorption for surface area. The idealized pore structure of a uniform cylindrical pore with shape factor in Peterson's model is thus avoided in the random pore model. However, the measurements required are sometime quite challenging especially for carbon measurement with N_2 gas adsorption. One has to be aware also of the difficulties caused by activated diffusion [48,49].

Percolation and fragmentation model considers the collapse of a porous structure at a certain local critical porosity [50,51]. At higher reaction rate of char gasification with a diffusion gradient, peripheral fragmentation could occur at very early conversion resulting in a faster conversion rate due to the smaller particle size from fragmentation. This was reported experimentally and by simulation [52,53]. The critical porosity or percolation threshold was determined by indirect electrical resistivity measurements and further confirmed by physical observations [53]. It is important as it relates to the

commencement of the fragmentation and affects the overall conversion. However, its determination is not easy and direct.

In contrast to the generally well developed common nonporous gas-solid system in heterogeneous catalytic reaction, porous solid system involved complex inter- and intra-particle diffusions which are dependent on the particle stacking and pore structure. For a porous body consisting of an agglomeration of nonporous fine particles, non-porous solid-gas system could still be applied with inter-particle diffusion resistance as the major external mass transfer resistance.

Specifically for the carbon tape employed in this study, the carbon particles within the tape are uniformly distributed due to the nature of the tape casting method. The reacting interface of the carbon porous tape could be distinct or sharp if the reaction rate is high. It is approaching the nonporous solid reaction mechanism even if the sample is porous. In contrast, when the reaction rate is relatively low, the whole sample will be subjected to near constant gas reactant concentration, and the reaction will occur throughout the sample. Under this circumstance, the carbon burn-off process could be appropriately modelled as a homogenous volume reaction [56]. The overall size of the carbon layer could be changing or remaining constant dependent on the reaction zones [54, 55].

(iii) Catalytic carbon reaction

The burn-off of carbon or carbonaceous materials under an oxidization environment could be catalysed by many metals or its associates such as oxides and carbonates [57]. Any metal oxides that could be potentially reduced by carbon to its metallic state are a likely catalyst for carbon gasification [58]. The rate of reactivity by an alkali metal

carbonate such as Cs_2CO_3 has been reported to increase the reaction rate by a factor of thousand times. For metal oxides, PbO is the most active catalyst [59].

Instead of accelerating the reaction rate, some metallic oxides can retard carbon burn off. Some forms of aluminium phosphate has been reported to be a good inhibitor of graphite oxidation by a phenomenon known as active site poisoning or phosphorus scavenging [60]. This is in fact one of the techniques used to protect graphite from oxidation in a high temperature, oxidising environment.

The contact interface of the catalyst for carbon burn off has a significant contribution to the rate of reactivity. For embedded carbon in LTCC which is a compact composite of different metallic oxides, the effect of catalytic reaction, although has never been reported or investigated, could not be assumed to be insignificant. Extensive mathematical analysis for such a solid-catalysed gas-solid reaction was not available [61]. However, a simple single pore model with consistent close contact between the catalyst and the carbon interface was analysed by Lee [62] using the effectiveness factor of Thiele modulus. Guzman and Wolf [63] had also ascertained the need for uniform solid catalyst distribution for effective reaction conversion. In general, a more complete and rigorous modelling along with systematic experiments are required for carbon burn off in LTCC. Instead of formulating a new model of specific solid-catalysed gas-solid reaction for LTCC, an efficient and effective approach is to establish a model based on the gas-solid reaction with rate parameters determined experimentally for LTCC catalytic effect for carbon burn off.

(iv) Carbon reaction rate

Reaction rate measurements for gas-solid reactions were usually conducted with various techniques such as fixed/fluidized packed bed, entrained flow methods and thermogravimetry analyser (TGA) [64-67]. Packed bed is suitable for a wide range of particle sizes and is operated in either differential or integral mode for elementary kinetic mechanism analysis. With plug flow or stirred reactor setup, the error could be greatly reduced. To assure the kinetic data, the residue and product species could be monitored and analysed at the exhaust port by infrared absorption and gas chromatography equivalent technique. Entrained flow reactor or drop-tube furnace injects a stream of particles/gas to a preheated gas flow stream or directly to the tube furnace. The solid sample and gases are then sampled downstream for kinetic analysis.

With the advancement of thermal analytical tool, TGA is gaining popularity because of its ease of set up, small sample size and precise temperature control [67-70]. Advanced temperature control software is also available such as modulated TGA offered by TA Instruments. The weight is continuous monitored throughout the course of testing at a relatively low pressure or vacuum environment. The achievable resolution of the weight measurement is in the μg range. With precise measurements either in isothermal/non-isothermal mode or a user's defined temperature profile, reaction rate corresponding to the weight change can be obtained for the determination of kinetic parameters. TGA is also suitable for evaluating gasification processes where only gaseous products are generated. However for both TGA and entrained flow methods, only apparent kinetic parameters will be obtained by the kinetic analysis. The actual temperature and the mass diffusion resistance experienced by the sample have to be carefully evaluated for kinetic analysis.

Literature reveals a wide spectrum of rate parameters determined experimentally for the carbonaceous materials. The values of the parameters reported in the literature are very much dependent on the chemical structure of the carbon, the testing environment, the equipment used for the experiments and the type of computation analysis used for the kinetic analysis [64,71,72]. There is no established kinetic analysis specifically for the embedded carbon tape. Both for ease of use, flexibility and accuracy, the commonly used TGA method will be suitable and adequate for the analysis of the LTCC carbon burn off process.

In kinetic analysis, another essential aspect is the rate expression model to best describe the chemical reaction. Generally, for a simple irreversible reaction, power rate model with a specific reaction order could be applied [64, 73]. For a large variation in concentration of both reactants and products over a particle, Langmuir-Hinshelwood model focused on the elementary processes of chemisorptions and desorptions of surface mechanisms could be considered [35]. This is necessary when the precise rate data are to be estimated if extrapolation is required for a wider operation range. However, the elementary processes for the reaction process have to be well understood and the rate equation becomes complex when multicomponent gas species are involved.

2.6.2 LTCC Sintering Model

LTCC involves liquid phase sintering (LPS) in general. It is different from the traditional solid-state sintering as in LTCC a low temperature glass based system acted as a liquid phase for sintering [2]. This liquid phase helps to achieve densification at a lower temperature and at a reduced time. The liquid phase also helps to produce a denser sample after sintering. The sintering mechanism could be complicated by

reactive sintering and crystallization when the glass components start to react with the ceramic particles to develop crystallized phases. For glass-ceramics LTCC system, sintering is always coupled with crystallization [74]. Furthermore, additives are generally included to promote infiltration and wetting of glass for a ceramic filled glass matrix.

Conventional LPS was generally described by a three-stage model [75,76] and a pore filling model [77]. Three-stage model considers no grain growth in the densification. Pore closure is by contact flattening and final solid-state sintering. Contact flattening is a mass transfer process at the contact interface between grains by either diffusion or interfacial reaction. The material is transferred to the surface of the neck through a liquid film when the particles are fully wetted by the liquid phase to minimize the surface energy. The densification continues over time with persistent reduction in pore size and grain shape change as long as the pores are present in the compact [78]. However, such a sintering phenomenon was not observed in real sintering. The densification rate predicted by this model is far slower than the real physical LPS system. At most, contact-flattening could only apply in the early stage of LPS for some specific systems with an initial dihedral angle of 0° between the particles and with low liquid phase volume.

Lee and Kang [77] developed a more realistic LPS model which focuses on liquid flow phenomena through series of experiments and observations. The sintering stages involved in the model are liquid coagulation, liquid redistribution and liquid pore filling. The major difference from the classical three-stage model is the instantaneous pore filling driven by differential pressure at the pore and solid surface due to the

continuous grain growth. However, it was very much developed based on a simple binary metal system. Glass based system such as LTCC, the sintering mechanism has not been extensively analysed. Most of the available literature was focused on development of new and novel material systems.

For LTCC, two general material systems were developed, namely ceramic filled glass composite and crystallisable/recrystallisable glass-ceramics system with no ceramics filler [1]. Ewsuk [79] proposed a combination of three-stage classic and pore fill model with a last stage of viscous flow for ceramic particle filled glass system. LTCC with crystallisable glass-ceramics should also behave as a viscous flow dominant sintering system. Thus in general, LTCC is considered a LPS system with viscous flow as a major driving force for densification [80].

Heraus HL2000 LTCC [15], the system selected for the present study, has a unique 3-layer structure. The top and bottom layers are a glass/ceramics LTCC system, with the centre layer a refractory constrained layer. It is a reactive alkaline-silicate glass ceramic composite system. Borosilicate glass reacts with alumina and titania fillers as a modifier [81] to form a stable crystalline phase. This will result in a low dielectric constant and improved mechanical properties. As the viscosity decreases during sintering, the glass phase starts to wet and react with the alumina fillers. At the same time, the glass phase infiltrates the refractory constrained ceramic layer assisted by the wetting agent. With this constrained layer, this tape system is able to achieve near zero-shrinkage in both the X and Y directions but it suffers a high shrinkage in the thickness direction.

For LPS involving complex low temperature glass system as a flux agent with ceramic component, the mechanism could be complicated. To derive a theoretical model will be rather challenging. Alternatively, a practical approach of determining the sintering kinetics may be adopted. Sintering master curve [82] was developed based on a combined-stage sintering model [83] for predicting the sintering density under any arbitrary firing profile. Combined-stage model allows the conventional three-stage model to be used in sintering modelling from the beginning to the end of sintering by considering the scale and geometry parameters. The master sintering curve could be generated along with the density data obtained from linear shrinkage measurements under different heating profiles and temperature-time integral with a known or predicted activation energy. However this approach is applicable for a single diffusion mechanism of solid-state sintering. The microstructure and the scaling parameters are assumed to be functions of density only.

Mohanram et al [84] proposed a variant of master sintering curve based on the measurements of uniaxial viscosity of LTCC where viscous sintering is the dominant mechanism. The obtained activation energies for the commercial LTCC systems are comparable with those values obtained based on the sintering master curves. However, a sintering viscosity model complete with contribution from the competing effects of crystallisation will still require a knowledge of the loading of filler particle and shrinkage anisotropy.

Among the practical approaches, thermokinetic model using solid-state reaction models to describe the sintering process has been reported [85,86]. It is based on a chemical reaction kinetic computational analysis for a thermally stimulated process. The rate

data were extracted from the dilatometry or TMA. It is a computation method allowing the kinetic parameters to be obtained for subsequent predictions without having to delve into the details of the actual mechanism.

Due to the complexity of LTCC, a practical approach using the thermokinetic model will be a promising approach. It reduces the uncertainty of using a classical model that has to be tailored to the specific material system. The classical model always required rigorous systematic experimental and mathematical analyses and formulation in order to cater for the various operational variables such as grain size, compaction between cast sheet, environments, etc. In many situations, this approach is rather impractical to be realised.

2.6.3 Porous Medium Model

Representative elemental volume (REV) approach involves the integration of conservation equations over the REV. REV is the smallest differential volume providing statistically meaningful local average properties. It leads to a more rigorous treatment of transport problems associated with a porous medium. The conservation equations have to be structured as volume average variables using various averaging theorems [88-90] seeking for a solution based on the definition of intrinsic phase volume average. Intrinsic phase volume average is the phase variable volume integral function over the phase volume instead of the averaging volume. This intrinsic phase volume variable corresponds better to the measured value. Although averaging method provides a more rigorous solution, the closure of conservation equations for a specific process are always not available without much simplification with assumptions [91]. This is due to the complexity of the inter-pore and intra-pore fluid dynamic interaction.

There are also impending issues on the precise physical meaning of the volume average variables. For example, the volume averaged temperature has no precise meaning in the thermodynamic point of view but was shown to be significant in non-isothermal applications [92]. It was also shown in the literature that there are deficiencies in the application of Darcy's pressure for two-phase flow [93]. The difference in distance between the centroids of phases and the averaging volume due to pore gradient subjected to multiple phase flow would require a redefinition of the classical intrinsic phase volume average. As such, different average operator such as centroid-corrected phase averaging has to be employed.

Most recently, Gary and Miller [94-96] explored having a consistent macroscale model for a porous medium based on the thermodynamically constrained averaging theory approach. This framework based on entropy inequality will have no ambiguity about the definition of the phase quantity at a larger scale for the system of interest. This approach should be applicable in general across a continuum of different scales. Although it has been demonstrated mathematically, it is still in a developmental stage and its practical implementation is yet to be tested.

A straight forward formulation is to use a continuum piece-wise approach, and with consideration of the effects of porosity for the reduced cross-sectional flow area and the tortuosity factor for the increased diffusion length due to the tortuous paths of a physical porous solid structure. Effective values representing the contributions from the different phases using the rule of mixture will be employed for properties such as diffusivity, thermal conductivity, and heat capacity. This similar approach has been demonstrated in many other investigations with reasonable good results [87]. The

apparent shortcomings are a loss of detailed microscopic configuration of the phase to phase boundaries and the quantity variations within phases. Using this approach, the results obtained are very much a local average similar to the superficial phase volume in the REV approach. From a practical perspective, this approach is deemed to have the potential to provide sufficient accuracy and details.

2.6.4 Multicomponent Model

Since a carbon burn-off process is conducted in air (a gas mixture), the multicomponent effect has to be considered. Maxwell-Stefan (MS) equation is commonly used when mass transfer involves a concentrated solution or a gas mixture with concentrations of species of the same order of magnitude. At this condition, all species are expected to interact with each other and itself. Curtiss and Bird [97,98] have derived the MS equation based on entropy balance equation. The system is assumed to be in thermodynamical equilibrium so that the set of equilibrium equations could be applied locally within the system for mathematical manipulations and simplifications. A set of unique expressions were derived to express mass flux as a linear combination of concentration gradients that could be incorporated in the convection and diffusion equations. This approach could easily be implemented numerically.

When the species of the gas mixture have nearly equal binary diffusion coefficients such as the O_2-N_2-CO system applicable to the present investigation, the interactions of species are very minimal; the effective diffusivity approach would be appropriate [99]. The effective diffusivity approach which formulates the multicomponent mass diffusion equations with a simple binary Fick's diffusivity, greatly reduces the mathematical complexity. However, this Fick's diffusivity is referring to a pseudo binary diffusivity

of a species in the gas mixture. The expression for the effective diffusivity could be referred to the formulation derived by Wilke [100] for the viscosity equation for a gas mixture. This approach is also applicable for practical applications where one of the components is in large excess in a dilute mixture.

2.7 Concluding Remarks

Various LTCC embedded structuring technique was reviewed. The most promising method is by employing fugitive carbon to support the structure both in lamination and sintering stages. Carbon leaves virtually no residue and is the ultimate requirement for practical use especially in high performance electronic applications.

A specific embedded carbon burn-off model in LTCC was not available. A promising approach is to build the process model upon the convection and diffusion equations with the respective models of carbon burn-off and LTCC sintering containing the reaction terms. The functional variables are related by physical constitutive equations or empirical relationships. After reviewing the various models, it appears to be feasible to have a LTCC carbon burn-off model based on a volume reaction model with a power rate model for carbon burn-off. The significance of catalytic reaction in carbon burn-off should not be ignored and has to be investigated. While for LTCC sintering model, a practical approach of using thermokinetic solid-state model will be a promising approach. All kinetic parameters could be determined physically in a relatively simple manner by employing thermal analysis tools of TGA and TMA.

Chapter 3

EXPERIMENTAL KINETICS ANALYSIS

For the need of process modelling, the kinetic parameters for carbon burn-off and LTCC sintering are essential. The kinetic parameters will be experimentally determined by thermal analytical tools and analysis.

Carbon could exist in many forms. However, for this investigation, a commercial carbon black tape cast in sheet form was used as it is compatible to the LTCC tapes investigated. The carbon black contained in the tape is amorphous, isotropic, nano-sized carbon near spherical grain. It is cast and blended with binder and plasticizer with a special mixing method for a homogeneous well dispersed carbon tape. The carbon black was purified by cycles of thermal treatments to ensure complete residue free after burn-off. Under microscopic examination, see Figure 3-1, it appears as spherical conglomerates of small carbon grains. The mean carbon particle size is approximately 762 nm by light scattering technique (Zetasizer Nano ZS).

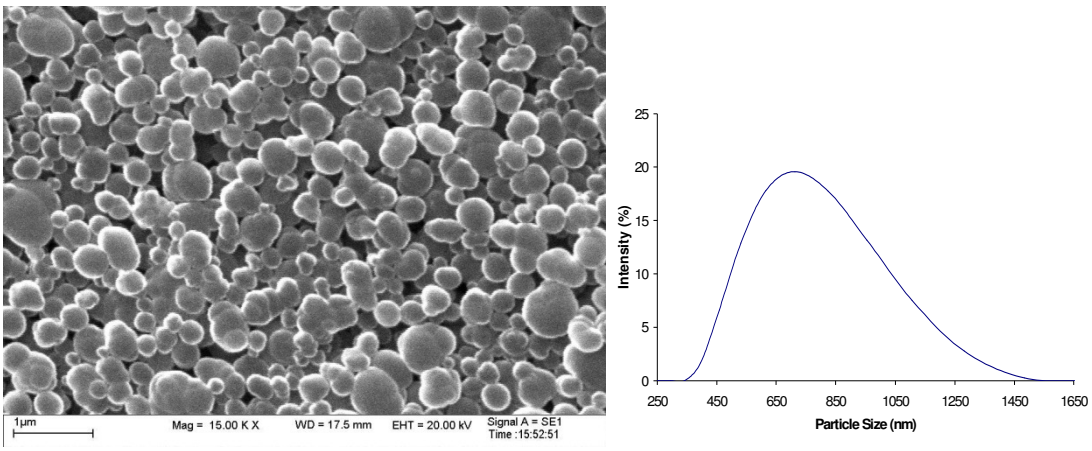

Figure 3-1 Carbon tape (after debinding) at high magnification with mean particle size of 748 nm using light scattering technique.

Carbon burn-off reaction is chemically simple. It has simple chemical equations when carbon reacts with O_2. However, the reaction mechanism becomes complex when it reacts at different temperature range as reported by Walker et al [55]. Carbon burn-off reaction rate changes with temperature and could be classified into three temperature zones. At the low temperature zone (Zone I), the burn-off is controlled by chemical reactivity of the carbon. The reaction is relatively slow and the reactant gas supply is always sufficient. The reaction is taking place throughout the volume of the sample and the concentration of the reactant is relatively constant throughout the reaction process. The product is always CO_2 when reacted with O_2. This is the ideal zone where intrinsic kinetic parameters of carbon burn-off should be determined. At the high temperature zone (Zone III), it is surface reaction controlled. The reaction is so fast that all the reactions occur at the surface and all the reactants are consumed at the surface. The product gases in this range will be dominated by CO when carbon reacts with O_2. At the intermediate temperature zone (Zone II), it is the diffusion and chemical controlled competitive reaction. Carbon burn-off rate could also be structurally affected particularly by the pore structure. The burn-off rate increases due the increase in pore surface area resulted from initial pore generation. The burn-off rate reduces after reaching the maxima by subsequent pore coalescing [45, 46].

Catalytic activities by most metals, metal oxides and salts were reported to significantly affect the reaction rate of carbon burn-off [64]. Some mineral oxides such as PbO, Cu_2O, Fe_2O_3 are strong active catalysts, while phosphorus-containing compounds such as $Al_2O_3.P_2O_5$ appears to be inhibitors for carbon burn-off [57-60]. The reaction mechanisms and its interactions with the vast variety of carbon structure are complex.

In addition, the reaction mechanism changes with reaction temperature and is further complicated by mass and pore diffusions during burn-off.

Indeed, an appropriate model which is sufficiently descriptive for this application of embedded carbon in LTCC is yet to be developed. Before arriving at a simple, but sufficiently accurate model, a representative burn-off process has to be first characterised. Over the years, researchers had attempted to use simple and quick techniques to characterise carbon combustion or burn-off process. One recent method is to use thermoanalytical method, in particular the Thermogravimetric Analysis (TGA). TGA had been employed for the kinetic study of carbon related materials especially in coal and coke [69, 101] in an effort to improve process control in carbon gasification and coal burning processes. Thermogravimetric analyser allows ease of operation and fast results generation. In addition, it has the added advantage that it requires only a minimum sample size typically in the range of mg. Accurate change of mass (resolution of 0.1 μg) as a function of temperature and time could be measured. Thus TGA is particularly useful for the analysis of mass change for thermally stimulated materials for studies of their evaporation, decomposition or interaction with a gaseous environment in a controlled manner. In this study, TGA will be utilized to determine the apparent kinetic parameters for carbon burn-off.

To model adequately the burn-off process of embedded carbon structure in LTCC, a good understanding of the LTCC sintering kinetics is also essential. The determination of its kinetic parameters, such as the common known kinetics triplets i.e. model function, activation energy & reaction rate constant, is necessary. LTCC sintering differs from the convectional solid state diffusion sintering. It involves liquid phase

sintering (LPS) to achieve densification at a relatively low temperature. This relatively low temperature sintering (achieved typically at 1073 – 1123 K) allows low loss conductive metals to be co-fired with the LTCC substrate.

LTCC is essentially designed for high performance electronic substrate as an alternative to HTCC system. One of the common metals used in LTCC is Ag which has a melting point of just about 1223 K. The others are Au, Cu & Pd. The commercially available LTCCs are generally glass ceramic composites consist of high temperature ceramic oxide such as Al_2O_3 and pristine or crystallized glass system to allow relatively low temperature firing at about 1123 K. The ceramic glass system used is specially formulated for high frequency requirements such as low loss dielectric, high thermal conductivity, and thermal expansion coefficient matching that of Si [1].

The sintering mechanism for LTCC is fairly complex; it may not conform to all the three classic stages associated with LPS model proposed by Kingery [75]. Furthermore, the three-stage classic model and theory could not adequately describe the fast densification rate associated with LPS system by contact-flattening and solid state sintering without grain growth. Lee and Kang [77] developed pore filling model based on series of experimental observations. It is a three stages sintering but based on the flow of liquid as liquid coagulation, redistribution and pore filling as the final stage of densification. It is more realistic than the three-stage model as the larger pore size is densified by instantaneous pore filling with grain growth.

Due to the LTCC high glass content of 40 - 80 vol. %, densification could possibly be achieved at the very initial stage when the matrix undergoing rearrangement where the

glass starts to flow [15,75]. The densification takes place as viscous flow sintering of glass as observed by Kemethmuller et at [80]. Viscous flow is the dominant driving force for LTCC sintering even though there is no wetting between the glass and the filler materials. As such, the process is very much dependent on the viscosity of the glass matrix during sintering. It becomes complicated when accompanied by glass associated crystallisation as crystallisation increases viscosity significantly.

In this study, Heraeus HL2000 LTCC system was specifically selected because of its unique construction. It is a self-constrained LTCC tape system [15,114]. It offers almost zero shrinkage in both the X & Y directions of less than 0.2 %. It is essentially a 3-layers LTCC tape structure produced by wet on wet special tape casting process with an inner high temperature ceramic constraint layer for achieving very low shrinkage for the top and bottom LTCC layers. The outer top and bottom layers have a LTCC composition of crystalline glass ceramics composite.

The sintering mechanism of Heraeus HL2000 LTCC system is as complex as most of the liquid phase sintering with densification occurred by viscous flow. Further complication is introduced by the existence of the constrained layer. During sintering, the glass powder coalescences and melt infiltrates within the composite matrix but wet over the constrained layer to achieve self-constrained zero shrinkage. To understand fully the kinetics of LTCC sintering, important factors for glass viscous sintering, such as sintering viscosity, surface tension and particle size, have to be determined. The interfacial mismatch stress building up during constrained sintering resulted from the wetting of low temperature glass between the LTCC and constrained layer [115-118] is also required.

The values of some of these sintering parameters may not be available and difficult to be measured experimentally and accurately. For a simple but practical approach, thermal analytical method was adopted in this investigation to estimate the required sintering kinetic properties from a solid state first order reaction model with respect to the degree of shrinkage. The linear shrinkage obtained from the thermal analytical method is assumed to be of sufficient accuracy to describe the densification process and no additional densification occurred after the end of shrinkage.

Among the thermal analytical methods, high temperature dilatometry has been commonly used not only for the quantitative evaluation of sintering kinetics but also for an in-depth study of sintering behaviour for mineral reaction, structural variation of raw materials, plasticizers and binding materials for ceramic processing [85,119]. In particular, dynamic dilatometry has been demonstrated for the study of densification behaviour of reactive bonded LTCC material [120,121]. Sintering kinetics is generally derived from the shrinkage curve under some heating programmes from the dilatometer.

In this investigation, instead of using dilatometer, thermal mechanical analyser (TMA) was employed. TMA measures the change in length of the sample with temperature and time as the dilatometer. It usually has a lower operating temperature range (< 1273 K) and short stroke length [122]. As the sintering temperature of the LTCC studied in this investigation is less than 1123 K and the sample thickness is in the range of 1 to 5 mm, TMA is thus well suited for sintering shrinkage evaluation for LTCC densification. If the LTCC shrinkage kinetics is assumed to be fully aligned with the sintering kinetics, a simple TMA curve will be able to characterise the sintering kinetics.

3.1 Formulation of Rate Equations

3.1.1 Carbon Burn-off Kinetics

Carbon burnout in air could be described in a major single step irreversible chemical equation with two main primary products of CO_2 and CO [55,102,103],

$$aC + b0_2 \overset{R_v}{\rightarrow} cCO + dCO_2 \tag{3.1}$$

The stoichiometric coefficients could be expressed in term of η, the product ratio of CO/CO_2,

$$a = \frac{2\eta+2}{\eta+2}, b = 1, c = \frac{2\eta}{\eta+2}, d = \frac{2}{\eta+2} \tag{3.2}$$

Based on Togoni's [104] experimental investigations, η (= CO/CO_2) obeys an exponential relationship and is dependent on the temperature and O_2 gas pressure at which it is burning off,

$$\eta = \left[Aexp^{(3070/T)}\right]^{-1} \tag{3.3}$$

Where,

$$A = 0.02\left(\frac{P_{O_2}}{1x10^5}\right)^{0.21} \tag{3.4}$$

The possible gasification of carbon by CO_2 at which the reaction rate is far slower than the reaction by O_2 is neglected in the above equations. For the gas phase oxidation of

CO, which is happening mostly at the higher temperature (> 1273 K) is beyond the temperature range of this investigation [55,104], will also not be considered.

As carbon burn-off with a net transfer of solid carbon is most conveniently be expressed in mass unit, the carbon reaction rate in mass concentration will be expressed in mass fraction instead of the usual molar concentration for most of the chemical reactions. The reaction rate equation based on the reaction rate of O_2 was expressed as a first order reaction i.e. reaction order equals to 1 [60,64],

$$R_v = R_{O_2} = k_c \rho_g w_{O_2} \tag{3.5}$$

Where k_c is the reaction rate constant for carbon reaction, $\rho_g$is the density of the total gas phase, $w_{O_2}$is the mass fraction of O_2

Indeed, researchers had attempted to determine the reaction order for carbon oxidation reaction. However, accurate determination has been difficult and the reaction order determined ranged from 0 to 1 depending on experimental conditions [64]. To complicate the matter, it might involve not only a single but multi-step reaction. Nonetheless, a first order reaction assumption has been widely used for the burn off reaction. From a practical application consideration, it is simple and easy to apply in complex multicomponent coupling system where coupling with diffusion and convection together with heat transfer equations is required.

With the relationship of reaction rates for each component [105] written as,

$$\frac{-R_{O_2}}{1} = \frac{-R_C}{a} = \frac{R_{CO}}{c} = \frac{R_{CO_2}}{d} \tag{3.6}$$

The reaction rate of carbon based on concentration of O_2 can be expressed as,

$$R_c = -aR_{O_2} = -ak_c\rho_g w_{O_2} \tag{3.7}$$

And ρ_g could relate to the equation of state as,

$$\rho_g = \frac{P_g M_g}{RT} \tag{3.8}$$

Where $P_g$is the total gas pressure, $M_g$is the molecular mass of the total gas phase, R is the universal gas constant.

Employing TGA for the kinetic analysis of carbon burn-off, the observed TGA rate equation of mass change with time could be expressed as [73],

$$\frac{dm_c}{dt} = \frac{R_c}{\rho_{cb}} m_c \tag{3.9}$$

Where m_c is the instantaneous mass of carbon during burn-off, R_c is the reaction rate of carbon, ρ_{cb} is the bulk density of the carbon

Substituting equation (3.7) into equation (3.9), one obtains,

$$\frac{dm_c}{dt} = -a\frac{k_c}{\rho_{cb}}\rho_g w_{O_2} m_c = -ak_c^*\rho_g w_{O_2} m_c \quad (3.10)$$

Where k_c^* is the apparent reaction rate constant.

By assuming the apparent reaction rate constant obeying Arrhenius relationship,

$$k_c^* = A_c^* exp^{-\frac{E_c}{RT}} \quad (3.11)$$

Where A_c^* is the apparent pre-exponential factor, $E_c$is the activation energy for the carbon burn-off.

The apparent rate constant k_c^* can be determined from the average carbon mass loss rate obtained experimentally from the TGA curve by rearranging equation (3.10),

$$k_c^* = \frac{\left(\frac{dm_c}{dt}\right)_{average}}{-a\rho_g w_{O_2}(m_c)_{t=0}} \quad (3.12)$$

One way to determine these kinetic parameters is to conduct isothermal TGA experiments at a set of specific isothermal temperatures. The mass loss rate could be approximated by the average mass loss rate from the start to end of reaction, with the total mass loss registered at total carbon burn-off,

$$\left(\frac{dm_c}{dt}\right)_{average} = \frac{Total\ burn{-}off\ mass}{Total\ burn{-}off\ time} \quad (3.13)$$

After determining the reaction rate constant at each isothermal temperature, and by taking logarithm on both sides of equation (3.11), the well known Arrhenius plot of $\ln(k_c^*)$ versus $1/T_{iso}$ is obtained,

$$\ln(k_c^*) = \ln(A_c^*) - \frac{E_c}{RT_{iso}} \quad (3.14)$$

The Arrhenius plot will appear as a straight line as described by equation (3.14) if there is no significant mass transfer effect from the sample [73]. The apparent kinetic parameters, particularly for the embedded carbon burn-off process, which is E_c and A_c^*, could then be calculated from the values of the slope and intercept of this linear plot.

Alternatively, the kinetic parameters can be obtained from multiple non-isothermal TGA experiments using isoconversion methods [106-111]. Variable kinetic parameters over the course of burn-off will be obtained instead, i.e. the activation energy and pre-exponential factor will vary with the degree of carbon burn-off.

Assuming that there is no residue left after burn-off, the degree of conversion for carbon burn-off can be written as,

$$\alpha_c = \frac{m_{c0} - m_c}{m_{c0}} = 1 - \frac{m_c}{m_{c0}} \quad (3.15)$$

Where m_{c0} is the initial mass of carbon before burn-off or at t=0

By taking time derivative of equation (3.15), the rate of conversion for carbon burn-off can be expressed as the rate of carbon mass loss,

$$m_{c0}\frac{d\alpha_c}{dt} = -\frac{dm_c}{dt} \tag{3.16}$$

By substituting equation (3.10) into equation (3.16),

$$m_{c0}\frac{d\alpha_c}{dt} = ak_c^*\rho_g w_{O_2} m_c \tag{3.17}$$

By expressing m_c in term of conversion according to equation (3.15), the rate of conversion of carbon burn-off could be expressed as,

$$\frac{d\alpha_c}{dt} = ak_c^*\rho_g w_{O_2}(1-\alpha_c) \tag{3.18}$$

For experiments conducted at a constant heating rate, the instantaneous temperature could be expressed as,

$$T = T_0 + \beta t \tag{3.19}$$

Where β is the constant heating rate, T_o is the initial temperature.

Taking time derivative, one obtains,

$$\frac{dT}{dt} = \beta \tag{3.20}$$

By employing equation (3.8), (3.11) and (3.20), equation (3.18) becomes,

$$\frac{T\beta}{a(1-\alpha_c)}\frac{d\alpha_c}{dT} = \frac{A_c^* P_g M_g w_{O_2}}{R} exp^{-\frac{E_c}{RT}} \tag{3.21}$$

By taking logarithms on both sides of equation (3.21), it yields a linear equation that allows the determination of the isoconversion kinetic parameters,

$$ln\left[\frac{T\beta}{a(1-\alpha)}\frac{d\alpha_c}{dT}\right] = ln\left(\frac{A_c^* P_g M_g w_{O_2}}{R}\right) - \frac{E_c}{RT} \quad (3.22)$$

Plot of ln $\left[\frac{T\beta}{a(1-\alpha_c)}\frac{d\alpha_c}{dt}\right]$ vs $\frac{1}{T}$ will provide the gradient for the activation energy and the intercept for A_c^* after curve fitting with a straight line at each conversion level of carbon burn-off from multiple constant heating rates TGA experiments.

It should be also noted that in the approach here, a first order reaction model for carbon burn-off has been assumed which allows also the determination of the pre-exponential factor. A unique set of kinetic parameters is expected for each conversion level, with the activation energy and pre-exponential factor varying with the carbon burn-off.

3.1.2 LTCC Sintering Kinetics

Using thermokinetics approach [85,86], the general sintering kinetic of LTCC could be expressed as a pseudo solid state reaction as,

$$\frac{d\alpha_L}{dt} = k_L f(\alpha_L) \quad (3.23)$$

where $f(\alpha_L)$ is the reaction model function, α_L is the fractional shrinkage related to sintering and k_L is the reaction rate constant. k_L can be written as :

$$k_L = A_L \, exp\left(-\frac{E_L}{RT}\right) \quad (3.24)$$

Equation (4.2) is commonly referred as the Arrhenius rate equation, where A_L, E_L and R are respectively the pre-exponential factor, the activation energy and the universal gas constant.

A simple first order reaction model (explicit model) was adopted [85]. It is directly related to the shrinkage of LTCC. The number of layers of LTCC structure was assumed to have no bearing on the model constructed. It is further assumed that there is no chemical reaction with gas species.

$$f(\alpha_L) = (1 - \alpha_L) \tag{3.25}$$

HL2000 [15] used for the study is fully self-constrained in both X-Y directions; the only shrinkage is in Z (thickness) direction. The linear shrinkage measurement in Z direction could therefore be used directly as the sintering shrinkage. The linear shrinkage which derived from TMA with respect to length change is normalized as the fractional shrinkage as,

$$\alpha_L = \frac{L_0 - L}{L_0 - L_f} \tag{3.26}$$

$$\frac{d\alpha_L}{dT} = -\frac{1}{(L_0 - L_f)}\frac{dL}{dT} \tag{3.27}$$

where L, L_o, and L_f are respectively the instantaneous sample length during sintering, initial sample length before sintering, and the sample length at completion of the sintering.

$\frac{dL}{dT}$ is the derivative of TMA curve with respect to temperature and it could be obtained from the experimental TMA curve.

For experiments conducted at a constant heating rate, the instantaneous temperature could be expressed as,

$$T = T_0 + \beta t \tag{3.28}$$

Where β is the constant heating rate, T_o is the initial temperature.

Taking time derivative, one obtains,

$$\frac{dT}{dt} = \beta \tag{3.29}$$

With equation (3.24), (3.21) & (3.29), equation (3.23) can now be re-written as,

$$\beta\left(\frac{d\alpha_L}{dT}\right) = A_L(1-\alpha_L)\exp\left(-\frac{E_L}{RT}\right) \tag{3.30}$$

Linearised by taking logarithms on both sides,

$$ln\left(\frac{\beta}{1-\alpha}\frac{d\alpha_L}{dT}\right) = \ln(A_L) - \left(\frac{E_L}{R}\right)\left(\frac{1}{T}\right) \tag{3.31}$$

The reaction parameter may be determined from equation (3.31) with a single TMA curve for non-isothermal but constant heating rate experiment by plotting $ln\left(\frac{\beta}{1-\alpha}\frac{d\alpha_L}{dT}\right)$ against $\left(\frac{1}{T}\right)$. Activation energy E_L could be determined from the slope of the fitted

straight line i.e. $\left(\frac{E_L}{R}\right)$, while $\ln(A_L)$ is the value of the Y-intercept. For better statistical analysis, multiple heating rate TMA curves were included for the linear regression analysis. Non-isothermal approach is always more appropriate and convenient if the process is not highly sensitive to heating rate and the reaction mechanism remains the same throughout the course of reaction.

However, for isothermal experiments, the rate equation could also be expressed with respect to time as,

$$ln\left(\frac{1}{1-\alpha}\frac{d\alpha_L}{dt}\right) = \ln(A_L) - \left(\frac{E_L}{R}\right)\left(\frac{1}{T}\right) \quad (3.32)$$

Factors such as glass powder coalescences controlled by the particle size, viscosity and surface energy are not considered explicitly in this study. These factors are indeed the important factors that will greatly affect the sintering characteristic especially LTCC sintering is dominated by viscous flow. In this study, simple technique based on sintering shrinkage to estimate the complex sintering behaviours on the LTCC sintering has been employed. In fact by measuring sintering shrinkage for viscous flow dominant process, the effect of viscosity and other factors mentioned in the question have now been included and reflected as a shrinkage parameter, which can be employed directly in the model. Furthermore, HL2000 is a self constrained LTCC system, with shrinkage dominated in the direction of thickness. Thus by measuring the thickness shrinkage, the sintering behaviours could be well characterized. Indeed, with various advances in material development with additives added to improve densification, detailed modelling of sintering is difficult. Resorting to use phenomenological model couple with experimental results seems to be a viable and practical path, which is adopted in the current investigation.

3.2 Experimental

Sacrificial carbon for the fabrication of embedded LTCC structure normally comes in a form of paste or cast tape. Cast tape could be employed with certain advantages in that it is available in various standard thicknesses and is easier to handle. The drawback is that it requires careful cutting to the right shape and dimensions. In contrast, carbon paste has to be screen printed and is generally for thin layer application as a lift-off sacrificial layer. Thus, carbon tape is especially suited for large embedded cavity applications. To avoid large concentration gradient (reactant and product) caused by bulk and pore diffusion across the sample thickness, the thinnest carbon tape available commercially from Thickfilm Inc i.e. 0.05 mm (2 mil), was employed.

Due to the size limitation of the TGA sample pan, carbon tape was punched into a ∅6 mm disc with an average weight of about 2 – 3 mg. The 2 mil carbon tape was then laminated within 2 layers of 0.127mm (5 mil) thick ∅9 mm discs made of HL2000 LTCC tape, see Figure 3-2. The lamination was performed using a hot hydrostatic laminator at a pressure of 100 kg/cm^2 at 343 K for 10 min.

Carbon burn-off rate was well reported to be easily accelerated or retarded by many inorganic compounds such as metal oxides [57-60]. They act as a catalyst or inhibitor; a small amount will have a significant effect. As the composition of LTCC tape apparently contains metal oxides, they can have a significant effect on the reaction rate by just simply laminating the carbon layer with the LTCC layers. To include the LTCC discs for the carbon burn-off kinetic analysis is to access and to include the possible catalytic effect of carbon burn-off due to its intimate contact with the LTCC layers. This will yield more meaningful results. This is because the TGA sample prepared in

such a way will be representative to the actual fabrication of LTCC embedded structures, although it might differ from the actual size and the layer configuration of the structures having more layers of LTCC. Another aspect is the off-gas analysis of TGA for possible evaporation of metal oxides. LTCC contains a set of metal oxides as a glass system, and containing possibly low vapour temperature species. However, most metal oxides exist in the form of solid glass compounds. The glass system is formulated and melted into solid glass before crushed into powder and mixed with ceramic powder and additives. During sintering, the glass melts and fuses with ceramic powder to form a monolithic structure, and evaporation of metal oxides in this condition is unlikely. Literature has also no reported evaporation of metal oxides during sintering. Indeed, burn-off of carbon has been extensively reported to be the only product gas species of CO & CO_2. The product ratio of CO & CO_2 could be difference as it depends on the burn-off temperature; this has already been factored in the rate equation. Thus no off-analysis was conducted in this study.

For TGA experiments, a single layer of LTCC is used to minimize the possible external mass transfer resistance which will likely shift the burn-off to a competing reaction zone of chemical reaction and mass diffusion. This will complicate the kinetic analysis for the determination of the intrinsic properties. In addition, both LTCC and carbon tapes contain polymeric binder, additives and solvent. Thus, before conducting the TGA experiments, the sample was first debinded in a box furnace for 2 hours at 673 K with air preheating blower installed for sufficient air circulation under normal air environment. By doing so, it minimizes the interaction of the decomposition of polymeric blinder to the subsequent burn-off at a higher temperature, which could then complicate the kinetic analysis. Although it is assumed that the thermal debinding

cycle will not adversely affect the subsequent burn-off carbon behaviour, it might have some effect on the reaction properties of carbon. As such, the debinding profile was selected as the same profile for debinding the LTCC samples in production.

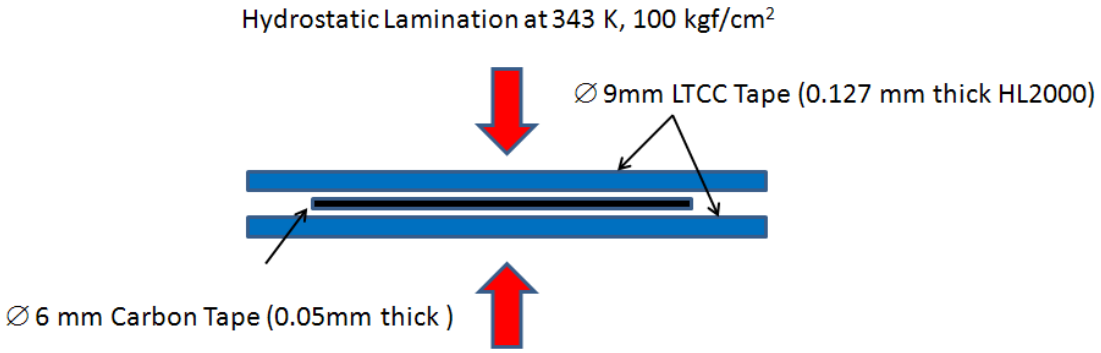

Figure 3-2 Embedded carbon sample configuration for TGA experiments.

The experiments were conducted in a TA Instrument model Q500 thermogravimetric analyser (Figure 3-3). The sample was placed in a platinum pan and first heated linearly at 20 K/min to the burn-off temperature of interest in an inert environment of N_2. After reaching the specific isothermal temperature, the sample gas was switched to dry pure air while holding the temperature constant until complete burn-off. The mass flow of pure air was controlled at 80 ml/min throughout the burn-off cycle. The burn-off temperatures were selected as 823 K, 848 K, 873 K, 898 K, 923 K, 948 K and 973 K to cover the whole spectrum of the possible burn-off temperatures related to LTCC sintering. However, the LTCC layers were also undergoing sintering during carbon burn-off. Thus care has to be taken in selecting the isothermal temperature to avoid seriously affecting the burn off rate caused by possible pore elimination of the LTCC layer. The mass loss as a function of time was recorded, with the derivative of mass loss with time computed simultaneously. The derivative was employed for the computation of the normalized degree of conversion of burn-off, which was used for

the determination of kinetic parameters. In addition, experiments with linear heating rates of 1 K/min, 3 K/min, 5 K/min, 10 K/min & 20 K/min were also conducted to provide the necessary data for the determination of the kinetic parameters using non-isothermal methods for isoconversion kinetic parameter analysis.

For TGA experiments, it is important to have accurate mass balance especially fugitive carbon is embedded in the LTCC. In order to have an accurate mass balance of the carbon burn-off gravitational analysis, the same configuration of blank LTCC was conducted as the baseline correction in identical experimental conditions. With the baseline of LTCC established, the TGA curve obtained could show just the burn-off of carbon. While for incomplete carbon burn-off, it was determined initially by comparing the total carbon burn-off weight to an average sample weight of about 30 samples after debinding. The carbon sample was prepared by a same set of die punch of ∅6 mm and the carbon was tape cast to have uniform thickness. Therefore a set of sample weights of ∅6 mm carbon tape was weighted after debinding. The average weight obtained should be representative to check for incomplete burn-off. Furthermore, the sample after TGA was pried open to check for carbon residue by subjecting it to another TGA run. For incomplete burn-off, the analysis of TGA with "pried" sample was used for calculation.

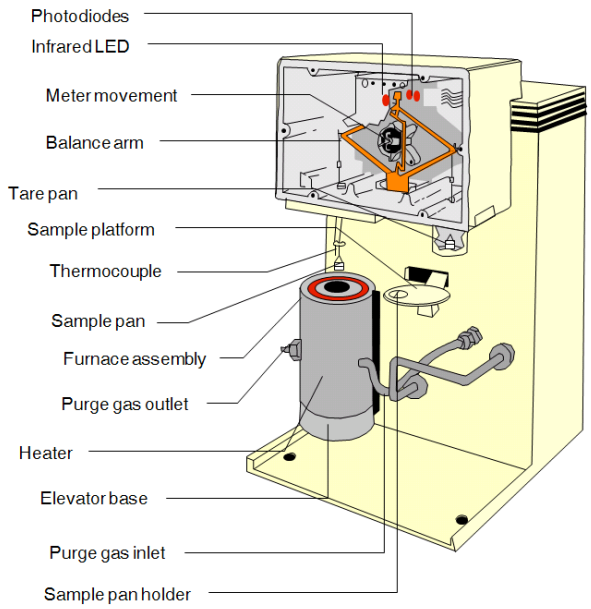

Figure 3-3 Schematic diagram showing the construction of TGA and the microbalance configuration (Extracted from TA Instrument training manual).

LTCC samples for sintering kinetic analysis were prepared from the HL2000, 0.127 mm (5 mil) thick green tape. A sample was first cut to size of ∅9 mm disc and stacked accordingly to 3, 6 or 9 layer structure. After hot hydrostatic laminated at 100 kg/m^2, 343 K, the sample was subjected to a debinding cycle at 673 K for 2 hours in a debinding furnace fitted with preheated air blower. This aims to completely drive off any solvent and polymer binder from the green tape. The debinded sample of 3, 6 or 9 layer structure had a sample height of 0.4 mm, 0.76 mm or 1.2 mm respectively. A TA Q400 TMA was set up with a standard expansion Quartz probe. The construction of the instrument and the standard expansion probe are shown in Figure 3-4. The sample was loaded and a constant loading of 0.05 N was applied to the sample to maintain consistent contact between the probe and the sample during testing. HL2000 is a self-constrained tape system with very low shrinkage at the X & Y directions. Thus measurements were taken at the Z-direction along which there would be shrinkages of more than 30 % with respect to the thickness. With this large shrinkage, any dimensional change would be recorded with good accuracy. Plot of length change with

temperature and time was recorded. Thermal expansion of the sample during heating was compensated from the thermal expansion coefficient (CTE) determined from the initial expansion of the sample. The CTE is assumed constant during the sintering process. These experiments were conducted to full densification under still air environment at different constant heating rates of 1 K/min, 3 K/min, 5 K/min and 10 K/min. The derivative of length change with temperature was also computed.

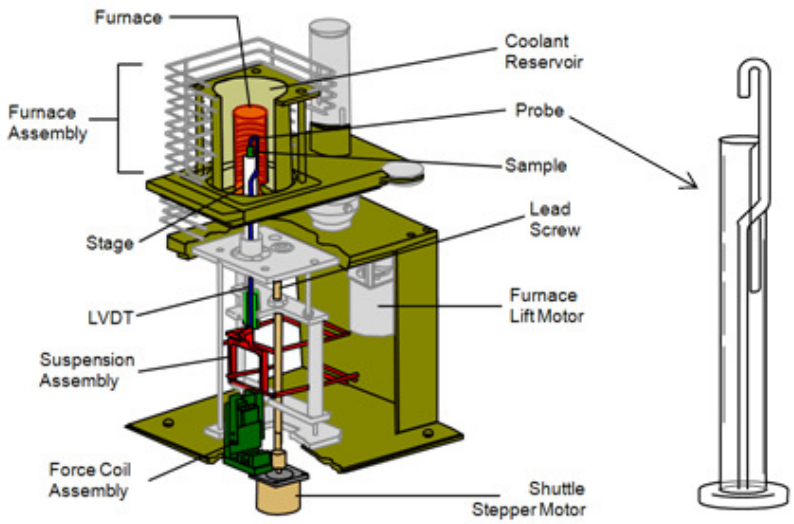

Figure 3-4 Schematic diagram showing construction of TMA and probe configuration of a standard expansion quartz probe (Extracted from TA Instrument training manual).

3.3 Results and Discussion

3.3.1 Carbon Burn-off Kinetics

The average mass loss rate was determined from the isothermal TGA curves. An example of isothermal TGA plots conducted at 923 K was shown in Figure 3-5. By assuming a linear mass loss rate for the burn-off, the estimated average mass loss rate curve can be determined graphically from the TGA curve, which is basically the average gradient measured from the starting to the end of burn-off. As compared to the method using initial mass loss rate [73], it is much easier. This is because the

identification of the point of the initial mass loss rate from the derivative of a TGA curve is difficult especially for carbon burn-off at high temperature. The initiation of burn-off is usually complex and unstable due to its inherent surface and edge defects resulted from the sources of the carbon. The burn-off will tend to be stable once the initial surface is removed.

The resulted Arrhenius plot of isothermal kinetic analysis is shown in Figure 3-6. For comparison, although the current focus is only on HL2000, the Arrhenius plots for a carbon tape, and carbon tapes embedded in other two commercial LTCCs, namely Dupont 951 and Ferro A6M LTCC tapes, were also determined. The results obtained indicate clearly that LTCC has effects on the carbon burn-off rate as none of the embedded carbon followed closely the carbon tape burn-off plot. Carbon embedded in HL2000 and Dupont951 shows catalytic carbon burn-off while Ferro A6M inhibits the carbon burn-off. The obtained activation energies and reaction rate constants are contained in Table 3-1. The effect of catalytic carbon burn-off is due to the intimate contact of LTCC and carbon layer. This close contact is the result of interpenetration of particles between the ceramics and carbon layer caused by hot lamination, a necessary step in LTCC fabrication.

The quantitative results expressed in standard oxides from X-ray Fluorescence Spectrometry analysis (XRF) using Shimadzu Lab Center XRF-1800 for LTCCs are shown in Table 3-2. All LTCCs contain several catalysts of reported metal oxides and also inhibitors for effective catalytic carbon burn-off [58, 60]. The combination of various catalysts resulted distinct burn-off rate for each LTCC system as compared to the carbon tape itself. For Dupont embedded carbon as shown in Figure 3-7, the TGA

curves at a constant heating rate of 10 K/min, carbon could completely burn-off at a lower temperature i.e. 50 K lower than the normal carbon tape. In contrast, for Ferro A6M tape, carbon burn-off was delayed by 55 K.

Hitherto there is no report on the significance of catalytic embedded carbon burn-off when interacting with LTCC's pore closure. Incomplete carbon burn-off may exist when pore closure is ahead of complete burn-off at higher sintering temperature ramp rate or for thicker LTCC layer. Further analysis of the Arrhenius plots as shown in Figure 3-6 revealed that Dupont and Heraus Tapes deviate from the linear trend at about 898 K, indicating strong mass resistance due to the faster burn-off rate where carbon burn-off shift the reaction to zone II or III i.e. mass diffusion zone. However, due to its retarded reaction rate, mass diffusion effect was not observed for Ferro tape even up to 973 K. These thin layers of LTCC covering the carbon had not significantly affected the burn-off characteristics; otherwise some incomplete burn-off at high isothermal temperatures due to complete pore closure of LTCC would be observed.

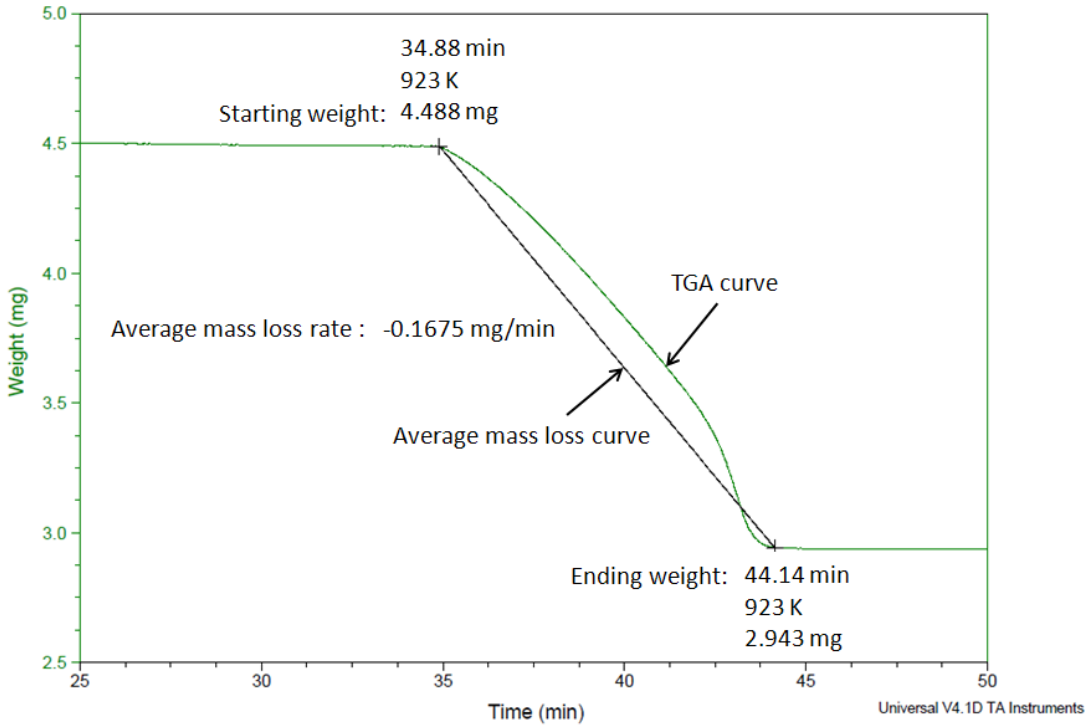

Figure 3-5 Example of average mass loss rate curve determined graphically from TGA curve for isothermal run at 923 K.

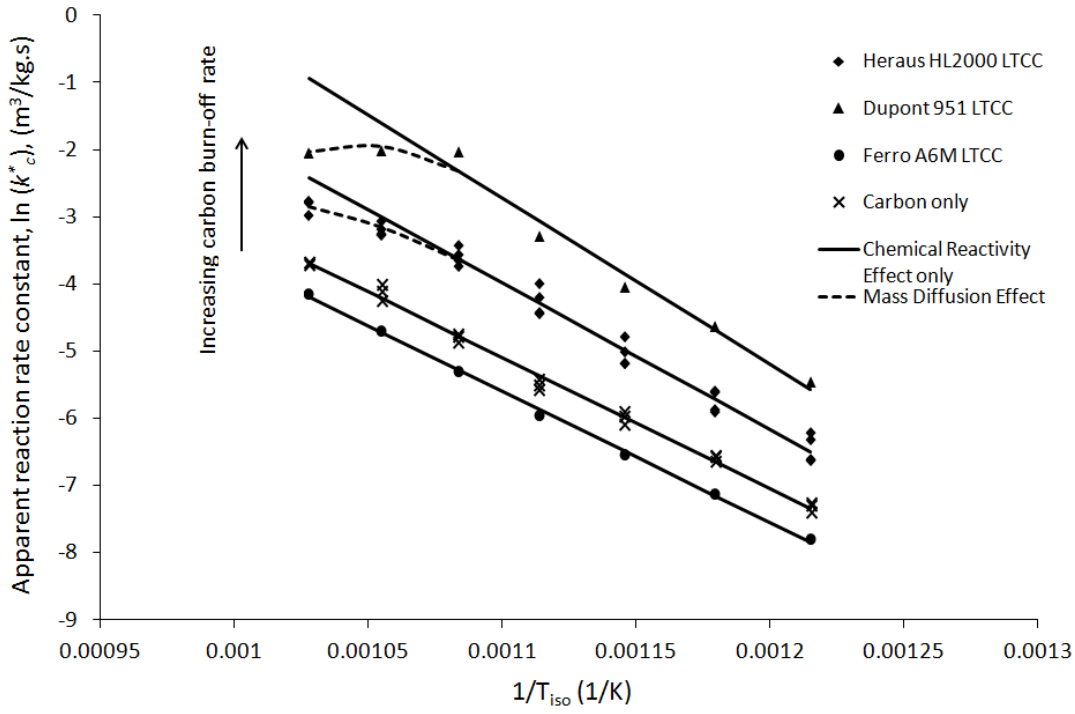

Figure 3-6 Arrhenius plots of embedded carbon with various commercial LTCC tape systems using isothermal kinetic analysis from 823 K to 973 K at intervals of 25 K. Dotted lines show trends of mass resistance effect.

Table 3-1 Calculated kinetic parameters from average mass loss curve.

Material Systems	Activation Energy (kJ/mol)	Apparent Pre-exponential Factor, $\ln(A_c^*)$, (m^3/kg.s)
Carbon Tape	155 ± 4	15.4 ± 0.5
Carbon embedded in Heraus HL2000 LTCC	181 ± 7	20.0 ± 1.0
Carbon embedded in Dupont 951 LTCC	206 ± 20	24.5 ± 2.7
Carbon embedded in Ferro A6M LTCC	156 ± 4	15.0 ± 0.5

Table 3-2 XRF analysis of LTCC systems based on standard oxides.

	LTCC Systems		
	Heraus HL2000	Dupont 951	Ferro A6M
Compounds	Content (wt %)		
Al_2O_3	36.51	39.41	0.30
SiO_2	34.05	39.92	48.99
CaO	10.25	4.56	49.48
PbO	-	12.34	-
SrO	6.64	-	0.03
BaO	4.59	-	-
TiO_2	3.86	0.04	-
K_2O	3.15	1.18	0.11
ZrO_2	-	-	0.69
Cr_2O_3	-	0.36	-
MgO	0.31	0.38	-
Co_2O_3	0.23	0.37	-
P_2O_5	0.21	-	0.16
Na_2O	0.11	1.39	0.05
Fe_2O_3	0.05	0.05	0.09
CeO_2	-	-	0.05
SO_3	0.04	-	0.05

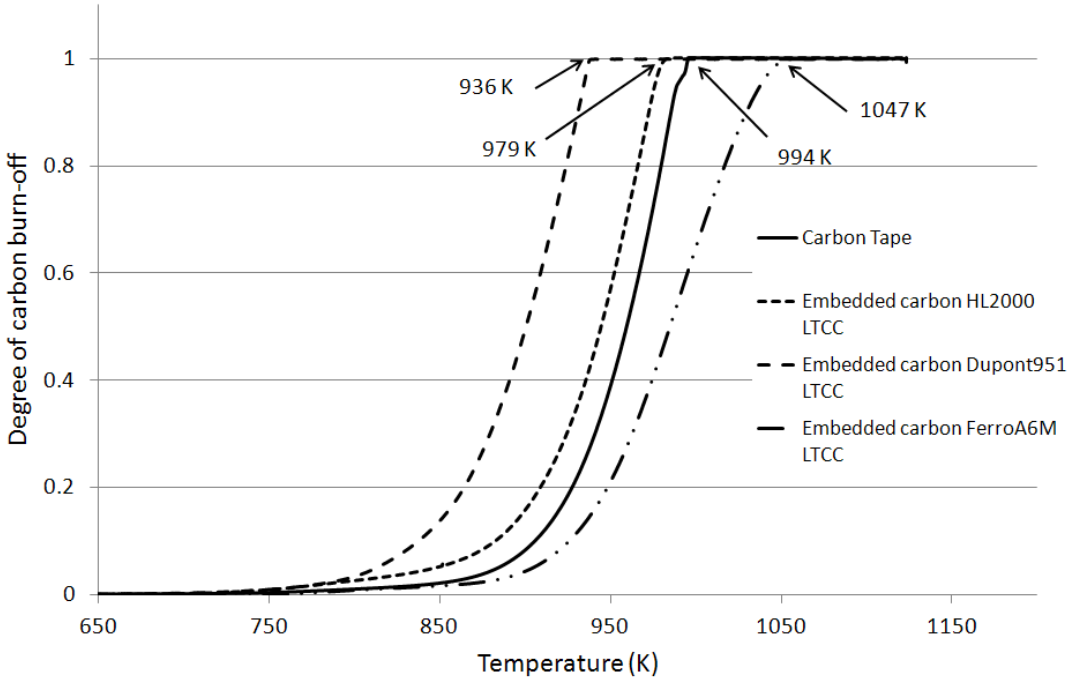

Figure 3-7 TGA plots with normalized degree of carbon tape burn-off at linear heating rate of 10 K/min for various embedded carbon LTCCs.

Alternatively, the variable kinetic parameters determined by isoconversion method but fitted with a first order reaction model for embedded carbon burn-off in HL2000 is shown in Figure 3-8. The kinetic parameters were determined at a conversion interval of 0.025. Activation energy varies in the range of 126 kJ/mol to 188 kJ/mol and gradually increases to a peak of 188 kJ/mol at 72.5 % of carbon burn-off. The same trend was observed in the pre-exponential factor which spans from 16 K/s – 26 K/s. The implication of variable kinetic parameters is complex and not well established; however, with increasing trend of activation energy, it could be an indication of competing reactions that could possibly occur during carbon burn-off [107-111].

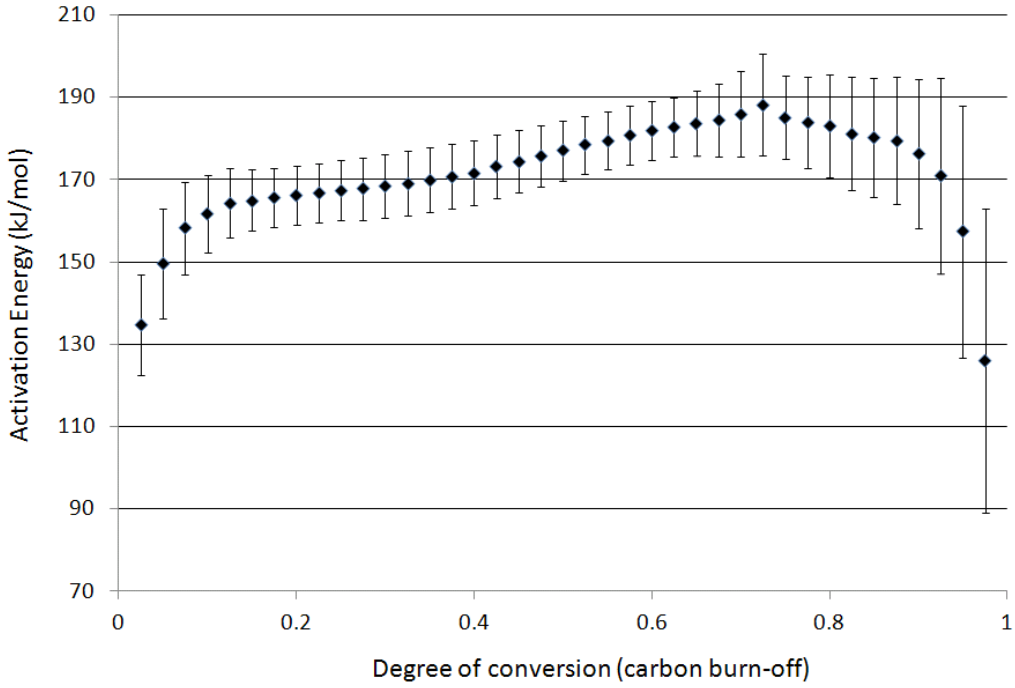

Figure 3-8 Variation of carbon burn-off activation energy with conversion with constant heating rate (non-isothermal) experiments. The error bar indicates the standard error resulted from the regression coefficient (slope) at each conversion level.

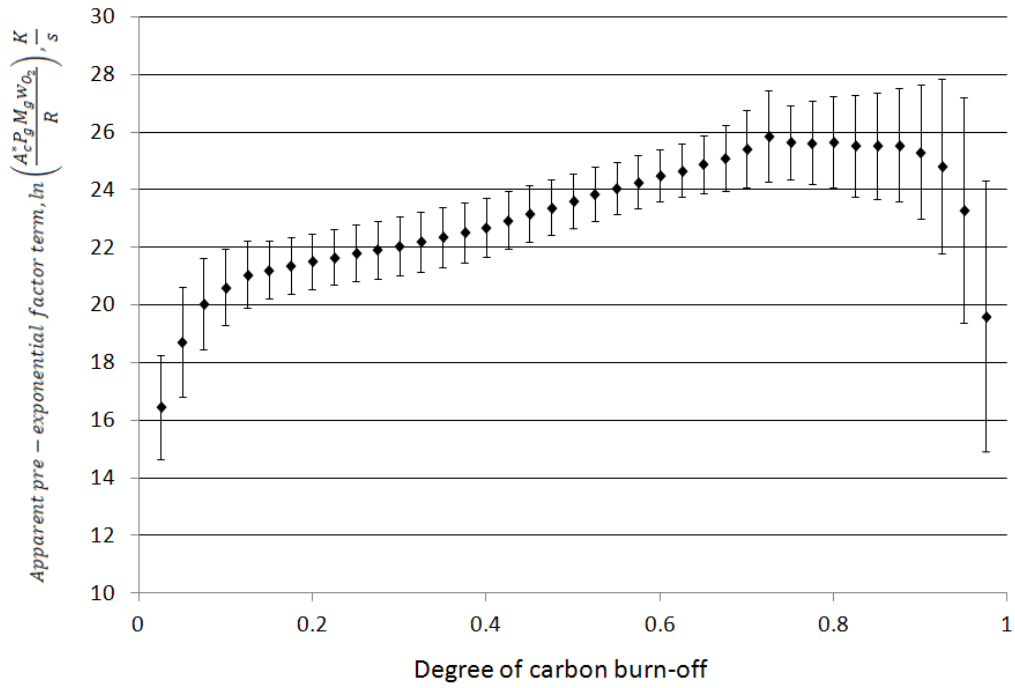

Figure 3-9 Variation of apparent pre-exponential factor term of carbon reaction kinetics with constant heating rate (non-isothermal) experiments. The error bar indicates the standard error resulted from the regression coefficient (Y-intercept) at each conversion level.

3.3.2 LTCC Sintering kinetics

The typical TMA curves obtained at various constant heating rates for HL2000 tape 9-layer structure are shown in Figure 3-10. The thermal expansion resulted from linear heating was compensated. As such, a relatively flat curve at the initial heating where there was no sintering taking place was observed. The thickness effect of LTCC sintering may not be significant as the maximum shrinkages obtained for the different layer structures are almost similar, namely 23 % – 24 % at 5 °C/min and 10 °C/min constant heating rates. Thus for LTCC sintering kinetic parameters, the thickness effect has not been included. It is interesting to note that heating rates did have an effect on the observed densification. The amount of shrinkage was larger at higher heating rate; this is due to early crystallisation or re-crystallization of glass components when sintered at low heating rate. Once the glass crystallized, the effective viscosity will increase significantly. The high viscosity will slow down further densification and resulted low shrinkage at the end of sintering cycle [84]. Sintering of LTCC at low heating rate will generally produce higher void content than at high heating rate. Figure 3-11 shows the normalized fractional shrinkage as required by the rate equation for the same data contained in Figure 3-10. All heating rates were assumed to reach full conversion or densification regardless of the different total linear shrinkage observed.

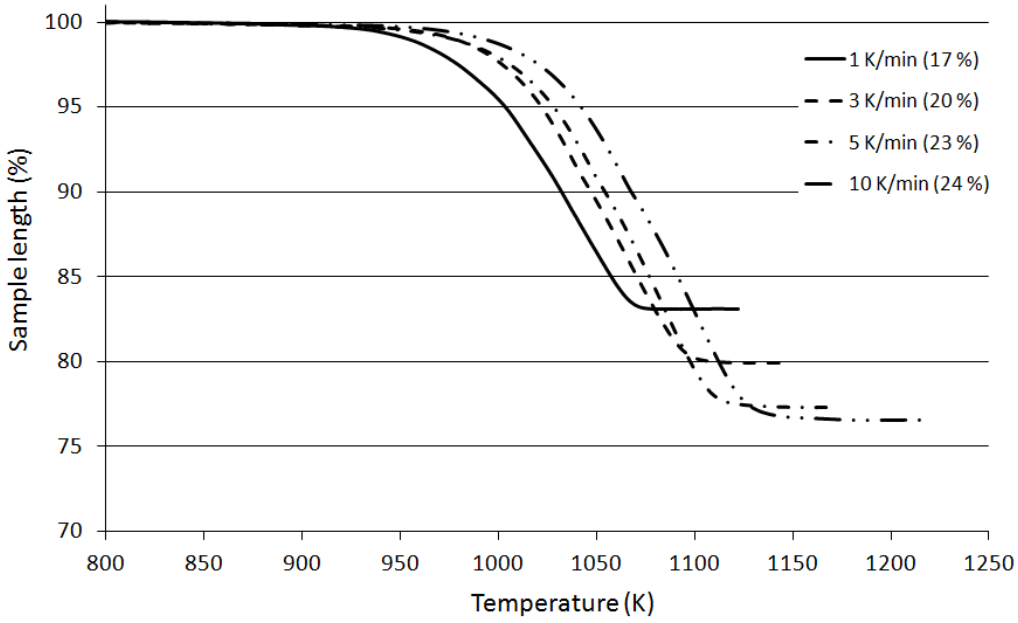

Figure 3-10 Typical TMA profile of 9-layers HL2000 at constant heating rates of 1, 3, 5 or 10 K/min. The maximum shrinkage is tabulated in bracket beside the legends indicating some dependency of heating rates.

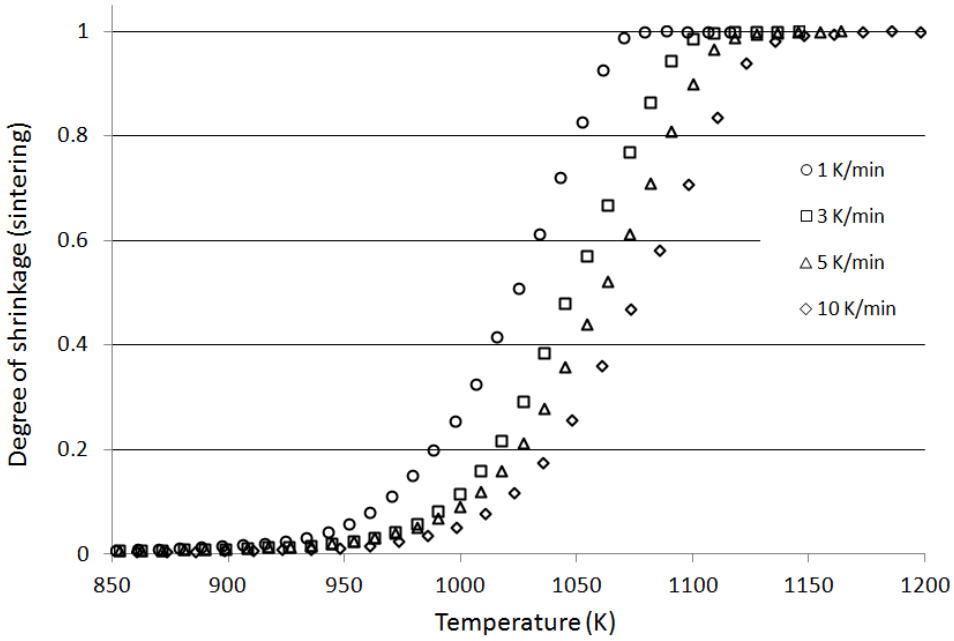

Figure 3-11 Normalized degree of sintering curve of 9-layer HL2000 at constant heating rates of 1, 3, 5 or 10 K/min.

Using non-isothermal analysis, the kinetic parameters could be determined by using a single run. The respective fitted linear plots established on 3, 6, and 9-layer LTCC structures with different constant heating rates are shown in Figures 3-12 to 3-15. The kinetic parameters are calculated based on equation (3.31) using the gradients and y-intercepts from the linear plots. The obtained kinetic parameters are summarized in Table 3-3. The activation energy obtained in this study for Heraus HL2000 system is in the range of 190 kJ/mol – 302 kJ/mol. This is comparable to the published values listed in Table 3-4. Results obtained indicate that the kinetics of LTCC is not independent of the heating rates. It shows trend of decreasing activation energy with increasing heating rates. This poses difficulty in determining the appropriate activation energy for modelling the LTCC sintering process.

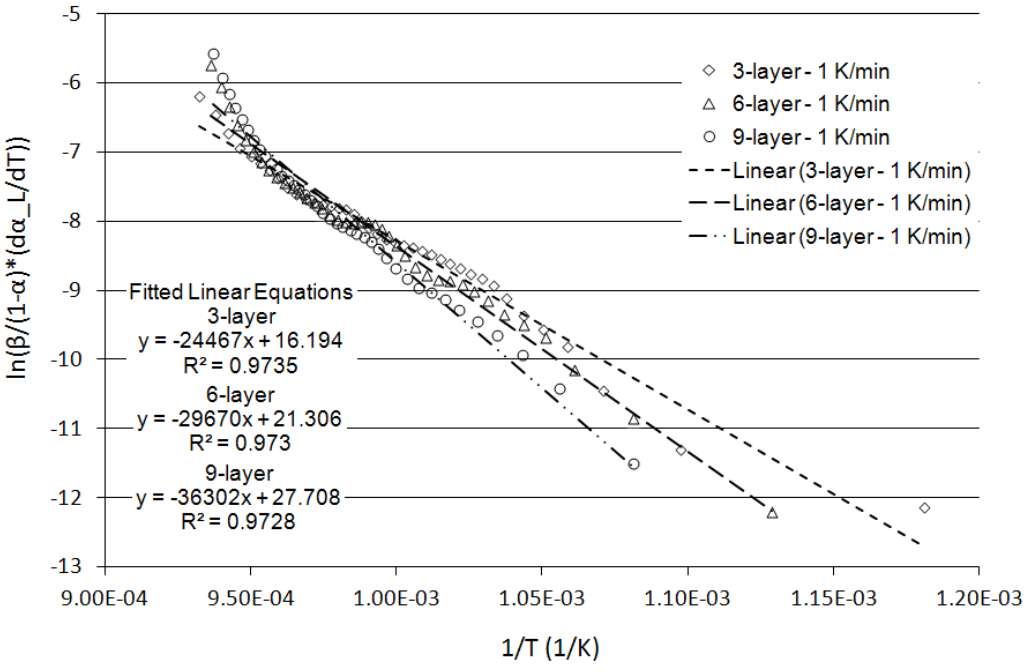

Figure 3-12 Single curve analysis at 1 K/min of 3, 6, 9-layer LTCC.

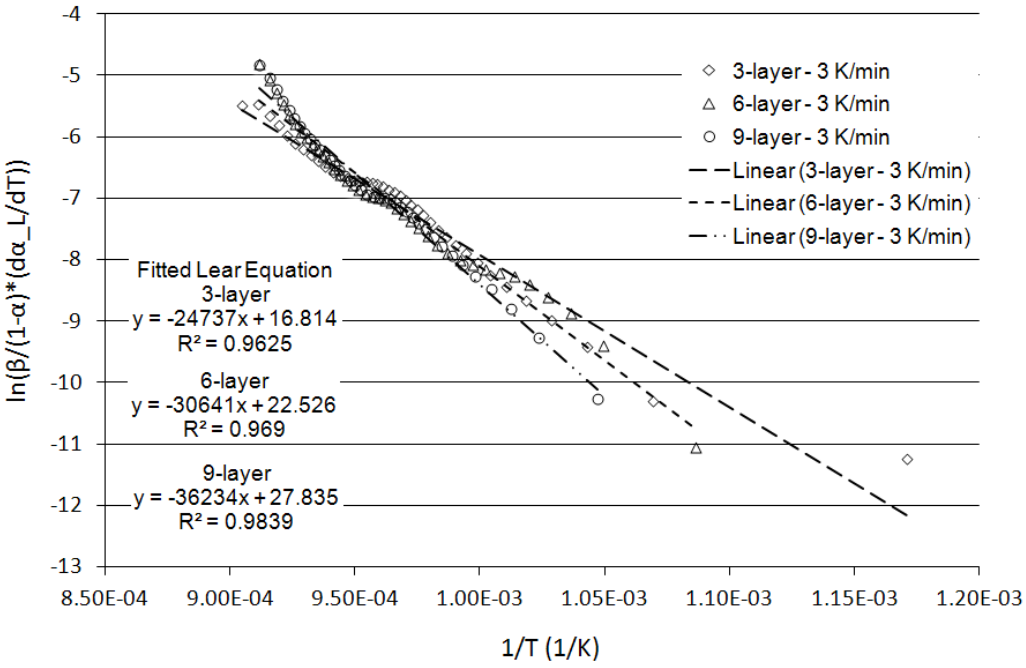

Figure 3-13 Single curve analysis at 3 K/min of 3, 6, 9-layer LTCC.

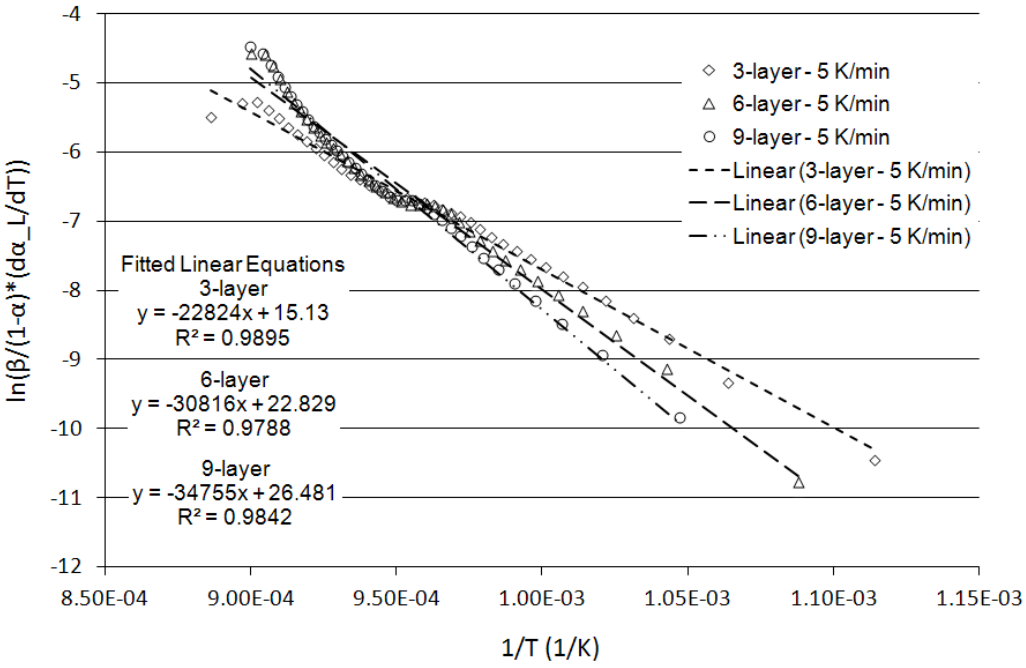

Figure 3-14 Single curve analysis at 5 K/min of 3, 6, 9-layer LTCC.

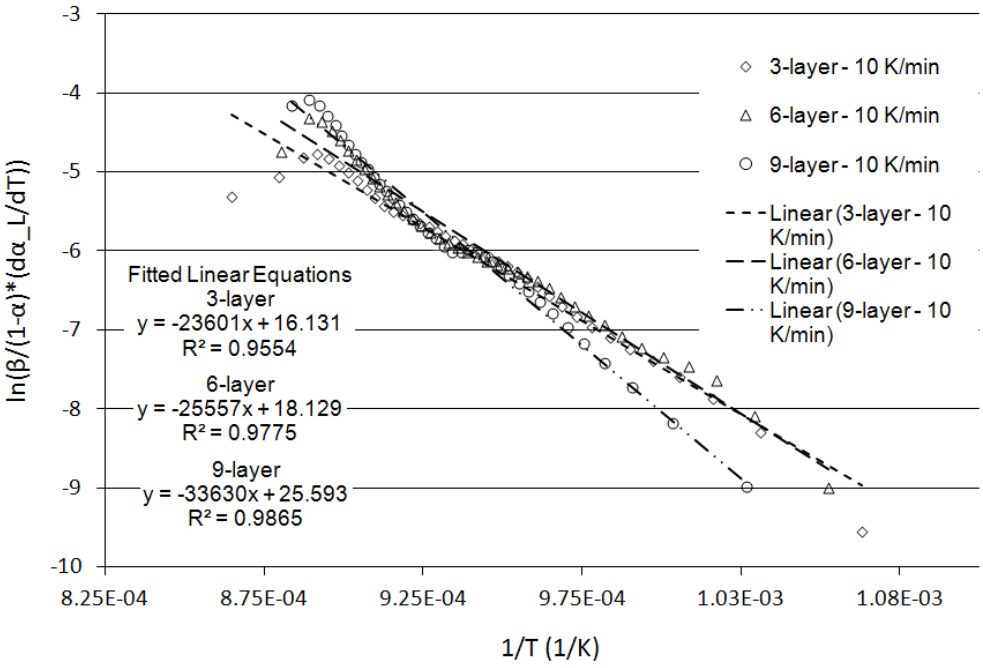

Figure 3-15 Single curve analysis at 10 K/min of 3, 6, 9-layer LTCC.

Table 3-3 Kinetic parameters obtained for constant heating rate using first order reaction model by linear curve fitting on single curve analysis for 3, 6 & 9 layers configuration of LTCC.

(a) 3-layer LTCC kinetic parameters

Heating Rate (K/min)	**Activation Energy (kJ/mol)**	**Pre-exponential Factor** $\ln(A_L)$ **(1/s)**
1	203 ± 5	16.2 ± 0.7
3	206 ± 7	16.8 ± 0.8
5	190 ± 3	15.5 ± 0.4
10	196 ± 7	16.1 ± 0.8

(b) 6-layer LTCC kinetic parameters

Heating Rate (K/min)	**Activation Energy (kJ/mol)**	**Pre-exponential Factor** $\ln(A_L)$ **(1/s)**
1	247 ± 7	21.3 ± 0.8
3	255 ± 8	22.5 ± 0.9
5	256 ± 6	22.8 ± 0.7
10	212 ± 5	18.1 ± 0.6

(c) 9-layer LTCC kinetic parameters

Heating Rate (K/min)	**Activation Energy (kJ/mol)**	**Pre-exponential Factor** $\ln(A_L)$ **(1/s)**
1	302 ± 8	27.7 ± 1.0
3	301 ± 6	27.8 ± 0.7
5	289 ± 6	26.5 ± 0.7
10	280 ± 5	25.6 ± 0.6

Table 3-4 Published activation energies for sintering of LTCC.

Activation Energy (kJ/mol)	**Material System**	**References**
375 ± 30	Dupont 951	[84]
450 ± 10	Ferro A6M	[84]
250	Heraus CT2000	[84]
325	Dupont 951	[155]
175 - 280	Ceramic filled Borosilicate glass	[156]

To avoid biases of selecting an activation energy and pre-exponential value from a single heating rate, and noting that the differences between values obtained with different heating rates and configurations are not excessive, an average activation energy value obtained by a simple liner regression line from data obtained for all the heating rates from all the different configurations is adopted. The result is shown in Figure 3-16.

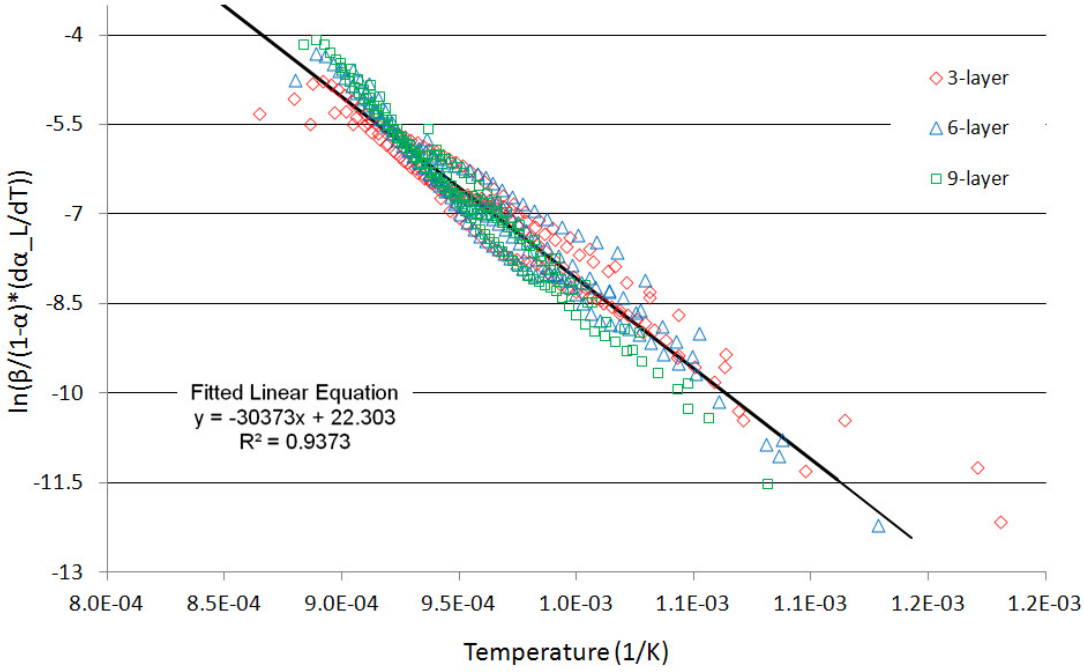

Figure 3-16 Kinetic analysis with first order reaction model on multiple heating rates for 3, 6, 9-layer LTCC.

The kinetic parameters obtained is,

$$\ln(A_L) = 22.3 \pm 0.4\ s^{-1},\ E_L = 253 \pm 3\ {}^{kJ}/_{mol}$$

with the standard errors of the linear regression analysis on the coefficient and Y-intercept.

Fitting of two linear curves to the plots is possible. This will result in two different activation energies governed by two reaction steps for the LTCC sintering kinetics. These two reaction steps could connect in series or parallel by similar or entirely different reaction models. The complexity of the analysis will increase significantly, and models based on two activation energies are difficult to be solved. The approximation adopted by fitting only a single linear curve for a first order reaction model provides good approximation, especially for the initial/intermediate stage of sintering which accounts for the bulk of the sintering cycle. Only at the very final stage of sintering (the last few experimental points) seems to have higher activation energy, thus a different linear plot is necessary. However, by ignoring this different linear plot will not introduce significant error as the final stage accounts for an insignificant fraction of sintering time.

3.3.3 Validation of Kinetic Models

(a) Carbon Burn-off Kinetic Model

To validate the assumed kinetic model with obtained kinetic parameters for kinetic analyses, equation (3.18) was integrated with respect to *t*, and solved by imposing initial conditions of $\alpha_C = 0$, $t = 0$, to obtain,

$$\ln(1-\alpha_C) = -\left(a\rho_g w_{O_2} A_c^* \mathrm{e}^{-\frac{E_C}{R_u T}}\right) t \qquad (3.33)$$

Chemical reaction controlled condition will be assumed with uniform temperature and concentration of reactant throughout the sample volume. The concentration of O_2 will be taken as the free stream air i.e. mass fraction of 0.21 for O_2 at one atmospheric pressure. By substituting the values of E_c and k_{0c}^* from Table 3-1 or Figure 3-8 & 3-9

and a firing profile, the carbon burn-off curve could be reproduced by solving the value, α_c.

(i) Kinetic analysis using average mass loss

As an example, the burn-off curves were reproduced at one of the experimental heating rates of 10 K/min based on the kinetic parameters obtained by using average mass loss from Table 3-1. The burn-off plots together with the experimental normalized TGA curves are shown in Figure 3-17. As compared to the various LTCC embedded carbons, the calculated carbon burn-off curves do not represent well the measured values and the burn-off path is also not modelled well. The difference, if compared to the burn-off time at complete burn-off is in the range of 98 s – 354 s.

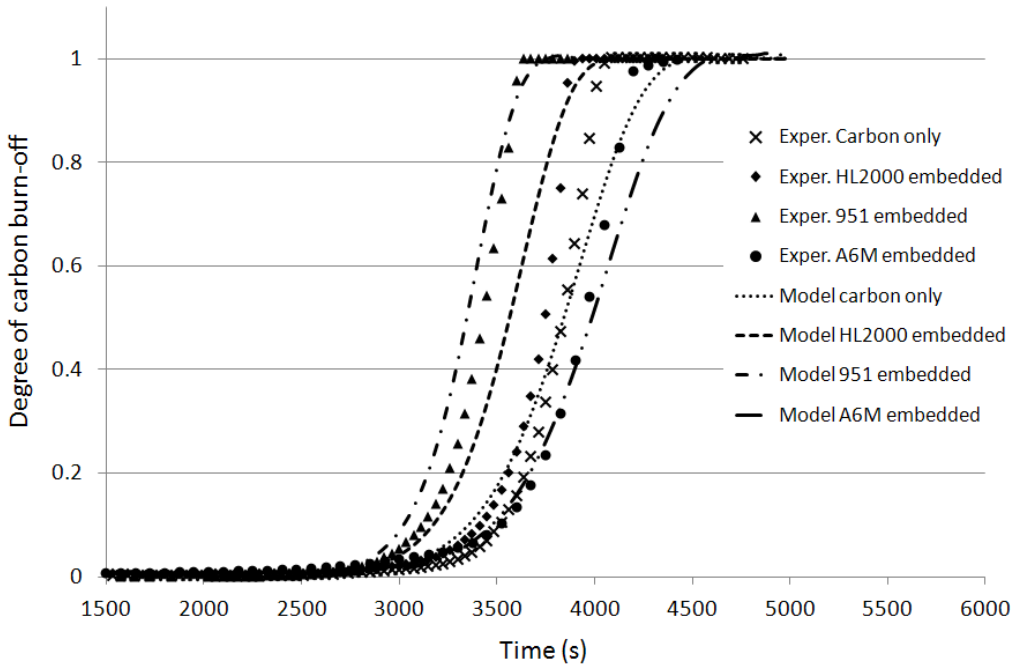

Figure 3-17 Model validation of carbon burn-off at linear heating rate of 10 K/min temperature profile with kinetic parameters obtained from average mass loss rate from HL2000, Dupont 951 & Ferro A6M LTCC.

(ii) Kinetic analysis using isoconversion model

Instead of using the values obtained from the average mass loss rate, the values from the isoconversion first order reaction model were used for HL2000 only (Figure 3-8 & 3-9). Since the measured burn-off rates at the start and end of burn-off were reported to be very unstable [112, 113], thus only the kinetic parameters obtained from burn-off conversion at 0.1 to 0.9 were employed. The large uncertainties in the measured reactivity at both ends of burn-off are mainly due to the devolatisation of polymeric residue from the carbon tape at low conversion and when mass approaches zero at complete burn-off at high conversion. Instead, for conversion values less than 0.1 and greater than 0.9, the same values of kinetic parameters as at 0.1 and 0.9 burn-off respectively were employed as good approximations, see Figure 3-18. The same assumption and modification were applied to the pre-exponential plot used in the subsequent model validation.

These parameters were employed on some complex burn-off profiles such as a long isothermal step as in Figure 3-19 and a multi-step firing profile consisting of multiple isothermal steps as in Figure 3-20. Excellent agreements were obtained with only some deviations. These deviations from the measured burn-off curve for the single isothermal step (Figure 3-19) and multi-step profile (Figure 3-20) are compiled in Table 3-5. The kinetic parameters obtained by the isoconversional first order model could provide a better estimation of carbon burn-off. These deviations are well acceptable for the parameters to be employed in the diffusion and thermal equations for subsequent modelling of carbon burn-off in the LTCC porous media.

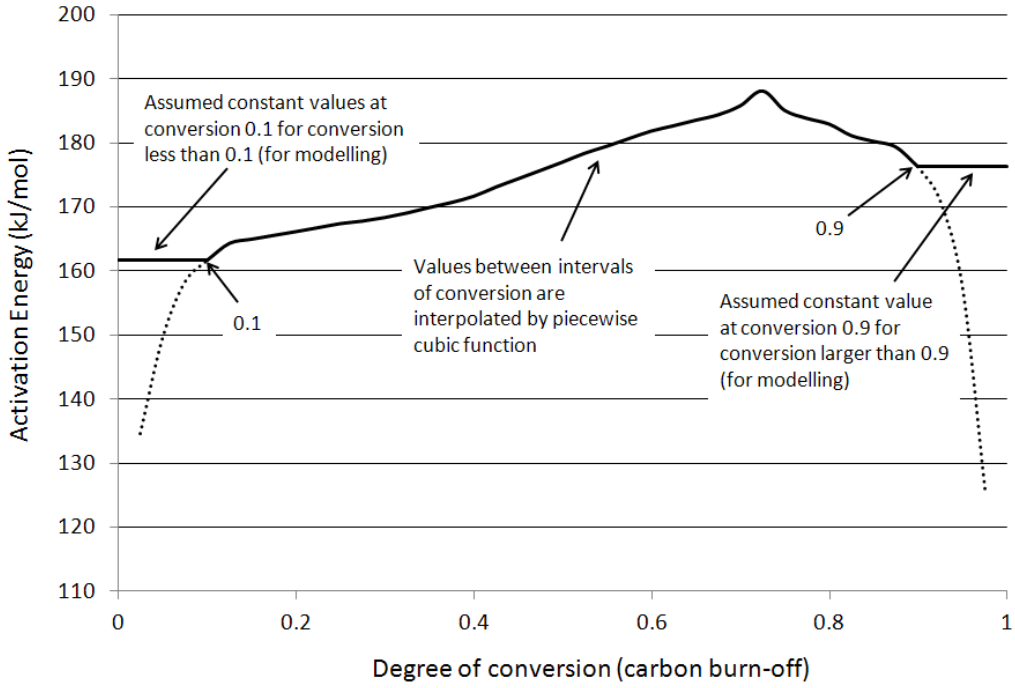

Figure 3-18 Isoconversion variable kinetic activation energy plots used for modelling. Same modification was applied to pre-exponential factors.

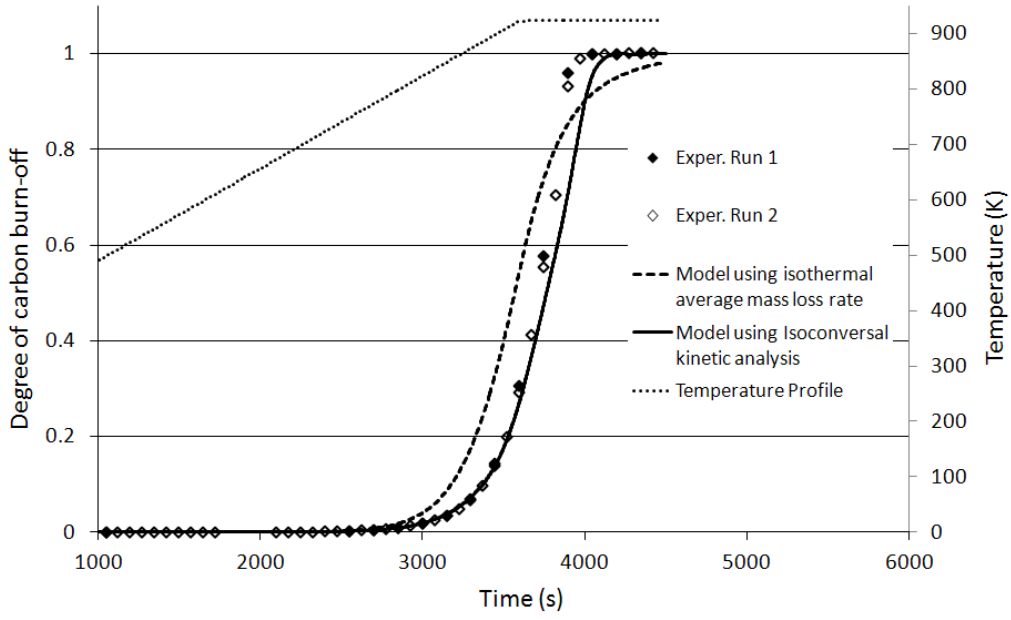

Figure 3-19 Model validations between kinetic parameters obtained from average mass loss and isoconversion variable kinetic parameters at isothermal step of 923 K for 30 min at constant heating rate at 10 K/min on HL2000.

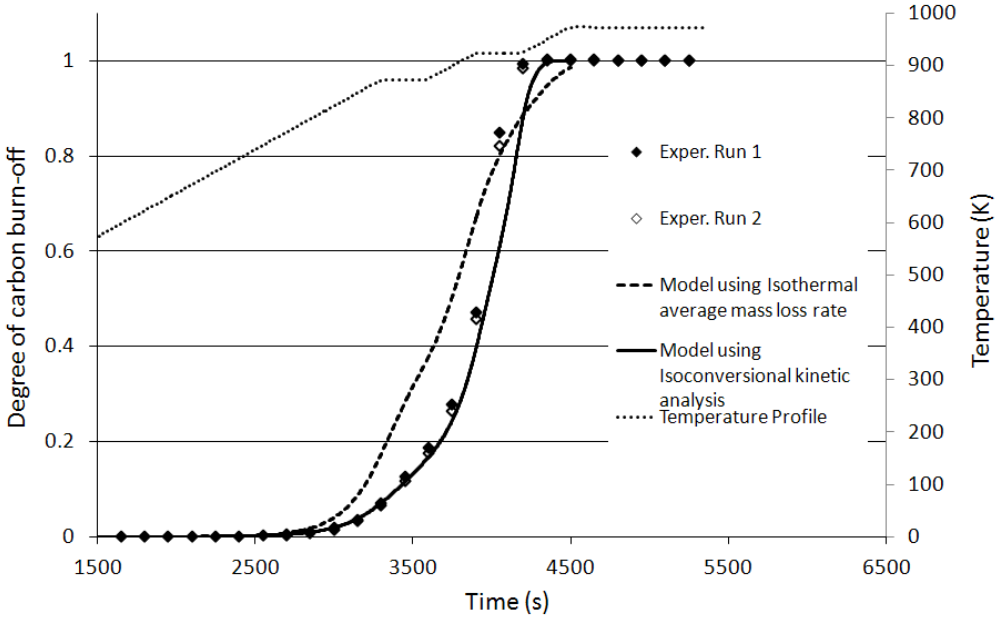

Figure 3-20 Model validations between kinetic parameters obtained from average mass loss and isoconversion variable kinetic parameters at multiple step burn-off profile between 873 – 973 K with constant heating rate of 10 K/min.

Table 3-5 Model validation results between kinetic parameter calculated from average mass loss and isoconversional variable kinetic parameters analyses.

	Time to reach complete carbon conversion (s)		
Temperature Profile	**Measured (average)**	**Average mass loss**	**Isoconversional**
Single isothermal step (Figure 3-19)	3938	4469 (+13.5 %)	4091 (+3.9 %)
Multi-steps (Figure 3-20)	4168	4469 (+7.2 %)	4297 (+3.1 %)

(b) LTCC Sintering Kinetic Model

If the activation energy and pre-exponential factor values obtained from the simple linear regression on the multiple heating rates were substituted back to equation (3.30), the sintering curves at different heating rates could then be predicted by integrating equation (3.30) with respect to t and imposing initial condition of $\alpha_L = 0$, $t = 0$. The deviation of the experimental data with the predicted curves can also provide an

assessment of the accuracy and appropriateness of using a single average value of activation energy and pre-exponential factor.

Equation (3.30) after integrating, becomes

$$\ln(1-\alpha_L) = -\left(4.8\ X\ 10^9 \exp -\frac{253000}{RT}\right) t \qquad (3.34)$$

The sintering curves i.e. α_L predicted with respect to time using equation (3.34) at 1 K/min, 3 K/min, 5 K/min and 10 K/min, are plotted and compared with the experimental results. The comparisons are shown respectively in Figures 3-21 to 3-24. For all cases, the predicted sintering curves fall within the experimental curves. However, trend of having larger deviation particularly at the initial stage of sintering was observed at the heating rates of 5 K/min (Figure 3-23) and 10 K/min (Figure 3-24). Though it is a concern, but for our study and in practical LTCC sintering process, the heating rate hardly exceeds 10 K/min., and that these larger deviations are not excessive, and acceptable. Therefore, it is reasonable to utilize the simple single step first order reaction model for this LTCC sintering process. This analysis also indicates that a single value of activation energy and pre-exponential factor could adequately describe the LTCC sintering process.

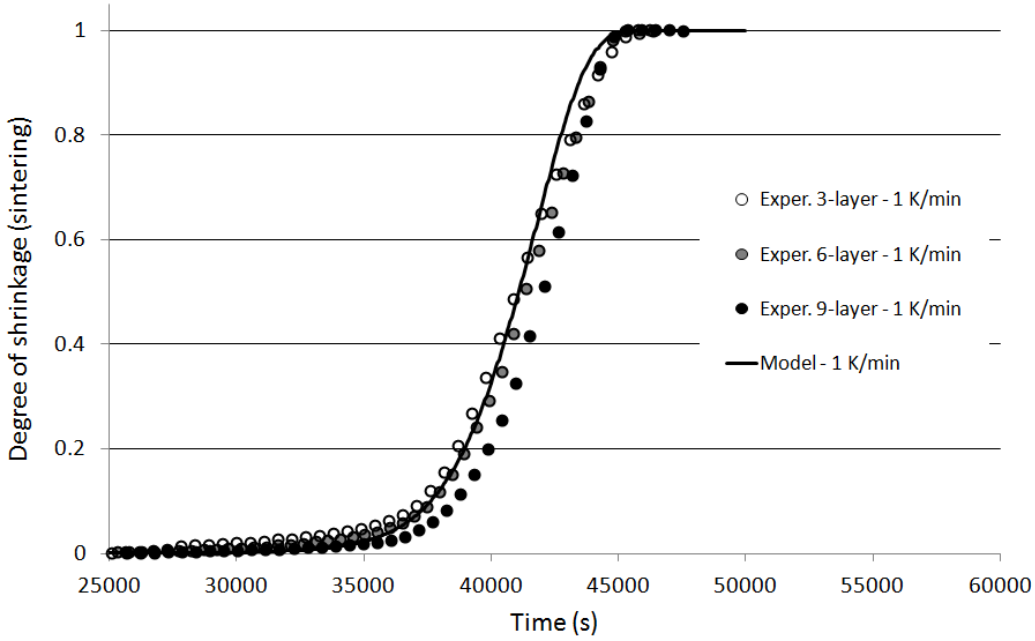

Figure 3-21 Comparison of experimental and predicted TMA curves at 1 K/min constant heating rate.

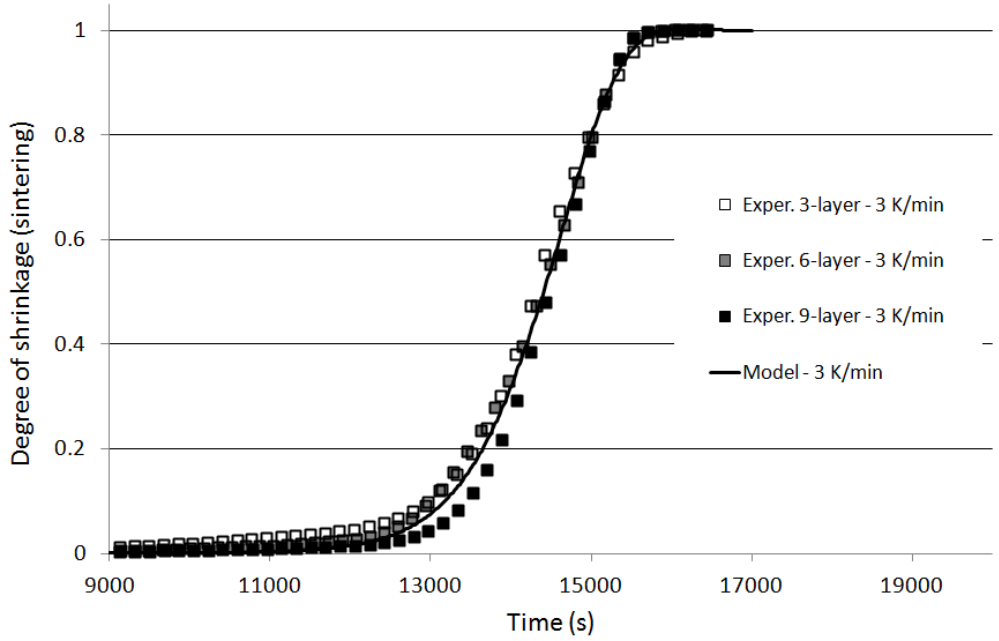

Figure 3-22 Comparison of experimental and predicted TMA curves at 3 K/min constant heating rate.

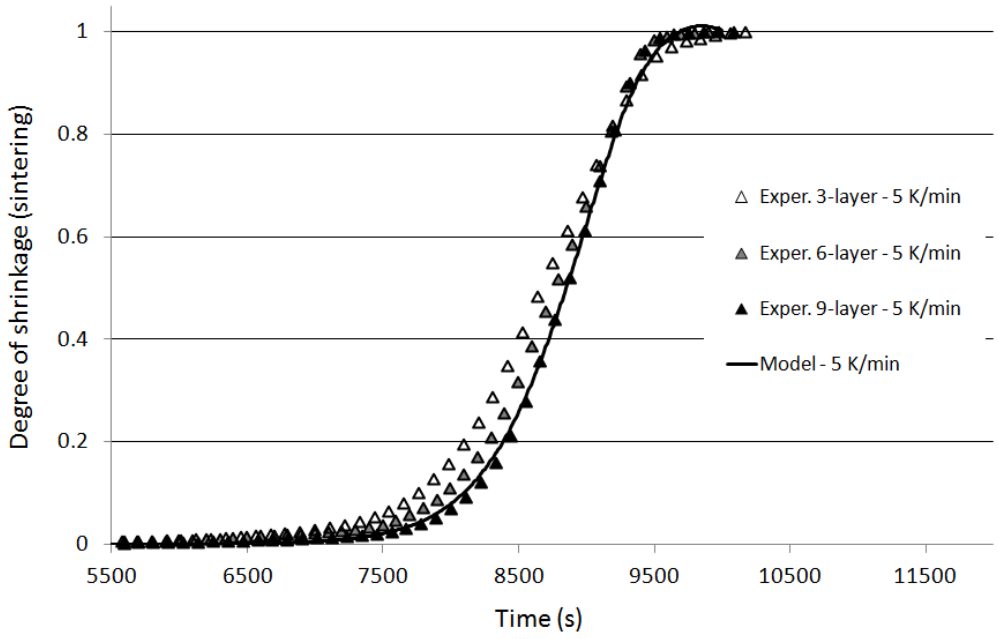

Figure 3-23 Comparison of experimental and predicted TMA curves at 5 K/min constant heating rate.

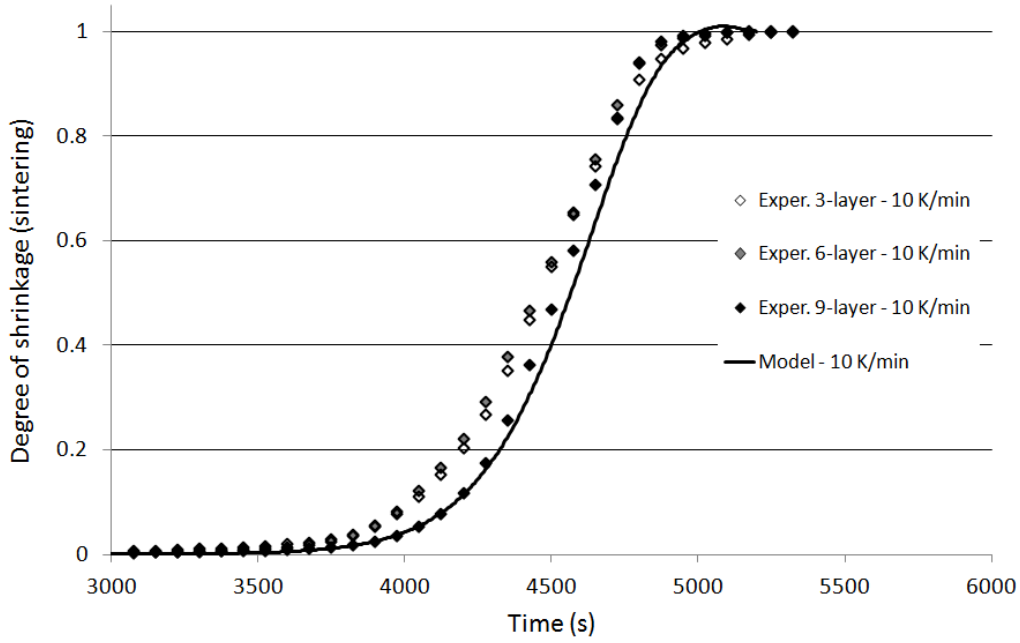

Figure 3-24 Comparison of experimental and predicted TMA curves at 10 K/min constant heating rate.

3.4 Concluding Remarks

LTCC embedded carbon kinetic analysis of catalytic effect induced by the inorganic metal oxides contained in LTCC was shown to be significantly affecting the carbon burn-off rate. Among the tested LTCCs, Dupont 951 is a strong catalyst followed by HL2000, while Ferro A6M inhibits the carbon burn-off. The catalytic or retarded effect of carbon burn-off was revealed by the TGA experiments; it was further confirmed in the kinetic analysis using isothermal TGA with average mass loss rate by comparing carbon tape burn-off with and without LTCC. The Arrhenius plots of embedded carbon with catalytic or retarded burn-off always appear above or below respectively the carbon tape's plots. Kinetic parameters for embedded carbon in LTCC were determined using both isothermal and non-isothermal kinetic analyses. Isoconversion method fitted with a first order reaction model was shown to be a better estimation method for embedded carbon burn-off with the ability to model quite closely the burn-off path.

The kinetic parameters for HL2000 sintering were determined based on first order reaction model for solid state reaction. Simple linear regression over multiple heating rates was used to avoid the ambiguity on the reaction rate parameters resulted from the single non-isothermal analysis. This simple model predicted the sintering curve reasonably well within the experimental range investigated from 1 K/min to 10 K/min. A single value of activation energy and pre-exponential factor could appropriately be used for the sintering of LTCC despite of the complex sintering mechanisms of viscous flow. In addition, this mathematically simple model could be integrated easily into the process model, the subject of investigation in Chapter 4.

Chapter 4

PROCESS MODELING AND SIMULATION OF EMBEDDED CARBON BURN-OFF IN LTCC

For a successful fabrication of embedded structure in a multi-layer LTCC ceramic, other than the structure formation and lamination processes, the most crucial process is the sintering process. The fugitive carbon which is embedded in the multi-layer LTCC has to burn-off while sintering of the ceramics is in progress. The inherent pore elimination during the sintering of LTCC reduces both the reactive gas supply and carbon burn-off escaping paths. For process optimisation of LTCC embedded structure manufacturing using carbon fugitive technique, a realistic model which takes into consideration the effects of mass transport phenomena for both reactive and product gases associated with the chemical reaction of carbon burn-off is necessary. Chemical reaction involves multi-species system of homogeneous gas and heterogeneous solid-gas reactions, and mass transportation system with multi-gas transport through the porous medium have to be considered. The porosity effect of LTCC with the evolution of microstructure during sintering, core shrinkage with severe structure change of carbon particles, concentration gradient of reactive species through the LTCC layer and the deformation of the un-supported LTCC layer over the embedded cavity as a result of the viscous flow of softening glass phase, are some of the major physical phenomena observed and to be considered in the model. The understanding of the process could lead to the optimisation of the fabrication process for improved dimensional stability and defect minimisation in an embedded structure of a multilayer composite ceramic substrate. This could form the foundation for the scaling up of variable sizes of

structures and the understanding of the contributing effects of other structural parameters such as LTCC porosity, and the partial pressure of the oxidising gas.

4.1 Physical Phenomena of Embedded Carbon Burn-off

For embedded structure fabrication of LTCC, especially for fully embedded structure, sacrificial carbon has to be burn-off if it was employed as a sacrificial insert for the system. Sample will undergo debinding at first and subsequently sintering of LTCC. Carbon burn-off will proceed during the course of sintering.

When a multilayer composite ceramic substrate such as LTCC containing embedded structure filled with carbon material is heated, the following events with reference to Figure 4-1 could occur [1,2,64]:

- Decomposition of polymeric binder and additives of the tape system caused by heat or oxidation i.e. debinding.
- Diffusion of mass including reactant (O_2), product (CO, CO_2) and inert (N_2) gases and heat across the boundary layer surrounding the embedded carbon sample.
- Diffusion of mass and heat through the porous structure of LTCC layers.
- Diffusion of mass and heat through the porous structure of carbon layer.
- Heterogeneous reaction of gases (O_2 and CO_2) with carbon within the carbon layer.
- Homogeneous reaction of gases (CO and O_2) within the sample.
- Heat generation or consumption by the carbon-gases chemical reactions.
- Sintering of LTCC by liquid phase viscous flow.
- Progressive pore elimination of the LTCC layers due to glass-phase sintering.

In addition, some physical structure changes may be expected:

- Progressive volume shrinkage of the embedded structure due to the densification of LTCC.
- Progressive deformation (sagging) of the LTCC layers over the unsupported embedded structure due to glass-phase softening.

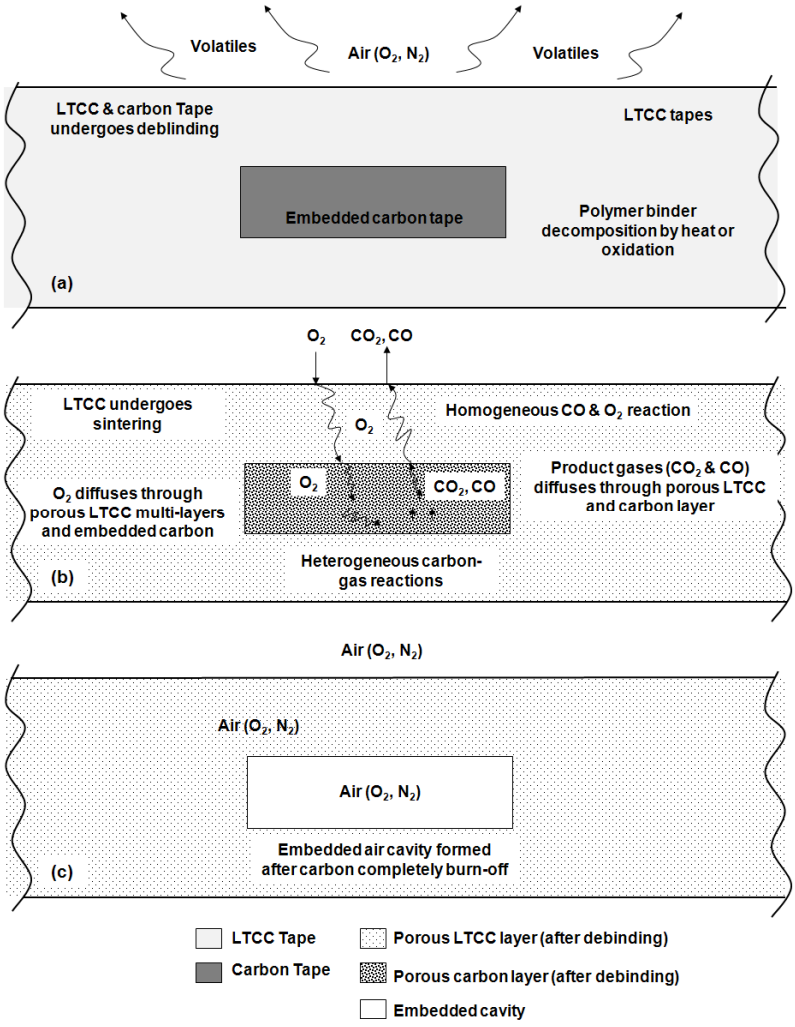

Figure 4-1 Phenomenological interpretation of embedded carbon burn-off process for embedded cavity in multi-layer LTCC during the sintering process. a) Debinding of LTCC embedded carbon, b) instant of LTCC sintering and carbon burn-off with diffusion of both reactant and product gases, c) complete sintering and burn-off.

4.2 Theoretical Model

The process of embedded structure using carbon burn-off is indeed complicated. The effect of green compact (lamination), mass diffusion of reacting and product species, gaseous reactions of the species, products of the carbon burn-off of complete or incomplete burn-off, etc all have an effect on the final embedded structures. However, by at large the key parameters are associated with mass transport with combined effect of reaction processes from both the LTCC sintering and carbon burn-off. The phenomenological model of carbon burn-off in embedded LTCC is described in detail in Section 4.1 with a schematic diagram shown in Figure 4-1. The two major process mechanisms are indeed the carbon burn-off and LTCC sintering. They are all kinetically connected and could be considered as chemical reaction processes where kinetic parameters are important. TGA and TMA, employed in the current investigation, as described in Chapter 3, are well known techniques for determining experimentally the kinetic parameters. TGA & TMA methodologies provide "overall" apparent kinetic parameters of the thermal activated process without having to delve into the reaction steps. The model though is simple, but the mass transport equations coupling with various mass transport parameters such as porosity evolution during sintering, multi gas species diffusion, energy balance of chemical and heat reaction, make it comprehensive enough to produce comparable and validated results.

Based on the physical phenomena depicted in Figure 4-1, a non-isothermal time dependent multi-component mass transfer system was proposed. The mass transfer model consisted of a set of species mass balance equations coupling with carbon burn-off, together with a LTCC sintering model. Energy balance equation was employed for the non-isothermal behaviour of LTCC firing profile and the exothermic reaction of

carbon burn-off. The possibility of a higher burn-off temperature than the firing temperature is thus considered. Due to the net transfer of carbon, Darcy equation was utilised for the possible internal pressure build-up of carbon burn-off.

This study focuses on the process modelling of the embedded carbon burn-off. As such, polymeric vaporization or related debinding phenomena were not modelled. The modelling assumes that the sample has fully debinded prior to the commencement of sintering and that the debinding process has no significant effect on carbon burn-off. To simplify the model without a loss of generality, volume shrinkages of cavity and LTCC during sintering were not considered although there will be about 10 – 30 % of linear shrinkage during sintering. This exclusion will not cause significant inaccuracy as this dimensional changes will only have an effects on the escape path of the gases and the reaction volume of carbon burn-off, which are only second order effects.

4.2.1 Mass Conservation of Species

The general mass continuity for species *i* for a chemically reacting multicomponent gas system in mass units could be expressed as [98, 123],

$$\frac{\partial(\varepsilon\rho_i)}{\partial t} + \nabla \cdot n_i = R_i \qquad (4.1)$$

Where ε is the porosity of the porous medium, ρ_i and R_i are mass concentration of species and mass rate of generation due to chemical reaction respectively of species *i,* n_i is the total mass flux.

Equation (4.1) is applicable for a medium with continuous properties. However, for LTCC, its carbon layers are porous after debinding. Thus, the variables have to be interpreted as average quantities over the smallest volume surrounding the point in interest which is considered sufficiently large for macroscopic continuum properties for a porous medium. The volume should contain many pores and solid matrix elements. As the pore sizes are small for a computational element size, this assumption is satisfied.

The source term, R_i represents the net formation rate of species *i*, per unit volume by a homogeneous chemical reaction. It is different from the heterogeneous reaction that is normally perceived for a carbon burn-off process, i.e. the reaction occurs at the carbon-gas interface, particularly for a single particle analysis. However, in this analysis, carbon tape was used and modelled. It is a layer cast with uniformly distributed fine carbon particles (< 1 μm) and is highly porous (porosity = 0.55) after debinding. As such, as burn-off proceeds at a relatively low temperature (< 1123 K), reaction takes place not just at the surface but also at the pore walls throughout the carbon layer. The reactant concentration gradient is expected to be low. Under these circumstances, the reaction may be well approximated as homogeneous [124,125]. Furthermore, accurate determination of the reacting surface area for a heterogeneous reaction is difficult even though there exists mathematical model for the computation of pore surface area based on the initial structure parameters [45].

The total mass flux n_i relative to fixed coordinates, includes both diffusive and convective flux attributed to bulk flow [126] may be written as,

$$n_i = \rho_i v_i \tag{4.2}$$

Where v_i is the species velocity.

The introduction of a reference velocity, i.e. mass average velocity, v, is a convenient tool. It is necessary especially when the diffusion equation is to be coupled with the momentum and energy equations where the linear mass momentum is always expressed in mass average velocity. The relationship between the velocities and mass flux can be written as,

$$n_i = \rho_i (v_i - v + v) \tag{4.3}$$

$$n_i = \rho_i v + \rho_i (v_i - v) \tag{4.4}$$

where $\rho_i (v_i - v)$ is a diffusion flux relative to the mass average velocity. Using Fick's effective diffusivity or pseudobinary approach for the multicomponent system [99], this diffusion flux j_i may be expressed as,

$$j_i = \rho_i (v_i - v) = -\rho_g D_i^e \nabla w_i \tag{4.5}$$

Where ρ_g is the density of mixture or total gas phase, D_i^e is the effective diffusivity for multicomponent diffusion, and w_i is the mass fraction of species, *i.*

Substitute equations (4.4) & (4.5) into (4.1),

$$\frac{\partial(\varepsilon\rho_i)}{\partial t} + \nabla\cdot(\rho_i v) = \left(\nabla\cdot\rho_g D_i^e \nabla w_i\right) + R_i \tag{4.6}$$

For the terms on the left hand side of equation (4.6), by expanding the differential operators by the appropriate differential relation and noting that $\rho_i = \rho_g w_i$,

$$\frac{\partial(\varepsilon\rho_i)}{\partial t} + \nabla\cdot(\rho_i v) = \frac{\partial(\varepsilon\rho_i)}{\partial t} + (\nabla\rho_i\cdot v) + \rho_i(\nabla\cdot v)$$

$$= \frac{\partial(\varepsilon\rho_g w_i)}{\partial t} + \left(\nabla\rho_g w_i\cdot v\right) + \rho_g w_i(\nabla\cdot v)$$

$$= \frac{\varepsilon\rho_g\partial(w_i)}{\partial t} + \frac{w_i\partial(\varepsilon\rho_g)}{\partial t} + \left(\rho_g\nabla w_i\cdot v\right) + \left(w_i\nabla\rho_g\cdot v\right) + \rho_g w_i(\nabla\cdot v) \tag{4.7}$$

With the following expanded mass continuity equation for the total gas phase,

$$\frac{\partial(\varepsilon\rho_g)}{\partial t} = -\rho_g(\nabla\cdot v) - \left(\nabla\rho_g\cdot v\right) + R_T \tag{4.8}$$

where the total mass rate of generation of all species is,

$$R_T = \sum_i^N R_i \tag{4.9}$$

Equation (4.7) becomes,

$$\frac{\partial(\varepsilon\rho_i)}{\partial t} + \nabla \cdot (\rho_i v)$$

$$= \frac{\varepsilon\rho_g \partial(w_i)}{\partial t} + \left(\rho_g \nabla w_i \cdot v\right) + w_i R_T = \rho_g \left(\frac{\varepsilon\partial(w_i)}{\partial t} + v \cdot \nabla w_i\right) + w_i R_T \quad (4.10)$$

Finally, equation (4.10) replaces the left right side of equation (4.6),

$$\rho_g \left(\frac{\varepsilon\partial(w_i)}{\partial t} + v \cdot \nabla w_i\right) + w_i R_T = \left(\nabla \cdot \rho_g D_i^e \nabla w_i\right) + R_i \quad (4.11)$$

Rearranging equation (4.11),

$$\rho_g \left(\frac{\varepsilon\partial(w_i)}{\partial t} + v \cdot \nabla w_i\right) = \left(\nabla \cdot \rho_g D_i^e \nabla w_i\right) + (R_i - w_i R_T) \quad (4.12)$$

Equation (4.12) is the equivalent form of species mass conservation equation expressed fully in mass fraction with reaction term due to the net transfer of carbon. Using mass fraction as the driving force for mass diffusion is convenient as it will not vary with temperature and composition particularly in non-isothermal condition which is common in practice [99].

4.2.2 Mass Balance of Carbon

The rate of conversion of carbon burn-off derived from the kinetic analysis of carbon burn-off in Chapter 3 was utilized. The mass balance was expressed in term of O_2 concentration and mass of carbon as,

$$\frac{d\alpha_c}{dt} = ak_c^* \rho_g w_{O_2}(1-\alpha_c) \quad (4.13)$$

where,

$$k_c^* = A_c^* exp^{-\frac{E_C}{RT}} \quad (4.14)$$

The kinetic parameters determined experimentally by TGA kinetic analysis were employed for modelling.

4.2.3 Momentum Equation

By considering bulk flow only due to internal pressure build-up by carbon burn-off reaction, the bulk flow velocity or Darcy velocity could be estimated by Darcy equation if laminar flow is expected,

$$v = -\frac{\kappa}{\mu}\nabla p_g + \rho_g g \quad (4.15)$$

Together with the total gas phase mass continuity equation and neglecting gravity effect from the gas phase, a mathematical model for the porous media flow with pressure gradient as the major driving force may be written [98, 127],

$$\frac{\partial(\varepsilon\rho_g)}{\partial t} = \left(\nabla \cdot \rho_g \frac{\kappa}{\mu}\nabla p_g\right) + R_T \quad (4.16)$$

where μ is the dynamics viscosity of the fluid medium passing through the porous medium. κ is the gas permeability of the solid and could be estimated by Poiseuille

flow relationship [128]. By assuming the same permeability for all the gas species and cylindrical pore, the gas permeability κ may be written as,

$$\kappa = \frac{\varepsilon d^2}{32} \tag{4.17}$$

Where *d* is the diameter of the solid pore size.

4.2.4 Energy Balance Equation

In addition to the mass continuity equations, the energy equation taking into consideration the possible heat reaction affecting the reaction temperatures especially for the exothermic reaction process has to be included. Transient heat transfer equation applied to a solid will be used but with effective thermal properties (C_p^e and k_e) considered for the porous media as an equivalent mixture of solid and gases.

By neglecting the effect due to radiation, and any mechanical energy heat source, heat balance equation including heat generation due to the chemical reaction of carbon burn-off may be written as,

$$C_p^e \frac{\partial T}{\partial t} + \nabla \cdot (-k_e \nabla T) = Q - C_p^e v \cdot \nabla T \tag{4.18}$$

and

$$Q = \Delta H_r(R_v) \tag{4.19}$$

Where C_p^e and k_e are the effective heat capacity and effective thermal conductivity respectively of the porous medium, ΔH_r and R_v are respectively the heat of reaction and the reaction mass rate of the chemical reaction.

4.2.5 Carbon Reaction Rate Model

Four chemical reactions could occur during carbon burnout in an air environment [129]:

Heterogeneous reaction: $C + O_2 \rightarrow CO_2$ (I)

Heterogeneous reaction: $2C + O_2 \rightarrow 2CO$ (II)

Heterogeneous reaction: $C + CO_2 \rightarrow 2CO$ (III)

Homogeneous reaction: $2CO + O_2 \rightarrow 2CO_2$ (IV)

However, a simple irreversible chemical equation to represent the main carbon burn-off process as described in Chapter 3 on the kinetic parameters of carbon burn-off would be sufficient to capture the overall effect and is adopted here. Thus, the overall reactions will be described by a combined reaction consisting of reactions (I) and (II),

$$aC + b0_2 \overset{R_v}{\rightarrow} cCO + dCO_2 \quad (4.20)$$

The possible gasification of carbon by CO_2 has a reaction rate far slower than the reaction by O_2 [55] and thus it was neglected. In addition, the possible homogeneous CO and O_2 reaction within the porous media is expected to be small as the applied sintering temperature was not high. As a whole, a homogenous reaction can be assumed as the reaction was taking place at a relatively low temperature with a low

ramp rate. The reaction regime was near chemical reactivity controlled and the effect of heterogeneity at the carbon surface was not significant.

Using the same approach as the carbon burn-off kinetic analysis in Chapter 3, the product ratio of CO/CO_2 is factored in for mass balancing at various temperatures. The stoichiometric coefficients are defined in term of CO/CO_2 product ratio [103,104,130] as,

$$a = \frac{2\eta+2}{\eta+2}, b = 1, c = \frac{2\eta}{\eta+2}, d = \frac{2}{\eta+2} \quad (4.21)$$

and

$$\frac{CO}{CO_2} = \eta = \left[A\ exp^{(3070/T)}\right]^{-1} \quad (4.22)$$

where $A = 0.02\left(\frac{P_{O_2}}{1x10^5}\right)^{0.21}$ (4.23)

First order reaction model was used for the burn-off reaction as it is a simple and widely used model with sufficient accuracy. It is a practical model for complex multi-components coupling system where coupling with diffusion and convection together with heat transfer equations are required. Carbon burn-off with a net transfer of solid carbon is most conveniently expressed in mass unit. The reaction rate in mass concentration was formulated with respect to mass fraction instead of the usual molar concentration. As such, the reaction rate based on the concentration of O_2 may be written as,

$$R_C = -ak_c\rho_g w_{O_2} \quad (4.24)$$

$$R_{O_2} = -k_c\rho_g w_{O_2} \quad (4.25)$$

$$R_{CO} = ck_c\rho_g w_{O_2} \quad (4.26)$$

$$R_{CO_2} = dk_c\rho_g w_{O_2} \quad (4.27)$$

where k_c is the reaction rate constant which was defined previously in Chapter 3. It could be determined experimentally from the TGA kinetic analysis

4.2.6 LTCC Sintering Rate Model

As the carbon was embedded as a structure in LTCC, the carbon burn-off will be greatly affected by the sintering of the LTCC. Sintering causes pore closure of LTCC and in turn increases the mass transport resistance for both reactants and products. Thus a relevant sintering model which could reasonably represent the LTCC sintering is necessary. The sintering kinetic of LTCC could be expressed as a pseudo solid state reaction. The reaction model function may be considered as a solid-state first order reaction, relating to the normalised fraction of linear shrinkage, α_L as,

$$\frac{d\alpha_L}{dt} = k_L(1 - \alpha_L) \quad (4.28)$$

where k_L is the rate function which is commonly referred as the Arrhenius rate equation, and could be written as:

$$k_L = A_L \, exp\left(-\frac{E_L}{RT}\right) \tag{4.29}$$

where A_L is the pre-exponential factor, E_L is the activation energy, and R is the universal gas constant.

The kinetic parameters of LTCC were determined experimental by TMA kinetic analysis as described in Chapter 4.

4.2.7 Other Constitutive Equations

There are other relationships involved in the formulation and useful in solving the multi-component diffusion problem. These relationships are provided in this section.

(i) Total gas phase density may be written as a function of temperature and pressure,

$$\rho_g = \frac{p_g(M_g)}{RT} \tag{4.30}$$

Where p_g is the total gas pressure in the system, and M_g is the molecular weight of the gas mixture.

(ii) Summation of mass fraction for all gases:

$$\sum_{i=1}^{n} w_i = 1 \tag{4.31}$$

(iii) Molar fraction of species:

$$x_i = \frac{w_i M_g}{M_i} \tag{4.32}$$

Where M_i is the molecular weight of gas species *i*

(iv) Summation of molar fraction for all gases:

$$\sum_{i=1}^{n} x_i = 1 \tag{4.33}$$

(v) Ideal gas equation of state for partial gas pressure of species:

$$p_i = x_i p_g \tag{4.34}$$

4.3 Transport Coefficients and Material Properties Estimation

4.3.1 Effective Diffusion Coefficients (D_i^e)

By assuming that diffusion takes place in the transition regime of molecular and Knudsen diffusion, the molecular-wall interaction and molecular-molecular interaction are both important. Thus, gas diffusivity could be expressed by the Bosanquet formula [132] as,

$$D_i^e = \frac{1}{\left(\frac{1}{D_{i\,m}^e} + \frac{1}{D_{i\,k}^e}\right)} \tag{4.35}$$

where $D_{i\,m}^{e}$ and $D_{i\,k}^{e}$ represent the effective diffusivity of species due to molecular and Knudsen diffusion respectively.

4.3.2 Effective Molecular Diffusion Coefficients ($D_{i\,m}^{e}$)

For simple gas molecules, such as O_2, CO, CO_2 and N_2, the ordinary binary diffusivity could be predicted by Fuller's equation [132, 133] based on hard sphere model and the principle of additive atomic diffusion volume as,

$$D_{i,j} = (3.2034e^{-8})\left(\frac{T^{1.75}}{p_g*\left(\vartheta_i^{\frac{1}{3}}+\vartheta_j^{\frac{1}{3}}\right)^2}\right)\left(\frac{1}{M_i}+\frac{1}{M_j}\right)^{0.5} \tag{4.36}$$

For flow in the porous medium, the ordinary binary diffusivity has to be modified to reflect the effect of flow due to the tortuous path of the porous medium. One of the simple relations to relate the structure parameters of porosity (ε) and tortuosity (τ) for the porous medium is,

$$D_{i,j}^{e} = \frac{\varepsilon}{\tau} D_{i,j} \tag{4.37}$$

Since multispecies are involved in the process modelling, the binary diffusivity could be extended to estimate the equivalent binary diffusivity by appropriate averaging the interaction of the various species in the multicomponent gas mixture [99,87,100]. It can be expressed as,

$$D_{i\,m}^{e} = \frac{(1-x_i)}{\sum_{j=1,j\neq i}^{n}\frac{x_j}{D_{i,j}^{e}}} \tag{4.38}$$

Equation (4.38) is thus the effective molecular diffusion coefficients to be used in equation (4.35).

4.3.3 Effective Knudsen Diffusion Coefficients ($D_{i\,k}^{e}$)

For Knudsen flow in a porous medium, diffusivity based on gas kinetic theory after considering the porous medium can be expressed as [35],

$$D_{i\,k}^{e} = \left(\frac{4}{3}\right) * kn0 * \left(\frac{8RT}{\pi M_i}\right)^{0.5} \tag{4.39}$$

where *kn0* is a characteristic parameter of the solid depending largely on pore geometry.

For a solid composed of uniform spherical grain, such as the carbon tape employed for this investigation, it is more realistically modelled as an aggregate of spherical particles. The characteristic parameter could be expressed as [35],

$$kn0 = \frac{1}{\left(\left(\frac{128}{9}\right)\left(n_d * \frac{\tau}{\varepsilon}\right)\left(r_g^2\right)\left(1+\frac{\pi}{8}\right)\right)} \tag{4.40}$$

and the number of solid grains per unit volume of porous solid n_d can be calculated,

$$n_d = \frac{3(1-\varepsilon)}{4\pi r_g^3} \tag{4.41}$$

The grain size, r_g, could be estimated physically by various techniques such as light scattering.

While for LTCC, it will be more appropriate to assume long cylindrical pore of uniform pore diameter, d_L, the Knudsen characteristic parameter may be expressed as,

$$kn0 = \frac{\varepsilon}{\tau}\left(\frac{d_L}{4}\right) \tag{4.42}$$

The pore size could be measured and estimated by mercury porosimeter.

For tortuosity, without the need for diffusivity measurement, an expression derived from mercury porosimetry for any pore size distribution with a simple cylindrical pore with pore shape factor close to unity was employed [130, 134],

$$\tau = 2.23 - 1.13\varepsilon \tag{4.43}$$

4.3.4 LTCC Porosity

Pore elimination for conventional heat treated sintering is complex. There is added complexity in LTCC sintering due to its liquid phase viscous flow sintering coupling with reactive sintering. The estimation of the porosity changes with respect to LTCC sintering is important as it will greatly affect the diffusion paths of reactants and products through the LTCC layer during carbon burn-off. There are possible kinetic competing effects of LTCC sintering on the carbon burn-off as the pore close-up and reducing the diffusion of reacting gas to the external environment. In-situ measurement of porosity of LTCC during high temperature sintering is difficult. As such, a physical model based on a combined TGA and TMA analyses were derived.

All the estimations were obtained based on data of the TGA and TMA curves obtained at a constant heating rate of 20 K/min for a 12-layer LTCC with 0.15 mm embedded carbon TGA sample and a 9-layer LTCC TMA sample. Based on the observation of TGA analysis, burn-off terminated at about 87% of total expected burn-off (Figure 4-2). This could be taken as the instance of pore closure preventing complete carbon burn-off. The porosity should reduce to zero for the burn-off to terminate prematurely i.e. the supply of reactant was shut off. With the TMA curve running at the same conditions as the TGA, the instant of pore closure corresponds to about 35% of the expected total linear shrinkage (Figure 4-2). This is an interesting phenomenon showing early pore closure well ahead of full shrinkage that deviates from the usual postulation of the conventional solid state sintering. The wetted interfaces between particles may block the paths of the gaseous reactant while allowing further shrinkage. It may only happen where liquid phase sintering of viscous flow is involved.

With this unique phenomenon and complex mechanism, an observation based porosity model was derived for the LTCC sintering as in Figure 4-3. An instant reduction of porosity was assumed at the initiation phase of sintering due to instant pore filling initiated by glass flow promoted by wetting additives commonly present in most of the LTCC system. This is a reasonable assumption due to the usual high content (>30 % wt.) of glass component in LTCC system. As such, instant pore elimination even before the shrinkage of system has stabilized [2] will be expected. Subsequently, it was followed by slow and gradual pore elimination and finally reached pore closure (near zero porosity) at about 35% of the total shrinkage. Shrinkage continued until full sintering was reached.

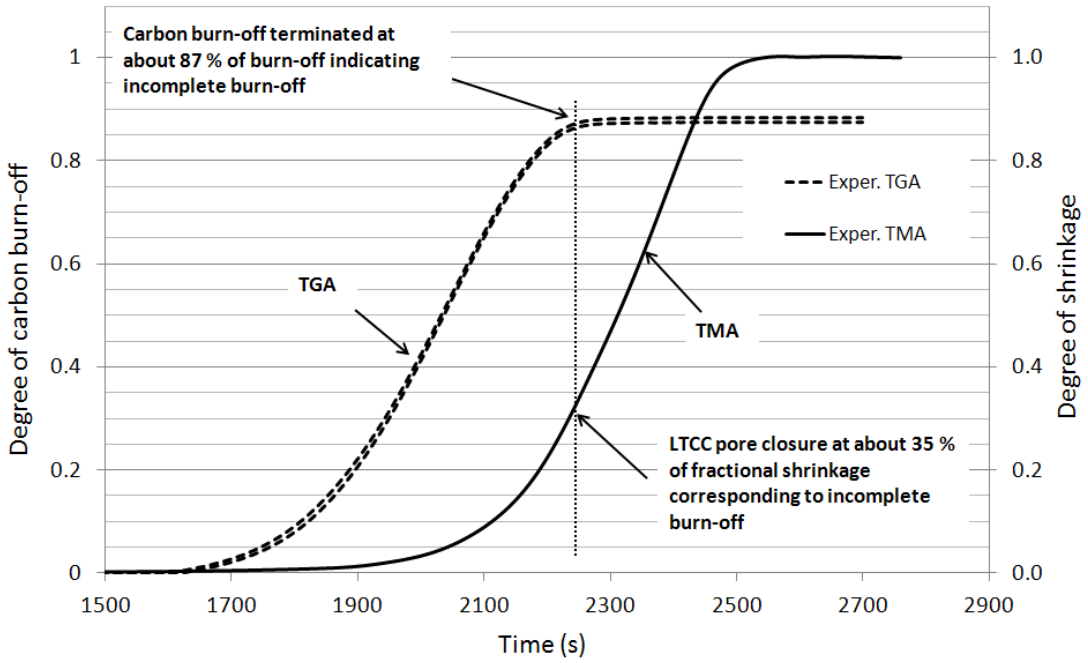

Figure 4-2 Combined TGA and TMA curves for determination of pore closure point at constant heating rate of 20 K/min.

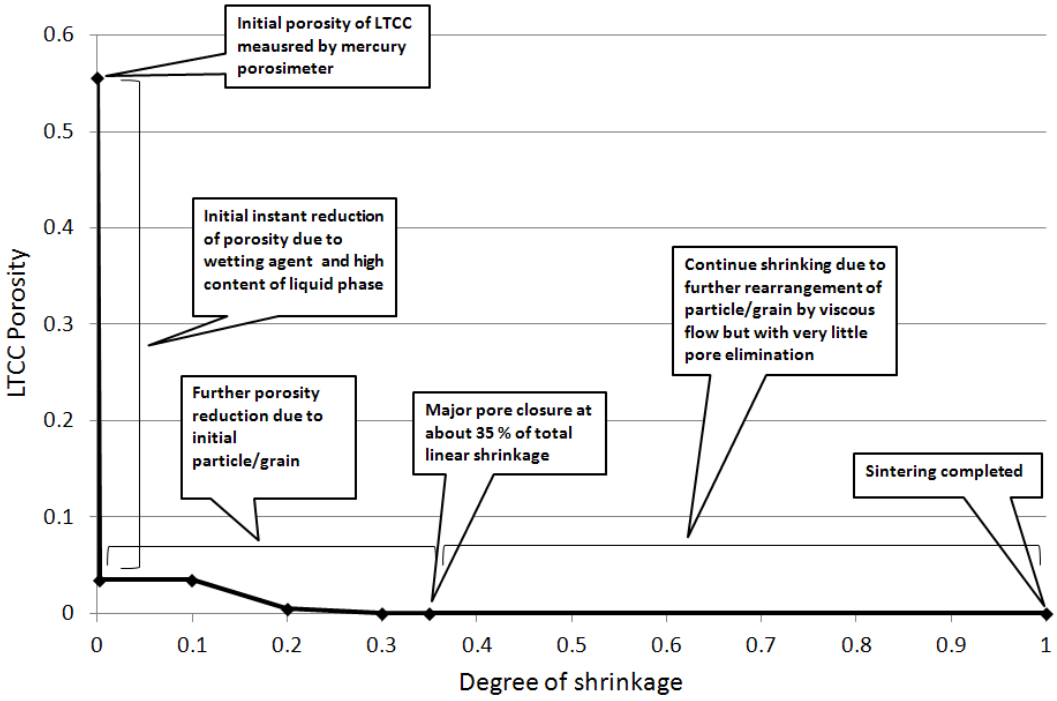

Figure 4-3 Porosity model with respect to degree of LTCC shrinkage.

4.3.5 Effective Thermal Properties, (C_p^e, k_e)

The heat capacity for gas permeated porous solid matrix is normally expressed as an effective heat capacity contributed both from the volume fraction of solid and gases and is expressed as [103,131].

$$C_p^e = (1-\varepsilon)\rho_s C_{ps} + \varepsilon \sum_{i=1}^{N} C_i C_{pi} \quad (4.45)$$

Where ρ_s and C_{ps} are respectively the bulk density and heat capacity of the solid phase, C_i and C_{pi} are respectively the molar concentration and heat capacity of gas species, *i*.

The effective thermal conductivity for an equivalent solid could be expressed as [131],

$$k_e = (1-\varepsilon)^2 k_s + \varepsilon^2 k_g \quad (4.46)$$

Where $k_s$is the thermal conductivity of the solid phase, and $k_g$is the thermal conductivity of the gas mixture.

Method of estimating the thermal conductivity of a gas mixture is analogous to the method of determining the viscosity of a gas mixture [98,100]. The following semi-empirical equations were adopted in this investigation, which are appropriate and satisfactory for non-polar gases at low density [87].

$$k_g = \sum_{i=1}^{N} \frac{x_i k_i}{\sum_{j=1}^{N} x_j \Phi_{i,j}} \quad (4.47)$$

where:

$$\Phi_{i,j} = \frac{\left[1+\left(\frac{\mu_i}{\mu_j}\right)^{\frac{1}{2}}\left(\frac{M_j}{M_i}\right)^{\frac{1}{4}}\right]^2}{\left[8\left(1+\frac{M_i}{M_j}\right)\right]^{\frac{1}{2}}} \quad (4.48)$$

Where $k_i$is the thermal conductivity of gas species i, x_i, x_j respectively are the molar fraction of species i and j, M_i, M_j are respectively the molecular weight of gas species i and j, and μ_i, μ_j respectively are the viscosity of gas species i and j.

The required individual viscosity, heat capacity and thermal conductivity of gas species could be obtained from the temperature dependency relationship from DIPPR®801 Database [136].

For carbon, the equivalent temperature dependent heat capacity relationship of graphite from Perry's handbook was employed. The thermal conductivity was obtained from published value for the synthetic chars using photophoretic force [137].

4.3.6 Heat of Reaction, (ΔH_r)

Heat of reaction could be important when a large amount of heat is released or absorbed during the reaction. Carbon oxidation is a temperature dependent process; the rate of reaction, the products produced and the mechanics of reaction change with the reacting temperature; in some cases significant heat could be liberated. Thus, to include the heat of reaction in the proposed model, the heat of reaction at the reacting temperature has to be formulated.

Considering an open system with minimal flow, the change of enthalpy at constant pressure is applicable and the kinetic energies could be neglected. The reaction map for the reaction equations is shown in Figure 4-4. By applying the law of thermodynamics, an enthalpy balance equation, namely the sum of enthalpy changes at the cooling of reactants (ΔH_1), heating of products (ΔH_3), and the heat of formation (ΔH_2), at the reaction temperature T may be written as,

$$\Delta H_r = \Delta H_1 + \Delta H_2 + \Delta H_3 \tag{4.49}$$

with the specific heats:

$$\Delta H_1 = \left(a_0 C_{p\_c\_0} T_0 - a_T C_{p\_c\_T} T\right) + \left(b_0 C_{p\_O_2\_0} T_0 - b_T C_{p\_O_2\_T} T\right) \tag{4.50}$$

$$\Delta H_2 = \left(c_0 H_{f\_CO\_0} + d_0 H_{f\_CO_2\_0}\right) - \left(a_{0f} H_{f\_c\_0} + b_0 H_{f\_O_2\_0}\right) \tag{4.51}$$

$$\Delta H_3 = \left(c_T C_{p\_CO\_T} T - c_0 C_{p\_CO\_0} T_0\right) + \left(d_T C_{p\_CO_2\_T} T - d_0 C_{p\_CO_2\_0} T_0\right) \tag{4.52}$$

Where a_0, b_0, c_0, d_0 are the stoichiometric coefficients related to the chemical reactions at the reference conditions, a_T, b_T, c_T, d_T are the stoichiometric coefficients related to the chemical reaction at the reacting conditions, $H_{f\_i\_0}$ are the heat of formation of reactants or products i at reference conditions, $C_{p\_i\_0}$ are the molar specific heats of reactant or product i at reference conditions, and $C_{p\_i\_T}$ are the molar specific heats of reactants or products i at reacting conditions.

Since the heat of formation are available for most of the compounds only at standard conditions i.e. 25°C and 1 atm, reaction map is utilised to determine the standard heat of formation at the reacting conditions of interest from the standard condition. The heat of formation (enthalpy of formations) at standard conditions are available at a number of handbooks such as DIPPR® database sponsored by AIChE. The formulation of heat of reaction as shown in Figure 4-4 could be found in most of the chemical engineering text books [105,138].

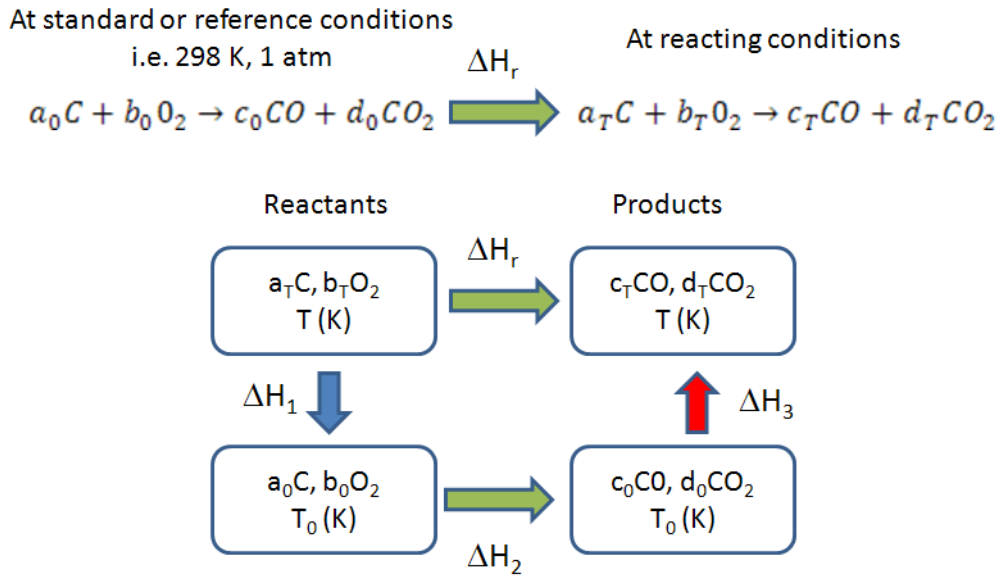

Figure 4-4 Reaction map of carbon oxidation utilised for current investigations.

4.4 Model Validations

For validation, the formulated governing equations of mass transfer for multicomponent system on embedded carbon LTCC structure were applied to a simple embedded carbon disc structure in LTCC of HL2000 system. It can be represented by an axisymmetric 2D model. Various configurations of this LTCC embedded structure in different combination of LTCC layers (2-layer, 6-layer and 12-layer configurations) and carbon thickness (0.05 mm, 0.15 mm and 0.25 mm) were modelled both

numerically and experimentally. A typical 0.15 mm thick carbon tape embedded within a 6-layer LTCC structure with sample dimensions indicated is shown in Figure 4-5. Axisymmetric modelling is sufficient as uniform and axisymmetric heating was applied from the surrounding; thus axisymmetric (i.e. in the θ direction) carbon burn-off will be expected. This allows much simplification in modelling.

The fabrication of the disc sample is relatively easy and it had the same dimensions as the TGA sample used in the carbon burn-off kinetic analysis. As such, the validation of the model could be carried out using the same TGA setup. The TGA experiment allows not only the capturing of the carbon burn-off behaviour, but at the same time the obtained results could be co-related to other variables such as internal pressure built-up, the effect of LTCC thickness and the carbon thickness. The effect of including the bulk flow driven by the pressure gradient produced by a non-equimolar chemical reaction could potentially be assessed from the model. The competing kinetics of carbon burn-off and LTCC sintering can also to be identified and deduced. In this carbon burn-off system, the burn-off environment will be in air and N_2 is the only major inert gas. The main reactant gas is oxygen. The ultimate aim of this study is to establish a model for the advancement of the understanding of fugitive carbon for embedded structure. This will provide the foundation for the evaluation of the LTCC sintering process.

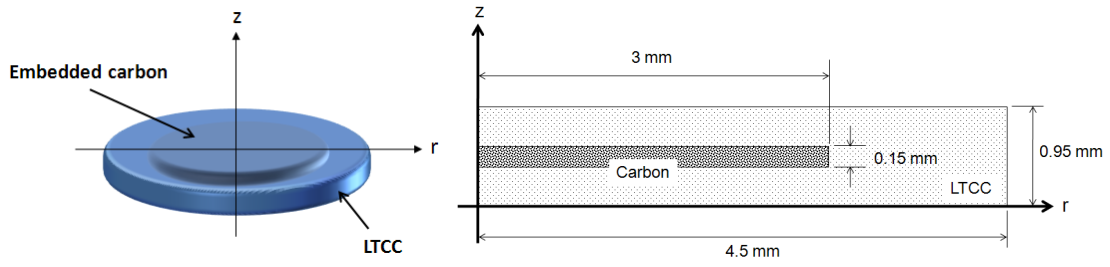

Figure 4-5 Schematic drawing of a simple embedded carbon LTCC disc structure with indicated dimension for a 6-layer LTCC structure.

4.4.1 Assumptions

Not all physical phenomena could be included in the model. It will be appropriate to examine here some of the major assumptions utilised:

- Carbon burn-off occurs in dry air environment with O_2 as the only reactant and N_2 as the only inert gas. CO_2 and CO are the primary products from the burn-off process.
- LTCC sintering is considered a non-reactive system with no chemical reaction involved.
- No external mass and heat transfer resistance will be imposed on the external surface boundary layer. This is because the free steam is not still and the temperature of interest is not high enough to result in significant effect of heat and mass resistance. This implies that mass and heat are freely carried away from the external surface.
- External surface boundaries are kept at constant concentration of gaseous species and expressed in term of mass fraction.
- Surface temperature follows closely the firing profile, and is not affected by any effect of heat transfer.
- No other structural change except porosity for both carbon and LTCC.
- No shape or size change of carbon layer is experienced due to possible percolation and fragmentation effect of carbon burn-off.
- No volume shrinkage of LTCC. Although the total shrinkage in LTCC sintering is in the range of 10 % – 30 %, it is most likely that burn-off is completed before any significant shrinkage.
- Carbon and LTCC layers are completely debinded and formed a rigid monolithic porous medium.

- The debinding process is not considered in the model.

4.4.2 Governing Equations

The system was initially assumed in the atmospheric air environment with no bulk or diffusive flow of gaseous species with a total gas pressure of 100 kPa (the standard atmospheric pressure). The initial mass fractions of the gaseous species were similar to that in the atmospheric air. The initial temperature was set at room temperature (298K) but subsequently followed the desired burn-off temperature profile.

A 2D axisymmetry mass transport model coupling with multicomponent chemical reactions with two distinct computation domains (Carbon and LTCC) was attempted. The computation domains as shown in Figure 4-6 were modelled as a porous medium. The surfaces were assumed as permeable walls. The gradient of the mass fractions of the gaseous species and the total gas pressure are all dependent on the diffusivity of the porous medium as well as the carbon burn-off rate.

The expected reactant concentration gradients in the sample during the sintering process are indicated in Figure 4-7. At low temperature (i.e. the initial sintering stage), burn-off is likely to be chemical reactivity controlled; the reactant profile will be following “a-A”, and the concentration could be assumed as constant throughout the sample volume due to a low burn-off rate. This is the time where the intrinsic kinetic parameters are determined for carbon burn-off as there is no significant external mass transfer resistance taking place. While the sample is heated up, the burn-off rate increases; the reactant profile will subsequently shift to profile “a-B”, “b-C”, “c-D” and eventually “d”. Profile “d” is an extreme case when the carbon burn-off is so fast that

virtually all the reactant is consumed at the carbon surface and the whole reaction appears as a surface reaction. The decreasing profile in the LTCC layer could also be due to the effect of sintering when pore closure is competing with the carbon burn-off. The LTCC layer in Figure 4-7 could be simply treated as a thick boundary layer with varying external mass transfer resistance due to the pore closure effect.

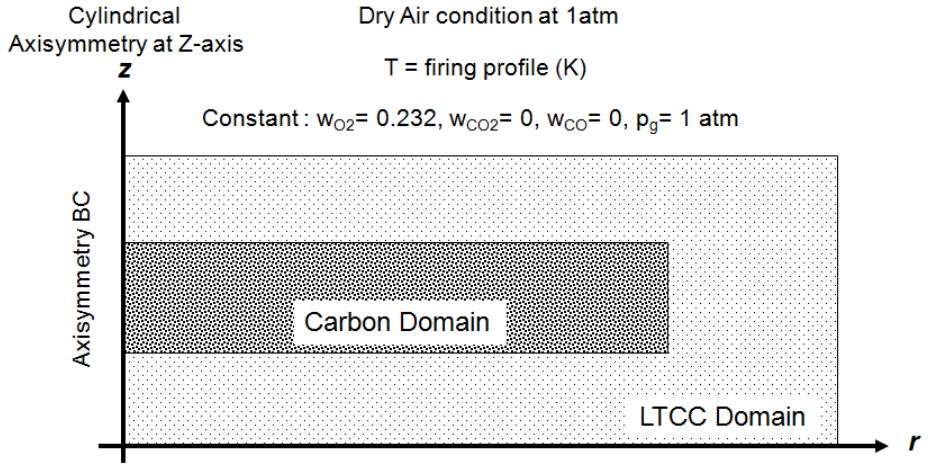

Figure 4-6 Axisymmetry 2D model for a simple embedded air cavity LTCC structure with separate computation domains of carbon and LTCC. Constant gas concentrations at atmospheric pressure were imposed at all boundaries as boundary conditions.

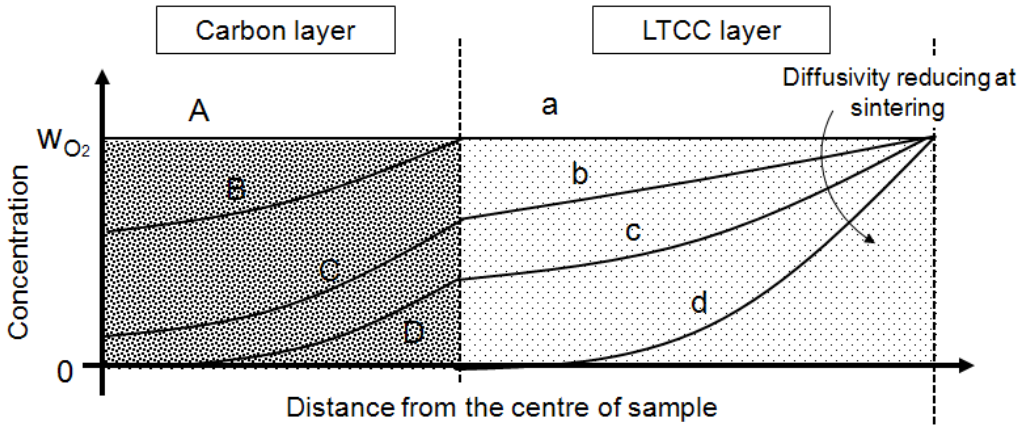

Figure 4-7 Reactant concentration profiles during the course of LTCC sintering.

The governing equations formulated in Section 4.2 were applied specifically to the carbon embedded LTCC sample. With the stated assumptions in Section 4.4.1, the following equations will be adequate to provide a complete solution for the model.

In both carbon and LTCC regions:

Mass balance for oxygen:

$$\rho_g \left(\frac{\varepsilon \partial(w_{O_2})}{\partial t} + v \cdot \nabla w_{O_2}\right) = \left(\nabla \cdot \rho_g D^e_{O_2} \nabla w_{O_2}\right) + \left(R_{O_2} - w_{O_2} R_T\right) \tag{4.53}$$

Mass balance for carbon dioxide:

$$\rho_g \left(\frac{\varepsilon \partial(w_{CO_2})}{\partial t} + v \cdot \nabla w_{CO_2}\right) = \left(\nabla \cdot \rho_g D^e_{CO_2} \nabla w_{CO_2}\right) + \left(R_{CO_2} - w_{CO_2} R_T\right) \tag{4.54}$$

Mass balance for carbon monoxide:

$$\rho_g \left(\frac{\varepsilon \partial(w_{CO})}{\partial t} + v \cdot \nabla w_{CO}\right) = \left(\nabla \cdot \rho_g D^e_{CO} \nabla w_{CO}\right) + \left(R_{CO} - w_{CO} R_T\right) \tag{4.55}$$

Mass balance for nitrogen:

$$w_{N_2} = 1 - w_{O_2} - w_{CO_2} - w_{CO} \tag{4.56}$$

Momentum balance for total gas phase:

$$\frac{\partial(\varepsilon \rho_g)}{\partial t} = \left(\nabla \cdot \rho_g \frac{\kappa}{\mu} \nabla p_g\right) + R_T \tag{4.57}$$

Energy balance for total gas phase:

$$C_p^e \frac{\partial T}{\partial t} + \nabla \cdot (-k_e \nabla T) = \Delta H_r(R_v) - C_p^e v \cdot \nabla T \quad (4.58)$$

In carbon region only,

Rate of carbon burn-off:

$$\frac{d\alpha_c}{dt} = a\rho_g A_c^* exp^{-\frac{E_C}{RT}} w_{O_2}(1 - \alpha_c) \quad (4.59)$$

In LTCC region only.

Rate of sintering:

$$\frac{d\alpha_L}{dt} = k_L(1 - \alpha_L) \quad (4.60)$$

Other constitutive equations:

$$\rho_g = \frac{p_g(M_g)}{RT} \quad (4.61)$$

Molar fraction of species:

$$x_i = \frac{w_i M_g}{M_i} \quad (4.62)$$

Summation of molar fraction for all gases:

$$\sum_{i=1}^{N} x_i = 1 \tag{4.63}$$

Ideal gas equation of state for partial gas pressure of species:

$$p_i = x_i p_g \tag{4.64}$$

Equations (4.53) to (4.60) are strongly coupled with the physical properties such as diffusivity, porosity, gas density and kinetic parameters functions of the carbon burn-off and LTCC sintering. The expressions for estimating the related physical properties were contained in Section 4.3. Together with the initial and boundary conditions, the variables required to solve for the model are $w_{O_2}, w_{CO_2}, w_{CO}, w_{N_2}, p_g, \alpha_c, \alpha_L,$ and T. The input to the model is the firing profile. This is the only process parameter in the LTCC sintering process that could be easily and practically adjusted and controlled.

4.4.3 Initial and Boundary Conditions

Constant mass concentration of gas species was imposed at the external surface without considering mass resistance over a stagnant film layer. Estimated from flow simulation, the superficial flow velocity past the sample was about 0.03 m/s when the air flow rate was set at 80 ml/min in the TGA environment. At this velocity the stagnant film layer is relatively thin. With a relatively low LTCC sintering temperature (i.e. below 1123 K) and a constant excess supply of air at the external surface, the effect of external mass resistance is not significant. The assumption that the stream is free to atmosphere gas pressure of 1 atm was appropriate. In addition, no heat transfer resistance was

imposed; the surface temperature at the external surface was set to follow closely to the firing profile.

Boundary conditions:

At r = 0, axisymmetry conditions applied,

$$\frac{\partial T}{\partial r} = \frac{\partial w_i}{\partial r} = 0 \quad (4.65)$$

At all surface boundaries,

$w_{O_2} = 0.232$

$w_{CO_2} = 0$

$w_{CO} = 0$

$p_g = 1\ atm$

$T = firing\ profile\ (T, t)$

At the interface between the LTCC and carbon layers, continuity of flux must be satisfied thus,

For mass conservation:

$$[n_i]_L = [n_i]_C \quad (4.66)$$

Where,

$$n_i = \rho_g (w_i v - D_i^e \nabla w_i) \quad (4.67)$$

For energy conservation:

$$[q]_L = [q]_C \tag{4.68}$$

Where,

$$q = C_p^e vT - k_e \nabla T \tag{4.69}$$

For Darcy's momentum equation:

$$\left[\rho_g v\right]_L = \left[\rho_g v\right]_C \tag{4.70}$$

Where,

$$v = \frac{\kappa}{\mu} \nabla p_g \tag{4.71}$$

Finally, the initial conditions (at t = 0) were given as,

For LTCC region,

$w_{O_2} = 0.232$

$w_{CO_2} = 0$

$w_{CO} = 0$

$p_g = 1\ atm$

$T = 323\ K$

$\alpha_L = 0$

For carbon region,

$w_{O_2} = 0.232$

$w_{CO_2} = 0$

$w_{CO} = 0$

$p_g = 1\ atm$

$T = 323\ K$

$\alpha_C = 0$

4.4.4 Material Properties and Kinetic Parameters

The carbon and LTCC material properties required for modelling were mostly measured physically with the appropriate instruments. Other properties not measured in this investigation were obtained from literature, datasheets and handbooks. The list of material properties employed in the modelling is contained in Table 4-1.

The values of kinetic parameters for the carbon burn-off were obtained by TGA kinetic analysis; see Chapter 3. The kinetic parameters for carbon burn-off with variable activation energy and pre-exponential factor with conversion were input into the computation in tabulated functions with interval of 0.1 degree level of carbon burn-off. Values between input data were obtained by interpolation using piecewise cubic function, except at both ends of the data where linear extrapolation was employed, see Figures 4-8 and 4-9 respectively for activation energy and apparent pre-exponential factor of carbon burn-off. Due to instability of burn-off observed at the initial and near to completion stages of the burn-off, rate parameter values were assumed constant at both end of the burn-off cycle.

Table 4-1 Material and kinetic properties for modelling.

Material properties	Values	Remarks
LTCC (HL2000) after debinding		
Initial porosity	0.5564	Measured by mercury porosimeter
Mean pore size in diameter	0.2016 μm	Measured by mercury porosimeter
Initial density	1346 kg/m^3	Measured by helium gas pycnometer
Fired density	2900 kg/m^3	HL2000 Design Guidelines [139]
Activation energy (sintering)	252.54 kJ/mol	TMA kinetic analysis (See Chapter 3)
Pre-exponential factor (sintering)	4.8×10^9 1/s	TMA kinetic analysis (See Chapter 3)
Thermal conductivity	3 W/m K	HL2000 Design Guidelines [139]
Heat capacity	1060 J/kg K	Use Mullite at 298 K [132]
Carbon Tape after debinding		
Initial porosity	0.5453	Measured by mercury porosimeter
Mean pore size in diameter	0.0676 μm	Measured by mercury porosimeter
Mean grain size in diameter	0.7676 μm	Measured by light scattering
True density	1947.7 kg/m^3	Measured by helium gas pycnometer
Activation energy (burn-off)	See Figure 4-8	TGA kinetic analysis (See Chapter 3)
Pre-exponential factor (burn-off)	See Figure 4-9	TGA kinetic analysis (See Chapter 3)
Thermal conductivity	Empirical expression	Appendix A
Heat capacity	Empirical expression	Appendix A
Gas Species (O_2, CO, CO_2, N_2)		
Thermal conductivity	Empirical expression	Appendix A
Heat capacity	Empirical expression	Appendix A
Viscosity	Empirical expression	Appendix A

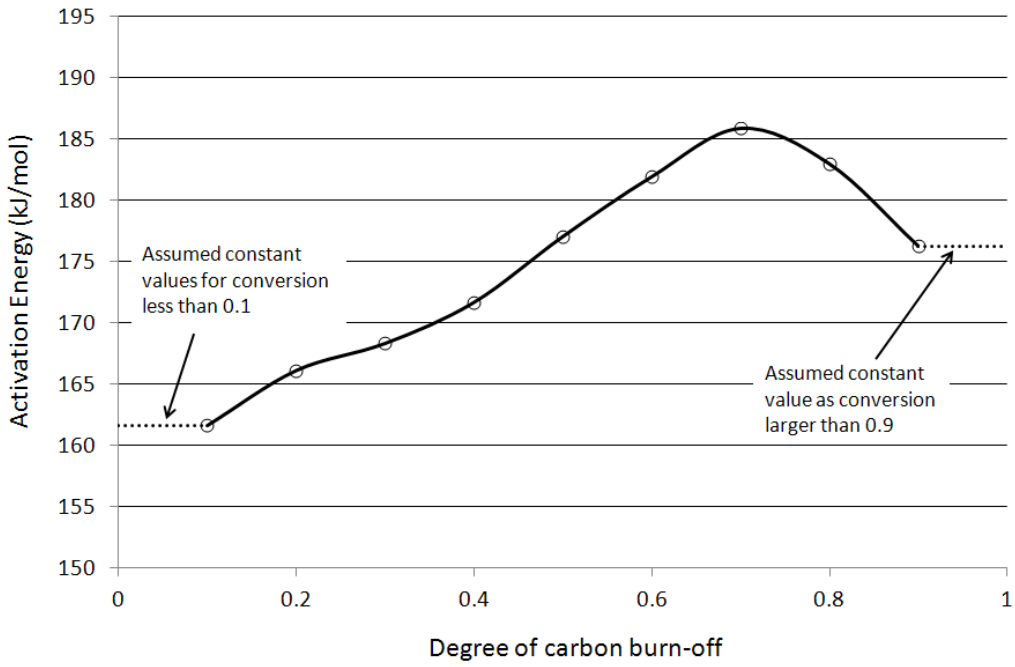

Figure 4-8 Apparent carbon burn-off activation energy vs. conversion for carbon burn-off model.

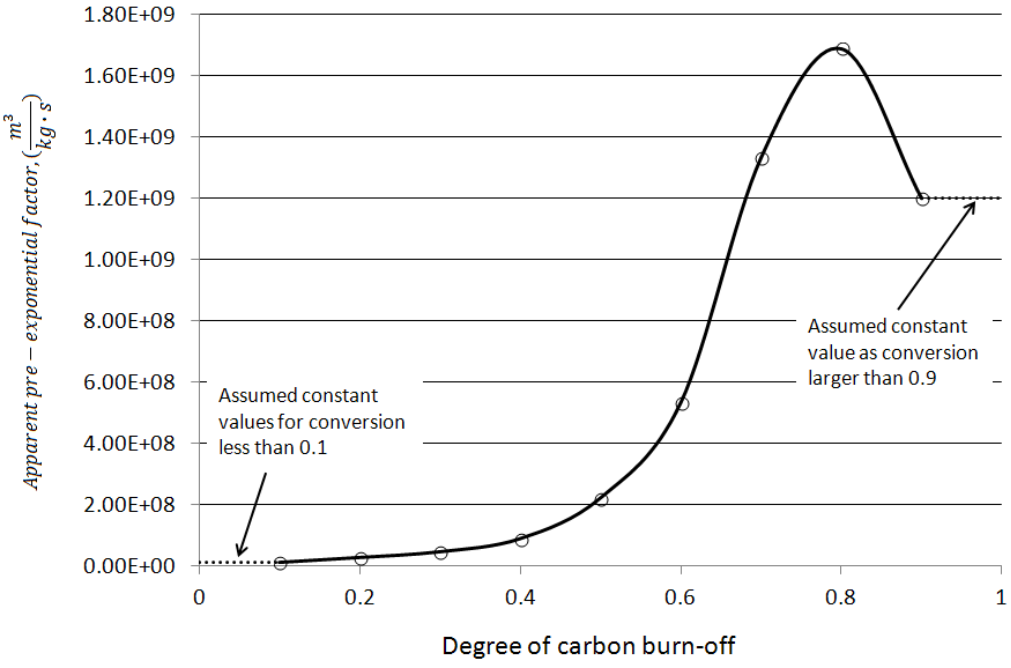

Figure 4-9 Apparent pre-exponential factor vs. conversion for carbon burn-off model.

The porosity of carbon during burn-off could be estimated from the initial porosity and the degree of burn-off where complete burn-off with no solid residue is expected [102,131],

$$\varepsilon_C = \varepsilon_{C0} + \alpha_c(1 - \varepsilon_{C0}) \quad (4.72)$$

Where ε_{C0} is the initial porosity of carbon before burn-off.

The bulk density for carbon during burn-off is expressed in term of the true density of carbon as,

$$\rho_{Cb} = \rho_{Ct}(1 - \varepsilon_C) \quad (4.73)$$

Where ρ_{Ct} is the true density of carbon.

For LTCC, the model for porosity changes during sintering as described in Section 4.3.4, Figure 4-3 is used. The LTCC density during sintering is assumed to change linearly with the degree of shrinkage as shown in Figure 4-10.

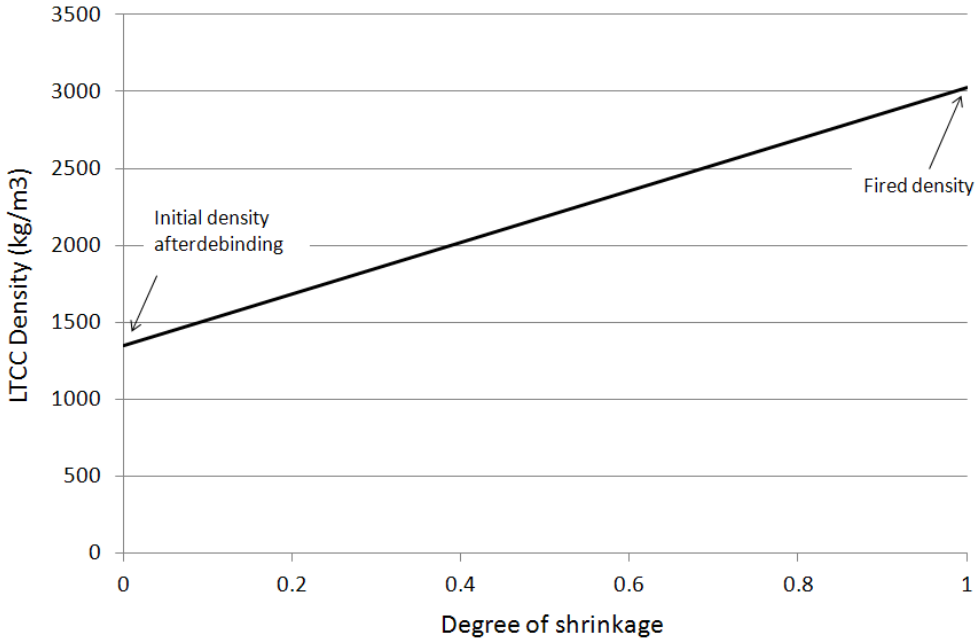

Figure 4-10 Linear estimation of density change of LTCC during sintering.

4.4.5 Numerical Method

The model was coded in COMSOL Multiphysics® (version 3.5) which is a commercial FEM software specifically designed for multiphysics modelling. Chemical engineering module which includes mass transfer and flow in porous medium was employed in conjunction with the classic PDE module for the burn-off and sintering models. All equations were coded with transient analysis type and were solved with the time-dependent solver. The numerical model was tested for mesh and time step sensitivity using coarse and fine meshes with different time step intervals. The meshing and time steps were optimised by the burn-off curve (time to reach 0.99 conversion). Automatic mesh generation with triangular elements having a denser mesh for the thin carbon layer was employed. Approximately 4000 elements were employed for all sample configurations, with a time step of 10 s, 15 s or 20 s for 20 K/min, 10 K/min or 5 K/min firing profile respectively. A typical 6-layer LTCC / 0.15 mm carbon embedded 2D meshing is shown in Figure 4-21.

COMSOL provides only standard mass transfer governing equations in molar concentration quantity for a general formulation of chemical reaction engineering. However, to handle all the formulated equations in this investigation, the coefficients were replaced with the appropriate coefficient expressions, in particular the diffusivity, velocity and reaction source term. With this modification, the model could be solved by the COMSOL solver.

For the carbon region, equations to be solved are species mass conservation equations (equations 4.53-4.55), momentum equation (equation 4.57), energy balance equation (equation 4.58), carbon burn-off equation (equation 4.59), equation of state (equation 4.61), and the summation of mass fraction (equation 4.56).

For the LTCC region, the equations are species mass conservation equations (equations 4.53-4.55), momentum equation (equation 4.57), energy balance equation (equation 4.58), LTCC sintering equation (equation 4.60), equation of state (equation 4.61), and the summation of mass fraction (equation 4.56).

All equations in both regions are solved simultaneously with the initial and boundary conditions for $w_{O_2}, w_{CO_2}, w_{CO}, w_{N_2}, p_g, \alpha_c, \alpha_L,$ and T.

4.4.6 Experimental

The same experimental setup was used as in carbon burn-off kinetic analysis in Chapter 3. The only difference was the sample configuration. These experimental runs were mainly used for model validation. The different structure configurations are shown in Figure 4-11. For easy reference, as shown in Figure 4-11, the sample structures were

named as (a) 2-layer LTCC structure, (b) 6-layer LTCC structure, and (c) 12-layer LTCC structure. For this model validation, the thickness of embedded carbon used was restricted to 0.05 mm (2 mil), 0.15 mm (6 mil) and 0.25mm (10 mil). The LTCC system was based on HL2000 LTCC system, with each tape having a nominal thickness of 0.125 mm.

To extensively test the model, experiments were conducted with variations of LTCC layer thickness and carbon layer thickness. Repeated runs were also conducted (2 to 3 runs). The details are as follows:

- 6-layer LTCC structure embedded with 0.05mm, 0.15 mm or 0.25 mm carbon tape under a constant heating rate LTCC firing profile of 5 K/min, 10 K/min or 20 K/min.
- 0.15mm carbon embedded in LTCC layers of 2, 6, or 12 layers under constant heating rate LTCC firing profile of 5 K/min, 10 K/min, or 20 K/min.

The LTCC firing profile could be found in Figure 4-12. The carbon burn-off and burn-off rate obtained were compared with the results predicted by the model.

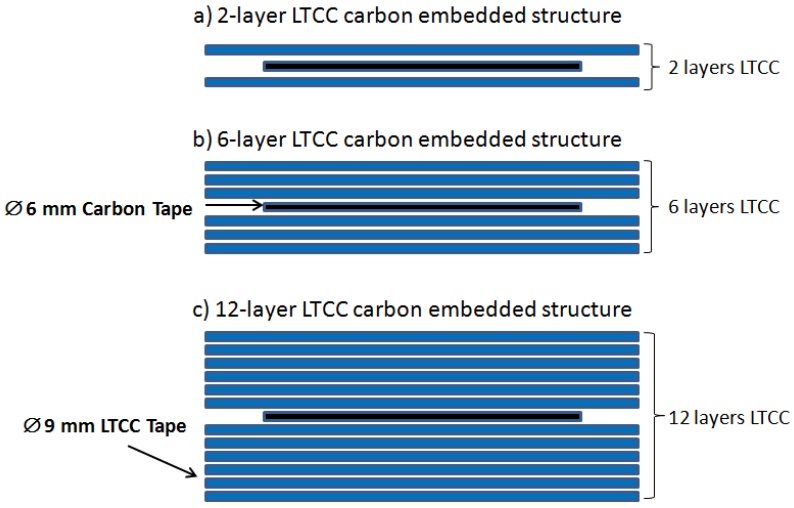

Figure 4-11 Sample configurations for model validation experiments.

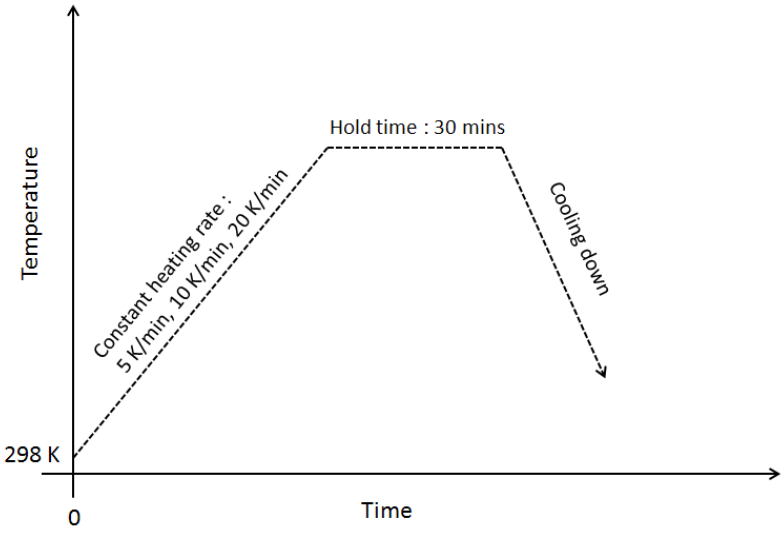

Figure 4-12 TGA experimental temperature profile (similar to actual LTCC firing profile).

4.4.7 Comparisons of Experimental and Modelled Burn-off Curves

A relatively easier way to validate the model is to use the experimental TGA results, but based on the burn-off conversion curve with respect to time or temperature. Other data that could be derived from the TGA curve is the derivative of carbon burn-off relative to time or temperature i.e. rate of carbon burn-off. For modelling, burn-off conversion expressed as an overall carbon conversion over the area of the geometry was used to compare with the experimentally measured results.

The overall carbon conversion or degree of carbon burn-off could be expressed as,

$$[\alpha_c]_{ave} = \frac{\int \alpha_c \, dAr_c}{\int dAr_c} \tag{4.74}$$

Where Ar_c is the area of geometry of the carbon layer.

The rate of carbon burn-off can be expressed as,

$$\frac{d([\alpha_c]_{ave})}{dt} \; or \; \frac{d([\alpha_c]_{ave})}{dT} \tag{4.75}$$

The rate of burn-off could be evaluated graphically by differentiating the $[\alpha_c]_{ave}$ curve with time or temperature.

Similarly, the sintering curve was determined from the model as,

$$[\alpha_L]_{ave} = \frac{\int \alpha_L \, dAr_L}{\int dAr_L} \tag{4.76}$$

Where Ar_L is the area of LTCC layers.

Various cases of sample configuration and firing profile as detailed in the experimental section were modelled and compared to the measured TGA results. Figures 4-13 to 4-15 show the effect of carbon thickness affecting the carbon burn-off while Figures 4-16 to 4-18 reveal the effect of LTCC layer.

(i) Effect of carbon layers

Three different thicknesses (0.05 mm, 0.15 mm, 0.25 mm) of carbon layer embedded in a 6-layer structure LTCC were employed to investigate the effect of carbon layer thickness in embedded carbon burn-off. The result of TGA experimental burn-off curves compared with the modelled results of similar burn-off curves are shown in Figures 4-13 to 4-15.

TGA measured burn-off curves at 5 K/min, 10 K/min, and 20 K/min all demonstrated slower burn-off for 0.25mm thick embedded carbon. The burn-off curves of 0.25 mm thick carbon layer at all heating rates seemed to have a distinct separation from the 0.05 mm and 0.15 mm results. The burn-off of 0.05mm and 0.15 mm thick carbon layer revealed little effect on the carbon thickness, no distinct burn-off curves was observed between the two thicknesses at all heating rates. The data for both thicknesses were overlapping with relatively large data scattering.

The predicted burn-off curves observed the same trend as the experimental TGA curves, namely thinner carbon burns faster than the thicker carbon. The predicted burn-off curves were systematically shifted with the carbon thickness due to the mass diffusion resistance of reactant induced by the carbon thickness. The predicted and experimental burn-off curves of 0.25 mm thick carbon layer do not agree well at 5 K/min and 10 K/min; the modelling results have faster initial burn-off than the experimental results. However, good agreements between experimental and predicted results were obtained at the higher heating rate of 20 K/min.

The distinct slow burn-off observed experimentally from the 0.25 mm thick carbon layer is likely caused by the effect of surface catalytic reaction between the LTCC and carbon layer. Carbon burns off by the initial surface catalytic reaction but will slow down with the gradually separation of the initial intimate contact of the LTCC. This "break-off" will slow down the total carbon burn-off. This was observed when a relatively thick carbon layer was used as an embedded layer (demonstrated by all the 0.25 mm thick carbon burn-off curves in Figures 4-13 to 4-15). In contrast, for thin carbon layer, the "break-off" was not as obvious because the initial catalytic burn-off

had already consumed a major portion of the carbon layer. Thus, a distinct slow down in burn-off was not observed (demonstrated by all 0.05 and 0.15 mm thick carbon burn-off curves in Figures 4-13 to 4-15). For a high heating rate, this "break-off" effect may not as obvious even for thick carbon layer as the reaction rate after "break-off" was still near to the initial catalytic reaction rate. For example, as shown in Figure 4-15, the 0.25 mm predicted burn-off curve agrees well with the experimental curve when the model was based on the simple catalytic reaction rate. This unique burn-off phenomenon was not considered in this model and thus the modelling results do not agree well with experimental results for 0.25 mm thick carbon layer at low heating rates. However, it should be noted here that for most practical applications, thin carbon layer was used and thus the "break-off" effect will not significant.

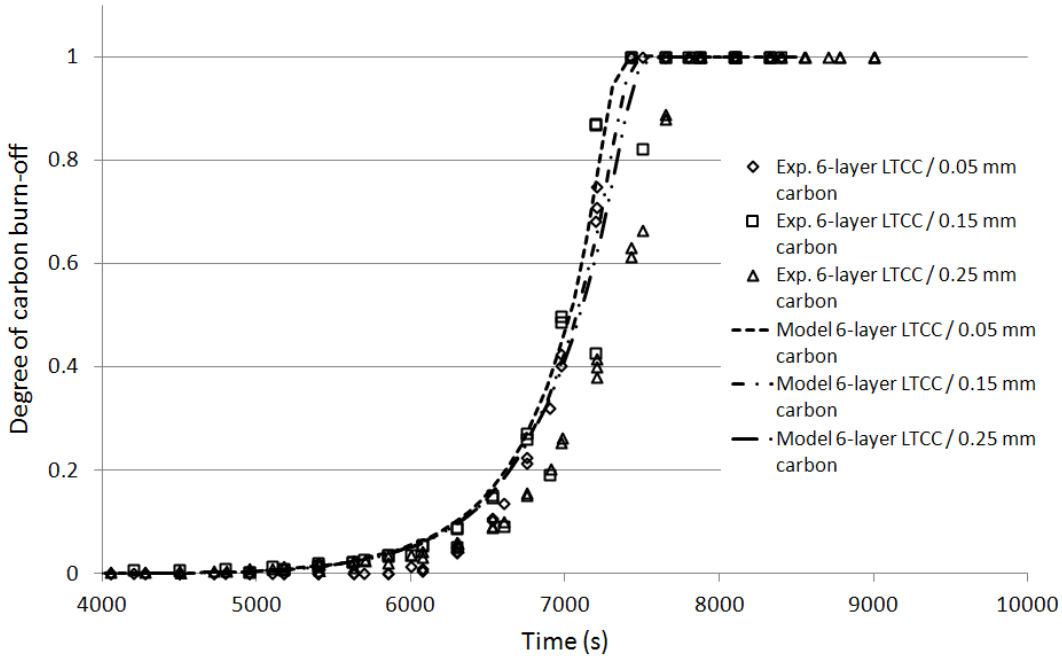

Figure 4-13 Effect of carbon tape layer at 5 K/min LTCC firing profile.

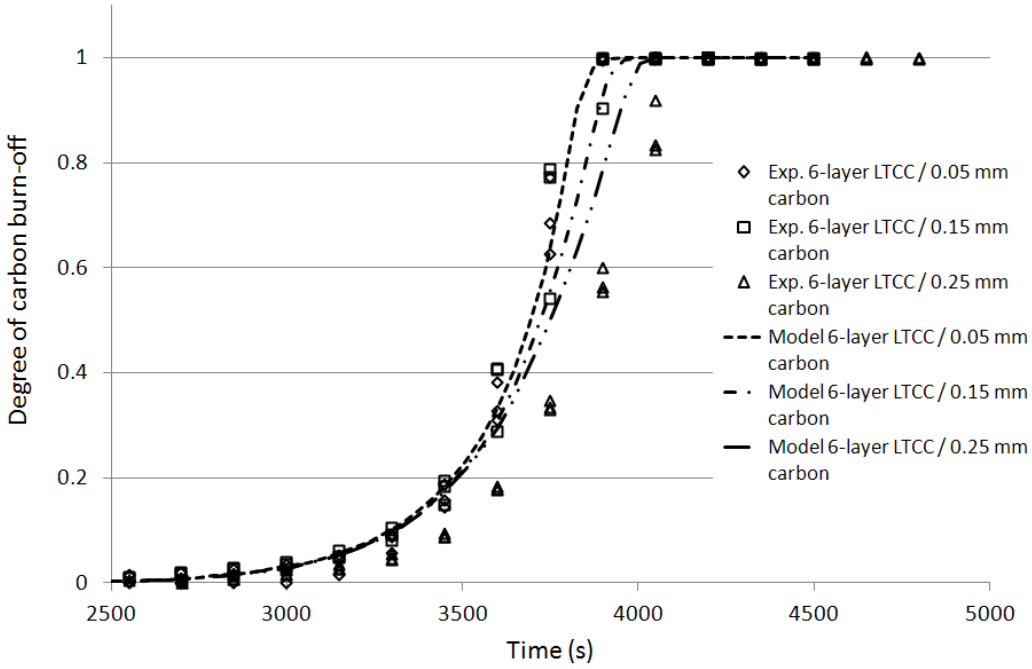

Figure 4-14 Effect of carbon tape layer at 10 K/min LTCC firing profile.

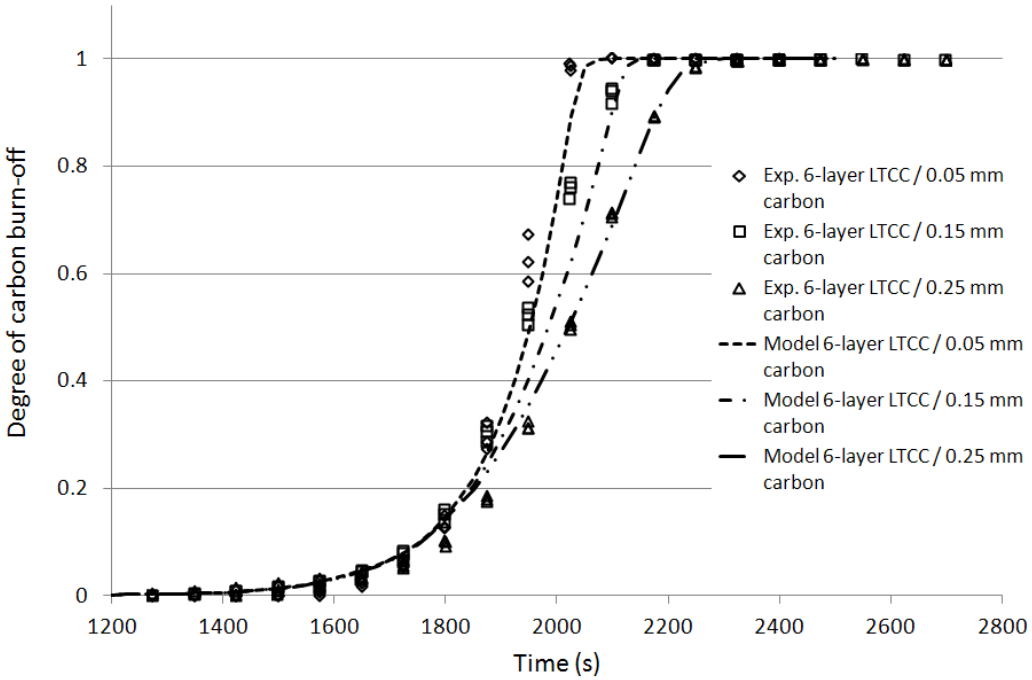

Figure 4-15 Effect of carbon tape layer at 20 K/min LTCC firing profile.

(ii) Effect of LTCC layers

The modelling results obtained from the 0.15 mm embedded carbon in 2, 6 and 12 layer structure LTCC are shown in Figures 4-16 to 4-18 for a constant heating rate profile of 5 K/min, 10 K/min or 20 K/min respectively. As LTCC pore closure has a strong effect on gas diffusivity, having an experimental based phenomenological LTCC porosity model is essential as a theoretical model specifically for LTCC sintering is hard to come by due to the complexity of glass/ceramics system of LTCC. The experimental porosity model in this investigation was tested as a whole by comparing the carbon burn-off through the various LTCC layers structures.

The effect of LTCC layers on carbon burn-off was reasonably well modelled for 2, 6, and 12 layers structures. At high burn-off rate, i.e. at a heating rate of 20 K/min, for a 12-layer LTCC structure, both model predictions and experimental results showed obvious incomplete burn-off phenomenon, see Figure 4-18. Only about 90% carbon burn-off was achieved. This indicates that carbon burn-off had terminated due to an insufficient supply of O_2 caused by LTCC sintering. This resulted from the competing kinetics of carbon burn-off and LTCC sintering which caused the undesired incomplete burn-off of embedded carbon.

In a practical application, such an incomplete carbon burn-off at this operating condition is usually not possible due to equipment limitation of having a high heating rate of 20 K/min. In addition, such a high ramp rate is undesirable as it could create large thermal gradient over the sample. Interfacial stresses initiated between layers could be severe. A lower heating rate of 10 K/min is generally acceptable and adopted by production lines. However, even at this lower heating rate, for thick LTCC layers

and thicker carbon layer, delay carbon burn-off could still probably occur due to the large diffusion resistance. This phenomenon is demonstrated in the numerical predictions of an 18-layer LTCC/0.25 mm embedded carbon structure in Figure 4-19. The dotted line indicates that there is incomplete carbon burn-off at about 94%.

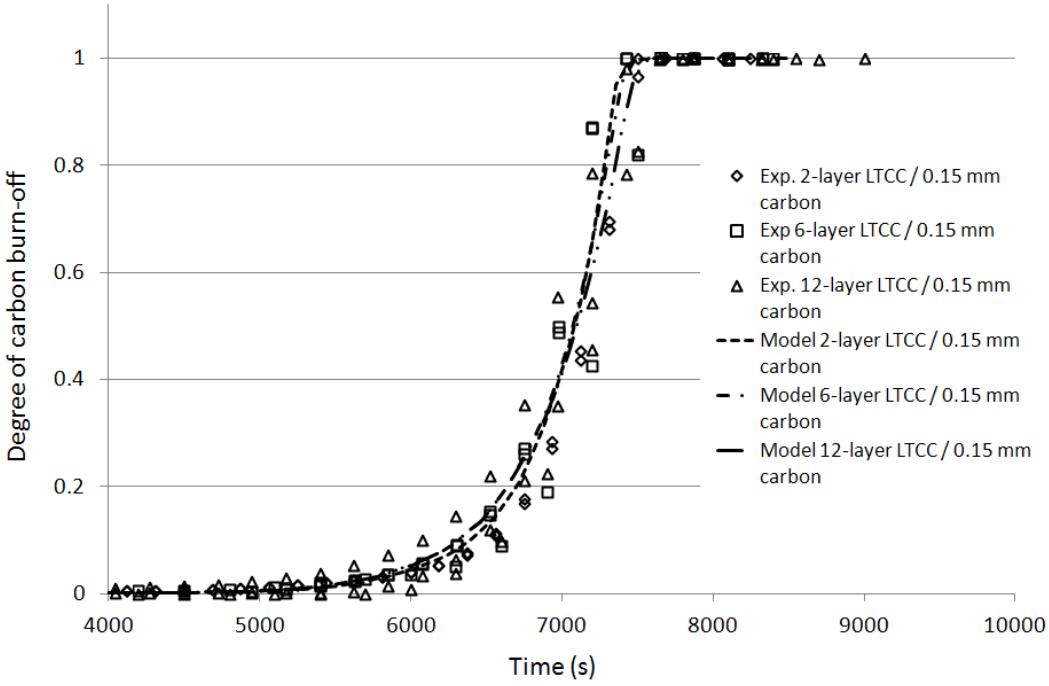

Figure 4-16 Effect of LTCC layer at 5 K/min LTCC firing profile.

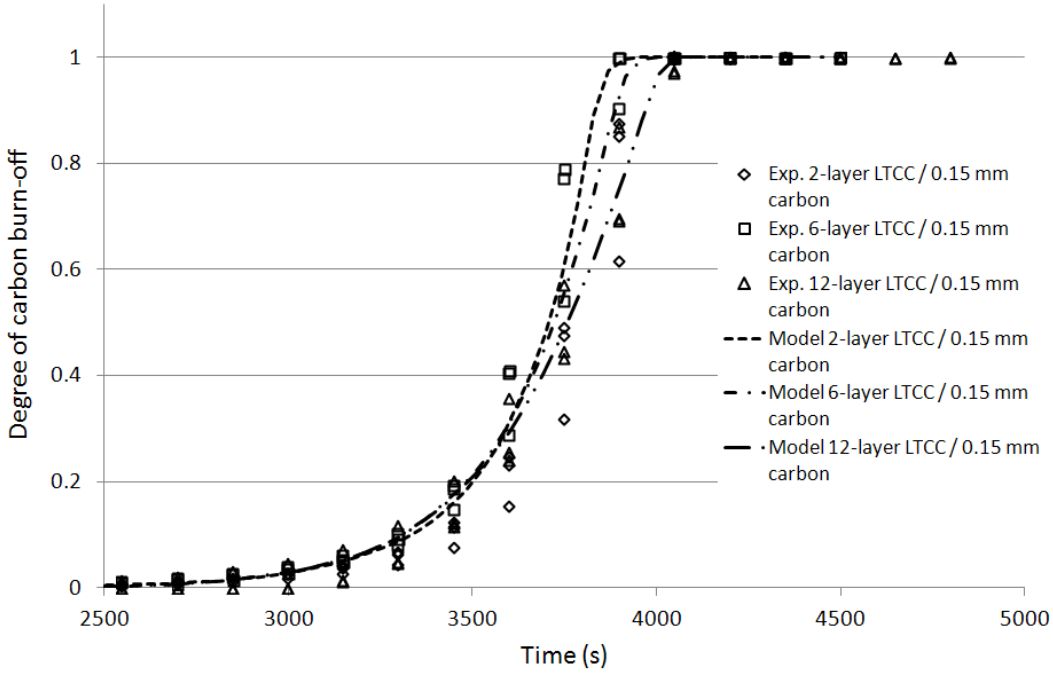

Figure 4-17 Effect of LTCC layer at 10 K/min LTCC firing profile.

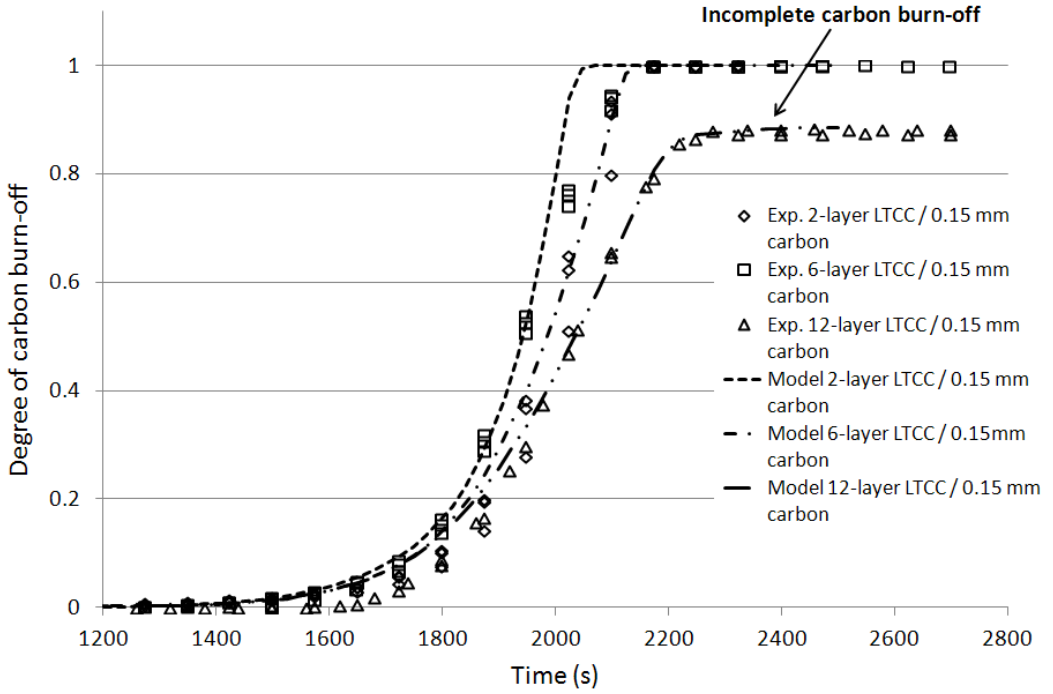

Figure 4-18 Effect of LTCC layer at 20 K/min LTCC firing profile.

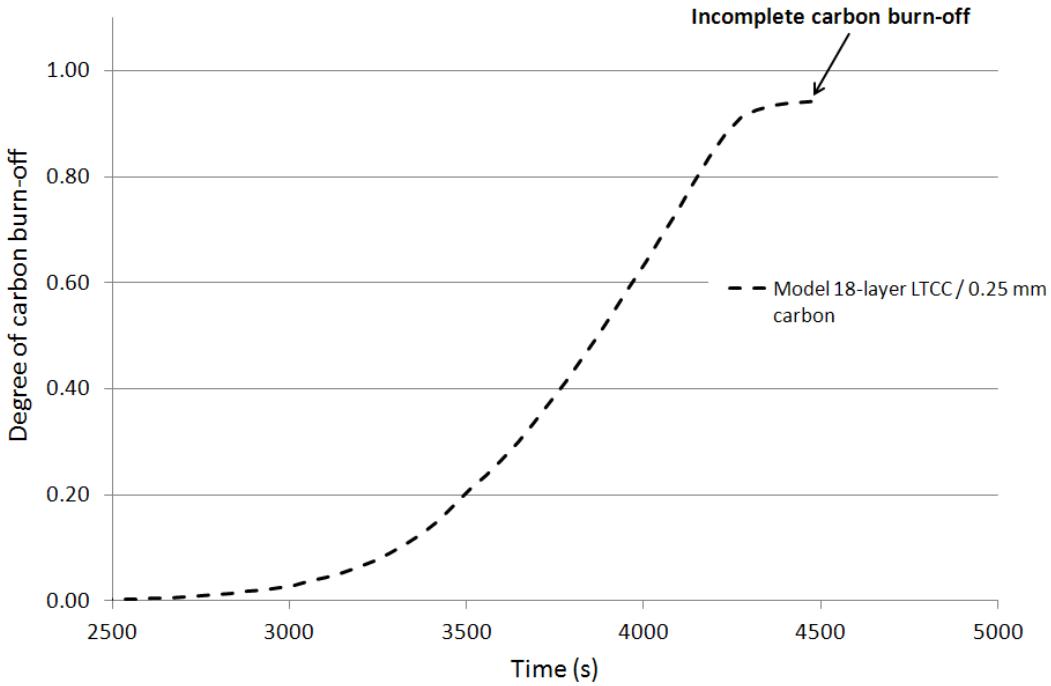

Figure 4-19 Effect of competing kinetics of carbon burn-off and LTCC sintering at 10 K/min for an 18-layer LTCC embedded structure.

Besides the above qualitative comparison between the modelled and measured results based on the burn-off curve for the effect of carbon and LTCC layers, the results obtained in term of sintering time to reach 99 % of carbon burn-off are listed in Table 4-2. The average deviation was taken from three experimental runs and arithmetically compared to the measured readings. The average deviation is expressed as,

$$Ave.deviation: \frac{[t_{\alpha=0.99}]_{modelled}-[t_{\alpha=0.99}]_{measured}}{[t_{\alpha=0.99}]_{measured}} \; x \; 100\% \qquad (4.77)$$

The deviations for the various runs with different configurations were less than 5 %, a rather good result for employing a simple first order reaction model for both carbon burn-off and LTCC sintering.

Table 4-2 Comparison between predicted and measured burn-off curves for time to reach 99% of carbon burn-off.

Embedded carbon configuration	Modelling Results (Time to reach 99% carbon burn-off), (s)	TGA Results (Time to reach 99% carbon burn-off), (s)	Average deviation based on equation (4.77), (%)
Constant heating rate profile : 5 K/min			
2-Layer LTCC/0.15 mm Carbon	7520	7504	0.2
6-Layer LTCC/0.05 mm Carbon	7480	7329	2.1
6-Layer LTCC/0.15 mm Carbon	7480	7416	0.9
6-Layer LTCC/0.25 mm Carbon	7565	7751	-2.4
12-Layer LTCC/0.15 mm Carbon	7565	7559	0.1
Constant heating rate profile : 10 K/min			
2-Layer LTCC/0.15 mm Carbon	3913	3980	-1.7
6-Layer LTCC/0.05 mm Carbon	3915	3850	1.7
6-Layer LTCC/0.15 mm Carbon	3960	3886	1.9
6-Layer LTCC/0.25 mm Carbon	4050	4135	-2.0
12-Layer LTCC/0.15 mm Carbon	4050	4034	0.4
Constant heating rate profile : 20 K/min			
2-Layer LTCC/0.15 mm Carbon	2047	2135	-4.1
6-Layer LTCC/0.05 mm Carbon	2075	2027	2.4
6-Layer LTCC/0.15 mm Carbon	2150	2143	0.4
6-Layer LTCC/0.25 mm Carbon	2250	2265	-0.6
12-Layer LTCC/0.15 mm Carbon*	2200	2177	1.1

Note: *incomplete burn-off, Time to reach 85% burn-off was taken instead.

(iii) Effect of firing profiles

The model was also validated on an arbitrary multi-step firing profile consisted of isothermal hold steps. The burn-off curve obtained from the model along with the measured TGA curve is shown in Figure 4-20. The modelling burn-off curve agrees well with the experimental measured curve, with the same trend of burn-off characteristics. As such, the model developed provides the possibility to model the carbon burn-off at various users' defined firing profile. This is a useful tool especially for optimisation of LTCC sintering profile.

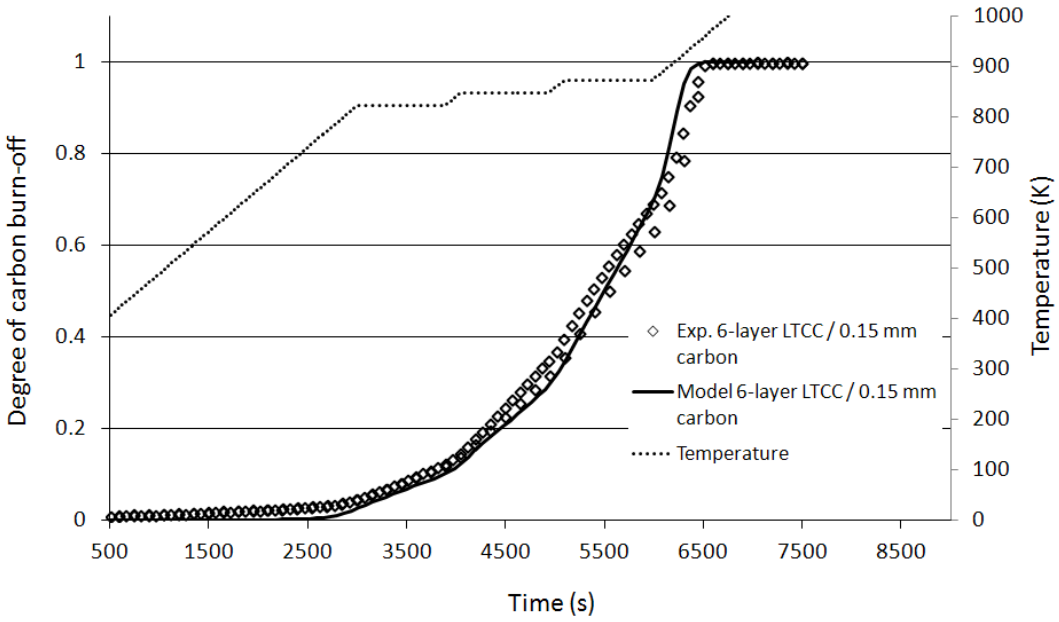

Figure 4-20 Carbon burn-off curve at arbitrary multi-step LTCC firing profile.

(iv) Total gas pressure

One of the important sintering parameters is the total gas pressure in the carbon layer. This internal pressure build-up in the system, if excessive, will cause severe swelling or cracking of the embedded structure. For analysis, the internal pressure was taken from the model results at the centre point in the carbon layer where the maximum pressure was occurring during the course of burn-off. The location of the centre point is shown as Point 1 in Figure 4-21. This pressure value could not be measured experimentally, and thus modelling had to be relied upon.

Based on the typical heating rate of 10 K/min, the pressure build-up in the carbon embedded cavity for different LTCC and carbon layers were compared, see Figure 4-22. Generally, build up pressure increased with LTCC layers and with carbon layers. The maximum pressure could reach 1.81 x 10^5 Pa. This is a sufficiently high pressure to

cause distortion of the LTCC layer when it was in its softening stage. Internal pressure also increased with an increase in heating rate as shown in Figure 4-23.

At Point 1 for the 6-layer LTCC structure, the plotted pressure build-up curves were observed to have the same trend as the burn-off curves under various heating rates, see Figure 4-24. The maximum peaks occurred almost at the same times indicating the close relationship as in equation (4.59). This indicates that for fugitive carbon used as embedded inserts, if the rate of burn-off could be lower, the burn-off pressure build up would be reduced. This will lead to a reduction of the risk of sample swelling. However, some pressure build-up may be essential to support the structure during sintering (glass softening) phase. The total gas pressure in the carbon layer could be used to optimise the LTCC process especially the firing profile for sintering without multiple physical testings of the sample in the furnace. Rate of burn-off could be reduced by using a low burn-off temperature or at a low heating rate. However, low temperature burn-off will result in much longer sintering time, which is not desirable from a production perspective. Furthermore, it may result in poor fired properties due to coarse grain growth and premature glass crystallisation.

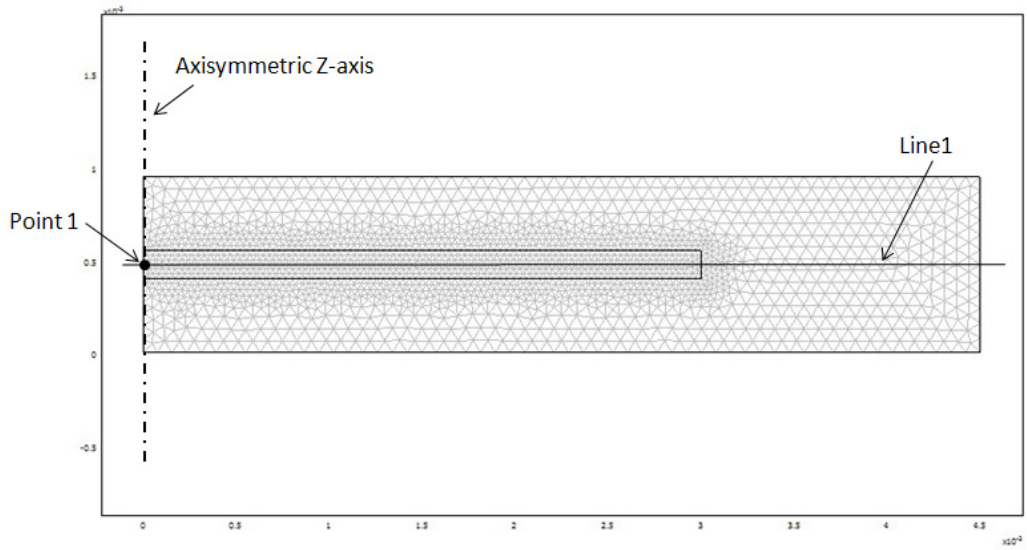

Figure 4-21 FEM mesh of sample configuration of 6-layer LTCC / 0.15 mm carbon embedded structure. Point 1 indicated is at the centre of the embedded carbon layer. (Note: half model shown as model symmetrical about centreline)

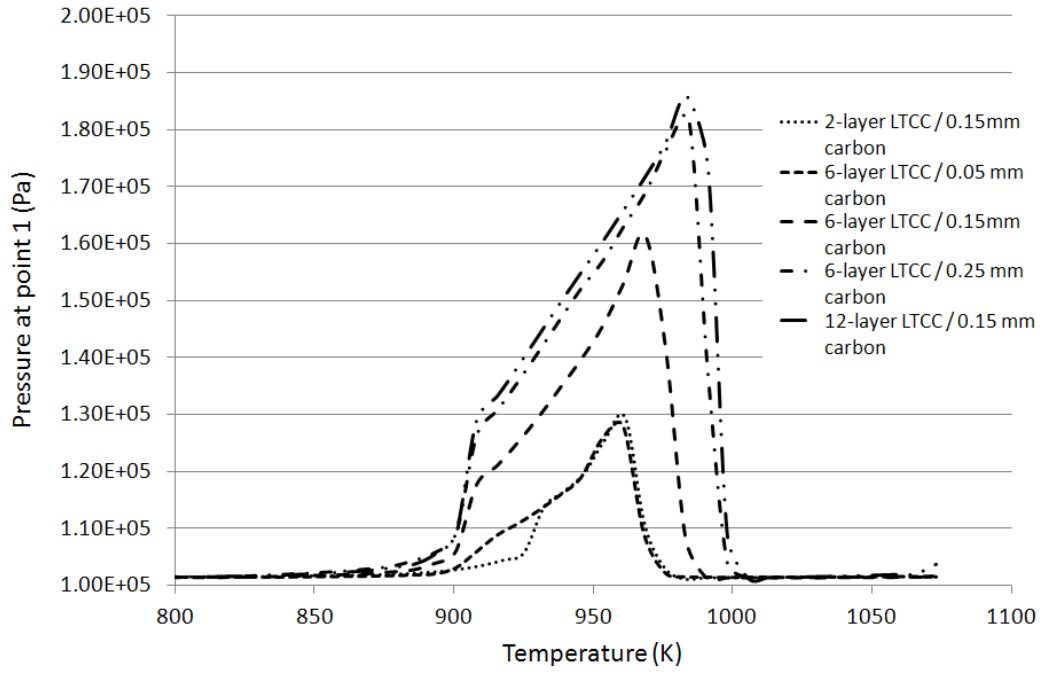

Figure 4-22 Pressure at point 1 with various LTCC layers and carbon layer thickness at 10 K/min constant heating profile.

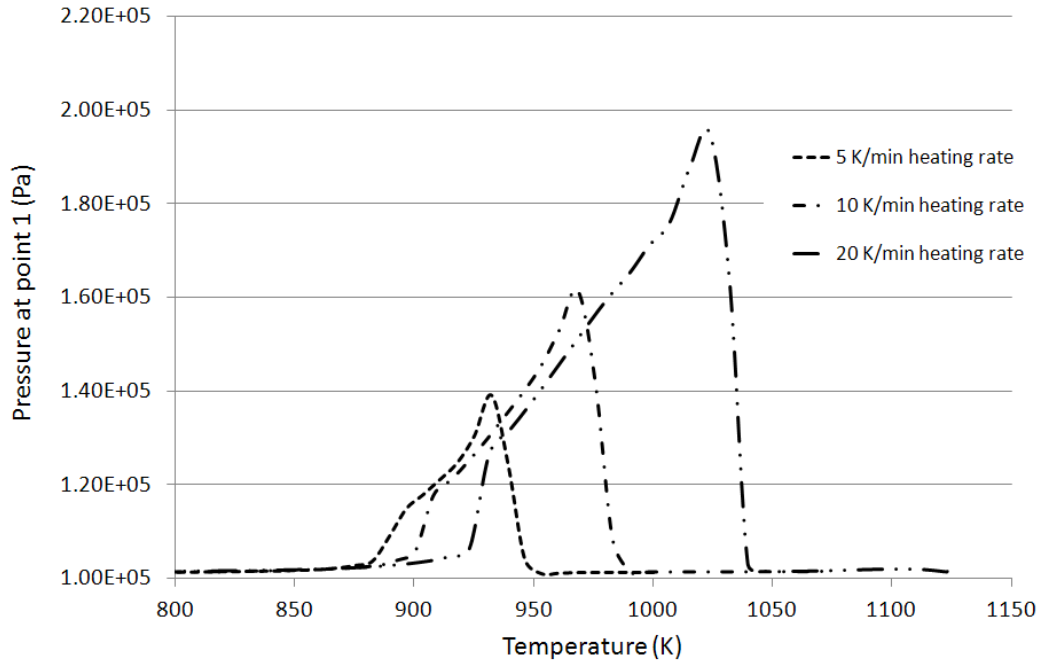

Figure 4-23 Pressure at point 1 of 6-layer LTCC / 0.15 mm carbon embedded structure with various heating rate firing profiles.

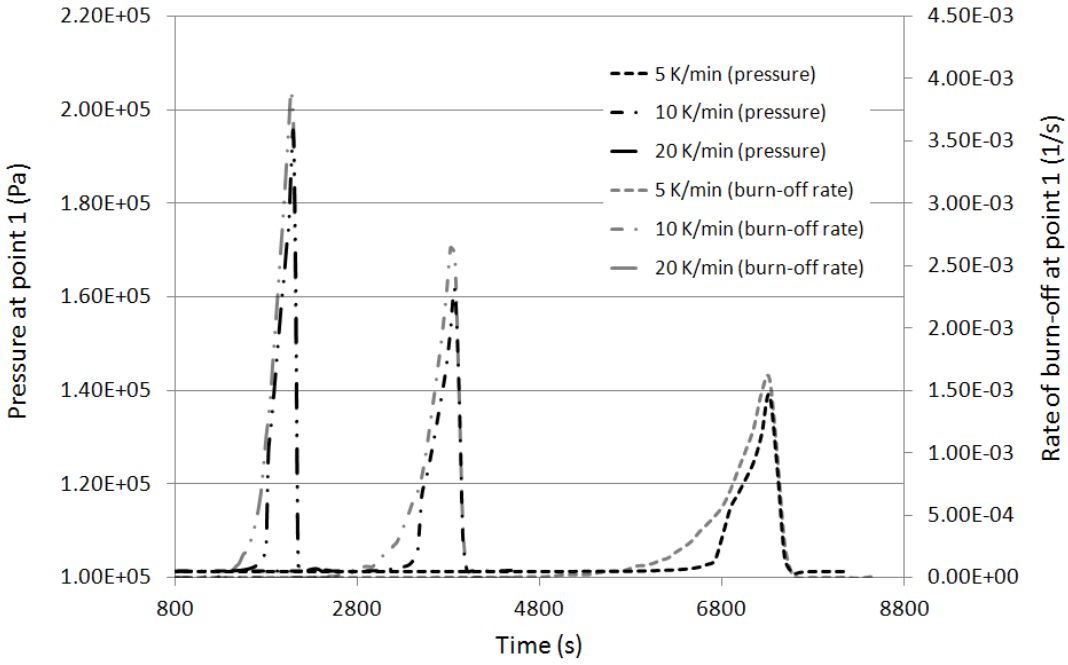

Figure 4-24 Plots of burn-off rate and pressure build up during the course of reaction for 6-layer LTCC / 0.15 mm carbon embedded structure.

(v) Reactant (O_2) concentration profile

O_2 concentration was a function of the location and the burn-off conversion. Instants of O_2 concentration profile along the centre line of the carbon layer at conversion levels of 0.05, 0.25, 0.50, 0.75, and 0.95 are shown in Figure 4-25 for a 12-layer/0.15 mm carbon structure. The location of the centre plane of the carbon layer is shown as Line 1, see Figure 4-21. Burn-off began with a constant concentration of O_2. At low level of conversion ($[\alpha_c]_{ave} = 0.05$), the concentration was almost constant throughout the sample due to low initial burn-off rate. As burn-off proceeded, at higher conversion, the consumption of O_2 gradually increased and eventually reached the maximum rate of burn-off at about 0.75 conversion level. When approaching complete burn-off ($[\alpha_c]_{ave} = 0.95$), the O_2 concentration began to decrease and finally returned back to its initial concentration at complete burn-off. Due to the nature of porous structure and also the pore closure effect of LTCC sintering, the LTCC layer behaved like a mass diffusion resistance layer with large concentration gradient in the LTCC layer.

Under the situation of competing kinetic, i.e. in the experimental run of 12-layer/0.15 mm carbon at 20 K/min, incomplete carbon burn-off was observed. The O_2 concentration profiles for such a situation are shown in Figure 4-26. At $[\alpha_c]_{ave} = 0.88$, where carbon burn-off was terminated, O_2 dropped to zero at the carbon/LTCC interface. This is due to the high mass diffusion resistance of O_2 caused by the sintering of the LTCC layer.

The concentration profile modelled matched well with the expected profile as depicted in Figure 4-7.

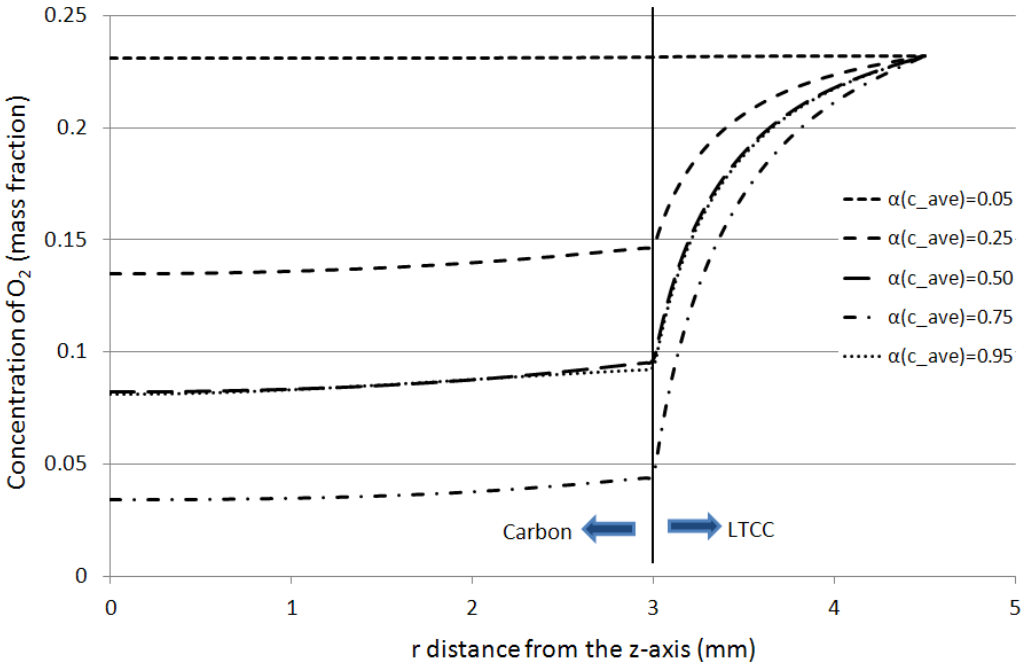

Figure 4-25 Mass concentration of reactant O_2 expressed in mass fraction along Line 1 during the course of burn-off (12-layer LTCC / 0.15 mm carbon embedded structure at 10 K/min).

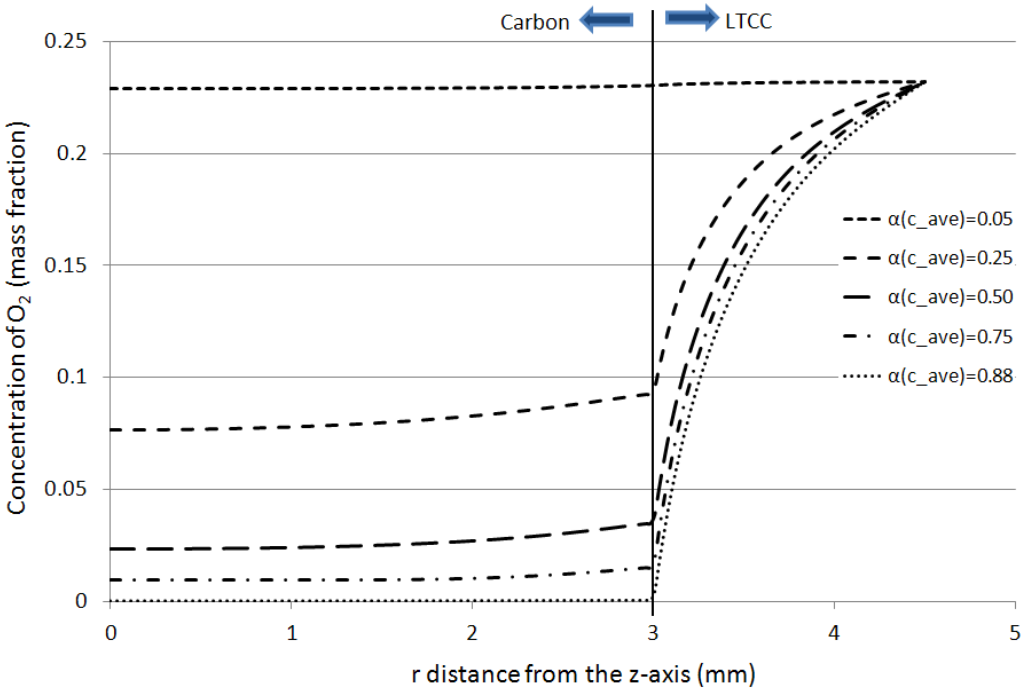

Figure 4-26 Mass concentration of reactant O_2 expressed in mass fraction along Line 1 during the course of burn-off (12-layer LTCC / 0.25 mm carbon embedded structure at 20 K/min) showing incomplete carbon burn-off at 0.88 conversion.

(vi) Species concentration profiles

For a better understanding of the concentration profiles of reactant and product gases during the course of burn-off, the gaseous concentrations are depicted in Figure 4-27 along with the carbon burn-off curve at Point 1, the centre point of the carbon layer. The consumption of O_2 was associated with the generation of CO_2 and CO in accordance with the product gas ratio as indicated in our earlier formulation, see equation (3.3) in Chapter 3, Section 3.1. The total gas phase concentration was balanced by the abundant quantity of N_2. The total gas phase mass fraction must always equal to unity.

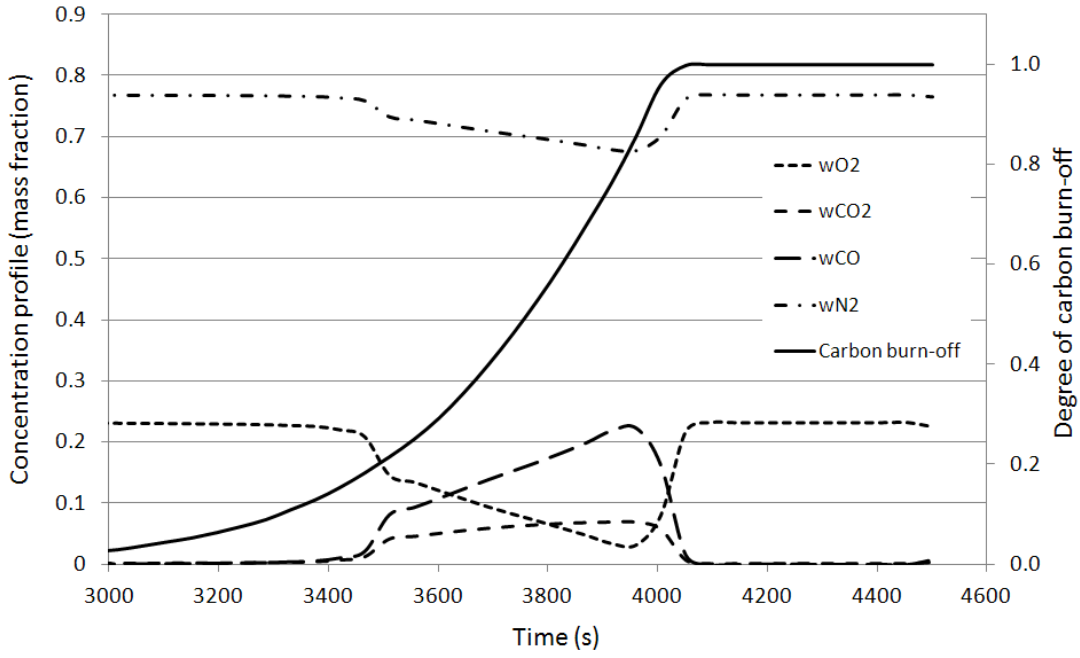

Figure 4-27 Mass concentration profiles of gas species at Point 1 expressed in mass fraction at centre of carbon layer during burn-off (12-layer LTCC / 0.15 mm carbon embedded structure).

(vii) Temperature profile

Temperature profile within the carbon layer at maximum carbon burn-off rate was obtained at Line 1 from the model for a 12-layer LTCC/0.15 mm carbon at 10 K/min heating rate, see Figure 4-28. The maximum temperature variation within the sample

was about 0.5 K. The slight increase in temperature of about 0.5 K above the firing profile temperature is not significant from a carbon burn-off perspective. However, this reveals the capability of the model in capturing the exothermic reaction effect of heating up the sample.

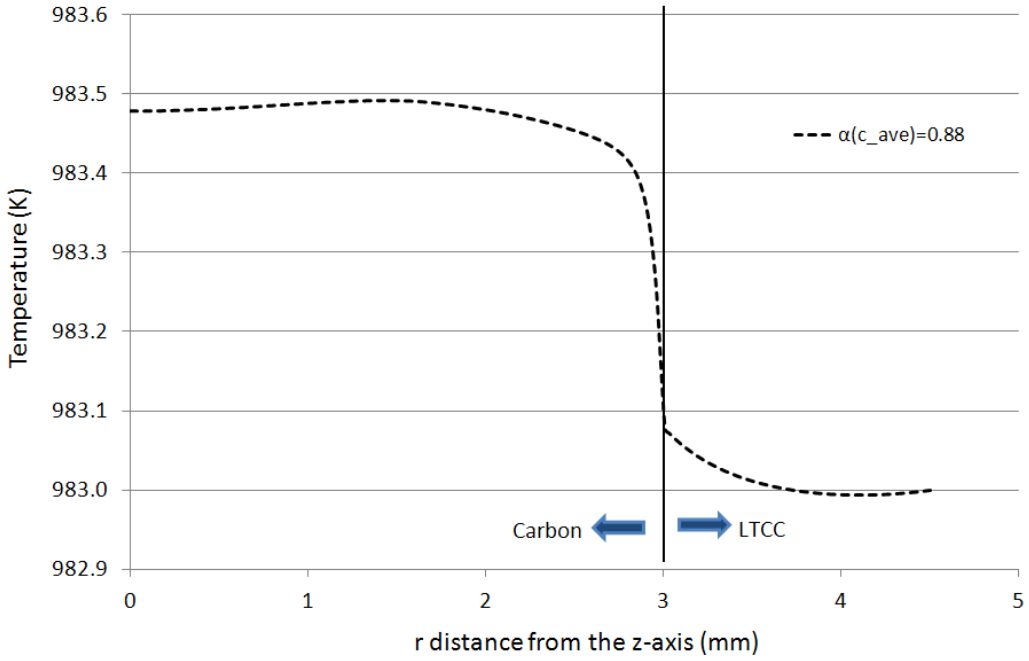

Figure 4-28 Temperature distribution along Line 1 for 12-layer LTCC/0.15 mm carbon at 10 K/min indicating maximum temperature deviation of 0.5 K at maximum burn-off rate.

(viii) Convective mass flux effect

Bulk flow for the system was governed by Darcy's pressure driven flow for porous medium. In all cases, mass transfer by diffusion was about an order higher than the mass transfer contributed by bulk flow. The maximum mass flux by bulk flow occurred at the maximum burn-off rate. The various mass flux components of O_2 at Point 1 of carbon tape are shown in Figure 4-29, indicating that the contribution by bulk flow of O_2 is very minimal. Thus, for model simplification, the effect of bulk flow may not be necessary be considered in the model.

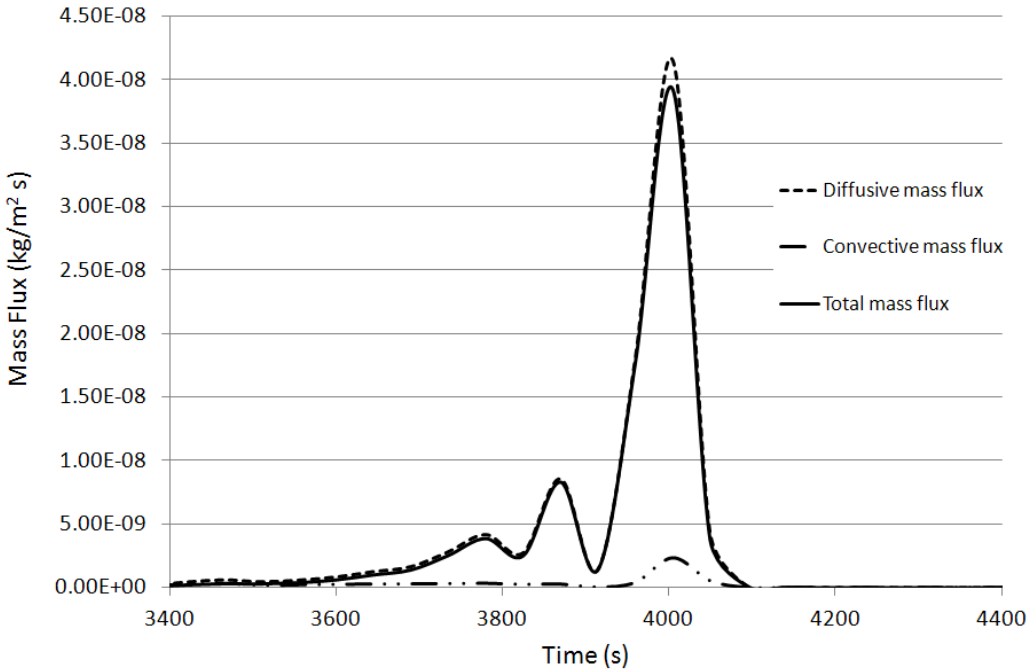

Figure 4-29 Mass flux profiles of O_2 at Point 1 of 12-layer LTCC/0.15 mm carbon at 10 K/min heating rate, indicating little contribution of mass flux from bulk flow (convective mass flux).

4.5 Concluding Remarks

Governing equations based on mass and heat transfer for multicomponent mixture was formulated together with the essential constitutive equations required for the modelling. Physical properties were determined experimentally or from empirical expressions which could be obtained from literature and handbooks. Those material properties not readily available were estimated from available data of similar materials.

The equations formulated will be employed for the simulation of carbon burn-off in embedded LTCC structures. It will be solved numerically for the embedded carbon burn-off process investigation and optimisation.

A process based 2D axisymmetrical model on the fabrication of simple cavity structure in LTCC using fugitive carbon was developed. Various embedded LTCC structure configurations with different combination of the number of carbon and LTCC layers were modelled and validated experimentally. Though the model predicted faster initial burn-off for thick carbon layer (0.25mm) at 5 K/min and 10 K/min heating rates, the difference between the burn-off curves at near burn-off completion ($[\alpha_C]_{ave} = 0.99$) were less than 5%. This presents sufficient accuracy for having the developed model for the simulation of carbon burn-off and LTCC sintering.

Other modelling results such as total gas pressure, reactant profile and temperature profile, which could not be validated experimentally, were also presented. These results provide a better understanding of the process and could be utilised for process optimisation or improvement.

In Chapter 5, this established model will be employed to demonstrate its potential in the optimisation of the LTCC sintering process to minimise cavity distortion (swelling or sagging) for a much larger sample dimensions which resemble some physical dimensions of devices for both RF electronics and MEMS applications.

Chapter 5

IMPLMENTATION OF PROCESS MODEL

Structural distortions such as cavity swelling and sagging were known to be the issue when dealing with large embedded structure. The internal pressure build-up due to carbon reaction and the gravitation effect of the suspended structure at the glass softening stage are closely related to the structure deformation [9]. Methods were developed by controlling of O_2/N_2 ratio in the sintering environment [28] or changing the carbon particle size in the carbon layer [146] in an effort to control the carbon burn-off rate during sintering. However, it will require additional gas control facility or source of carbon particles which may require reformulation of carbon paste or tape.

As such, the model developed in Chapter 4 is further validated in this chapter, in particular its capability for modelling typical practical geometries with large embedded structures, such as those contained in some of the applications in the areas of sensors, RF, microfluidic, microreactors and MEMS devices [8,140,141,142,143,144,145]. The LTCC sintering profile is to be optimised for the burn-off of carbon embedded in such a large embedded cavity.

As discussed in Chapter 4, total gas pressure was strongly coupled with heating rate. By applying low heating rate in the sintering profile, the pressure built-up can be lowered during carbon burn-off and at the same time delay the crystallisation of the LTCC. This will allow complete or near complete burn-off before the onset of softening of the LTCC system. In addition, carbon burn-off could be improved further by incorporating multiple isothermal steps. The advantage of using multiple-step firing

profile as compared to other methods is its ease of implementation. It can be achieved easily by re-programming the sintering furnace.

In this chapter, the developed process model for optimising the firing profile for an embedded cavity structure using multi-step firing profile will be demonstrated.

5.1 Experimental

The simple embedded cavity of ∅8 mm in the earlier experiment in Chapter 4 was scaled up to ∅32 mm. The construction of the sample is shown in Figure 5-1; it is a simple ∅32 mm circular cavity with a height of about 0.15 mm. This represents sufficient equivalent volume of space for housing multiple high performance RF, MEMS or microfluidic modules.

The fabrication of the samples was achieved with LTCC production equipment. The sample was built up primarily with self-constrained HL2000 tape. In addition, two other commercial tape systems, Dupont 951 and Ferro A6 LTCC tapes, were also employed for comparison. The LTCC tape was cut to size by CO_2 laser. Carbon tape of 0.15 mm (6 mil) thickness acted as the fugitive layer. The layers were stacked, aligned, pre-bonded and laminated. The sample was heated at 1 K/min constant heating rate from room temperature and debinded at 673 K for 2 hours. Preheating air blower integrated with the sintering furnace was used for better debinding. After debinding, the sample was subjected to the firing profile suggested by the developed process model. Temperature of the furnace was calibrated and controlled within 5 K. The temperature near the sample (5 mm above the sample top surface) was measured to be 20 K - 30 K higher than the furnace temperature settings depending on the range of

temperature used. As such, the sintering profile of the model was referred to this measured sample temperature, and compensated accordingly for programming the sintering furnace temperature.

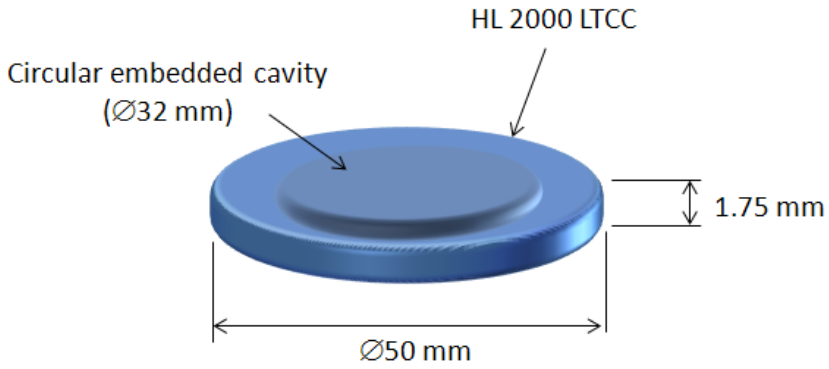

Figure 5-1 Sample construction before sintering.

5.2 Modelling

A 2D axisymmetric model was employed. The computation domain is shown in Figure 5-2. Instead of a TGA chamber, a full scale sintering furnace was employed here. Both the initial and boundary conditions were set exactly the same as the earlier model described in Chapter 4, Section 4.4.3. However, as the working space is now much larger than the TGA chamber, the boundary conditions might have to be appropriately adjusted for validation of the model. An attempt was made to optimise the firing profile to achieve the lowest internal pressure build-up in the cavity in the shortest processing time and within the operating specifications of the sintering furnace (maximum ramp rate is 10 K/min). For the purpose of process optimization, results achieved are targeted for comparisons.

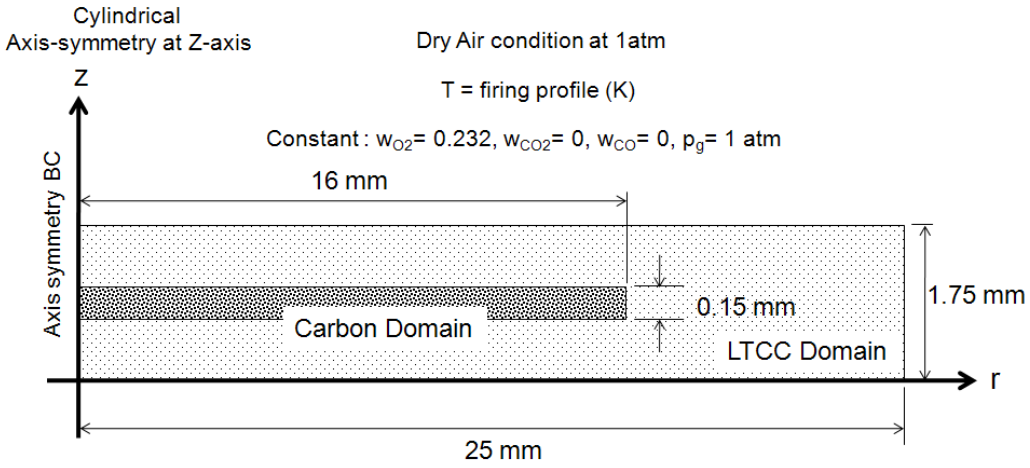

Figure 5-2 Computation domains for embedded structure with boundary conditions.

5.3 Optimisation of LTCC Sintering Profile

Optimisation was to be achieved by only adjusting the firing profile to achieve a fully embedded cavity with minimum sagging or swelling, and complete burn-off for the embedded carbon layer. The total gas phase generated during the carbon reaction and the LTCC sintering at the onset of pore closure due to viscous flow of glass components are considered by the process model for estimating the cavity deformation.

For optimisation, LTCC sintering is deliberately retarded for carbon burn-off to be completed just before the onset of glass flow to reduce cavity swelling due to the gas build-up pressure. However, it is important to maintain a certain level of gas pressure to prevent structure sagging due to gravitation effect of the suspended structure. Profiles selected have to take into consideration also sintering time required to minimise the production cycle. With the LTCC sintering curve, the relationship of pressure build-up is estimated at the centre point of the carbon layer where maximum pressure build-up occurred. This allows the determination of the pressure at the onset of glass softening point. The profile which produces the least pressure value at the onset point will be

selected. Simultaneously, the carbon burn-off curve is employed for the estimation of complete carbon burn-off.

Pressure build-up could be lowered by reducing the burn-off rate. Multiple steps of isothermal dwells will also delay LTCC sintering such that carbon burn-off could proceed smoothly. This will avoid premature complete sintering of LTCC, and thus the elimination of gaseous escape route before complete carbon burn-off. Based on the analysis of carbon burn-off rate, the operating temperature range of 823 K to 1048 K for multi-step profiling will be appropriate. Since constant heating rates within 5 K/min to 10 K/min are always recommended as standard LTCC sintering profiles, see Figure 5-3, profile optimisation employing the multiple step burn-off strategy will be explored on this basis through the developed process model.

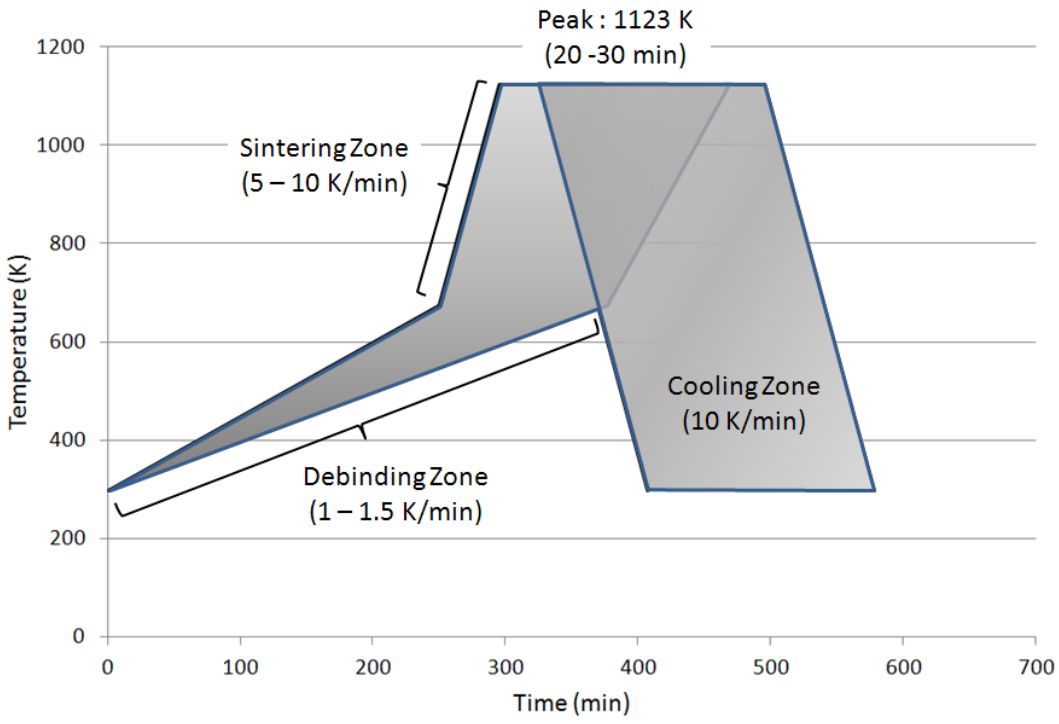

Figure 5-3 Recommended firing profiles for LTCC sintering.

The multiple steps firing profile related parameters are shown in Figure 5-4. A simple parametric study was generated as in Table 5-1. Carbon burn-off temperature was targeted at 898 K, 923 K, and 948 K, based on the TGA analysis. Due to HL2000 catalytic carbon burn-off at 898 K, a complete burn-off could be expected below 45 min, an accepted production rate. Below 898 K, burn-off could take much longer. Various constant heating rates of 2.5 K/min to a maximum heating rate of 10 K/min were used to heat up the sample from 673 K to the burn-off temperature with different soak times. The process model developed was utilised for the sintering zone.

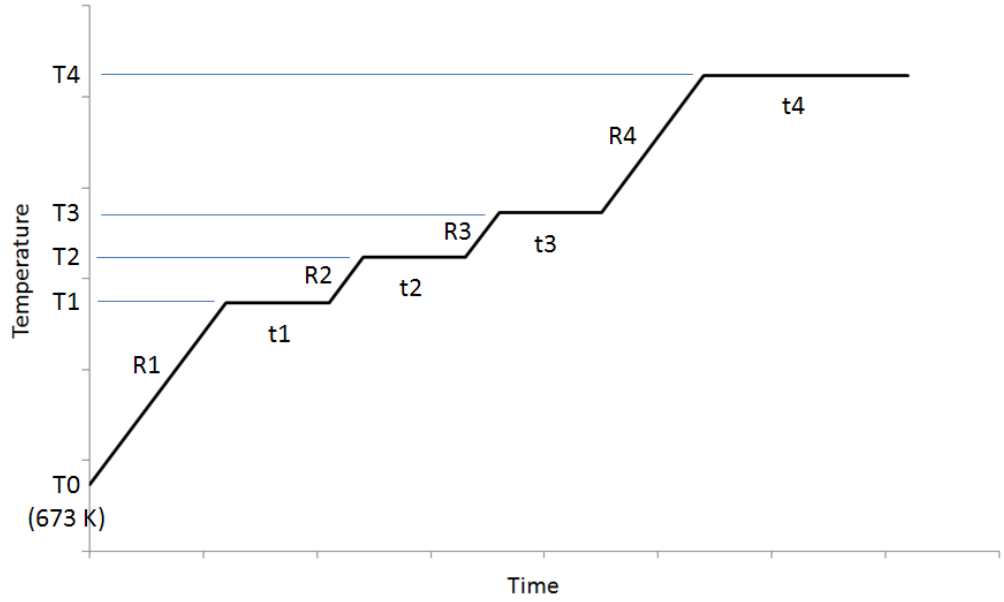

Figure 5-4 Firing profile parameters to be optimised for LTCC sintering.

Table 5-1 Firing profile parameters for optimisation modelling.

	Step 1			Step 2			Step 3			Step 4		
Run No.	R1 (K/min)	T1 (K)	t1 (min)	R2 (K/min)	T2 (K)	t2 (min)	R3 (K/min)	T3 (K)	t3 (min)	R4 (K/min)	T4 (K)	t4 (min)
1	5	1123	15									
2	10	1123	15									
3	10	923	15	10	1123	15						
4	10	923	30	10	1123	15						
5	10	948	15	10	1123	15						
6	10	848	0	2.5	923	15	10	1123	15			
7	10	873	0	2.5	923	15	10	1123	15			
8	10	898	15	5	923	15	10	1123	15			
9	10	923	15	10	948	5	10	1123	15			
10	10	898	5	10	923	10	10	948	5	10	1123	15

5.4 Results and Discussion

5.4.1 Burn-off Curves

The firing parameters selected as listed in Table 5-1 for the optimisation of firing profile for the embedded cavity structure were modelled using the developed process model. The results obtained for the carbon burn-off curves under fully embedded LTCC conditions are shown in Figure 5-5. All firing profiles shown in Figure 5-5 achieved complete burn-off. Thus the cavities fabricated should be free of carbon residue.

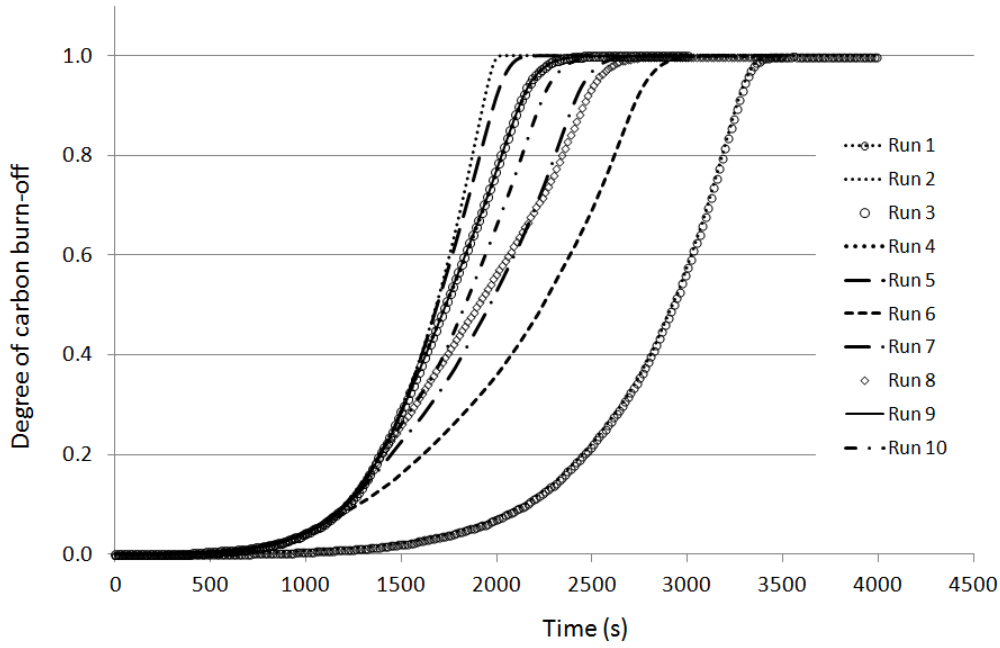

Figure 5-5 Embedded carbon burn-off curves obtained from the process modelling for the optimisation of firing profile runs.

5.4.2 Total Gas Pressure

The total gas pressure in the carbon layer was determined at the centre of the carbon layer (similar position as Point 1 of Figure 4-21 in Chapter 4) where the maximum pressure was occurring, along with the overall average degree of sintering of LTCC. The pressure plots for all the 10 runs are shown in Figure 5-6. In addition, the pressure values were estimated at the onset of softening of LTCC i.e. when LTCC becomes soften and swells with minimum pressure build-up in the cavity. The onset point was estimated at 2% of degree of LTCC sintering. The values of the total gas pressure are listed in Table 5-2.

Pressure build-up during the sintering process at Run 2 (10 K/min) was relative high at the onset of glass softening of 1.65 MPa. This pressure build-up in the embedded cavity could be reduced by having a multi-step firing profile typically from the range of 873 K – 923 K. For example, the multi-step sintering profile of Run 6 reduced the maximum

pressure build-up by as much as 38 % as compared to Run 2, see Figure 5-6. The combination of isothermal steps shown from the modelling calculation could suppress the pressure build-up, delay LTCC sintering, and result in lower pressure (near atmospheric pressure) before the onset of the glass softening. These would result in much less deformation to the cavity when competing kinetics of carbon burn-off and LTCC sintering occurred.

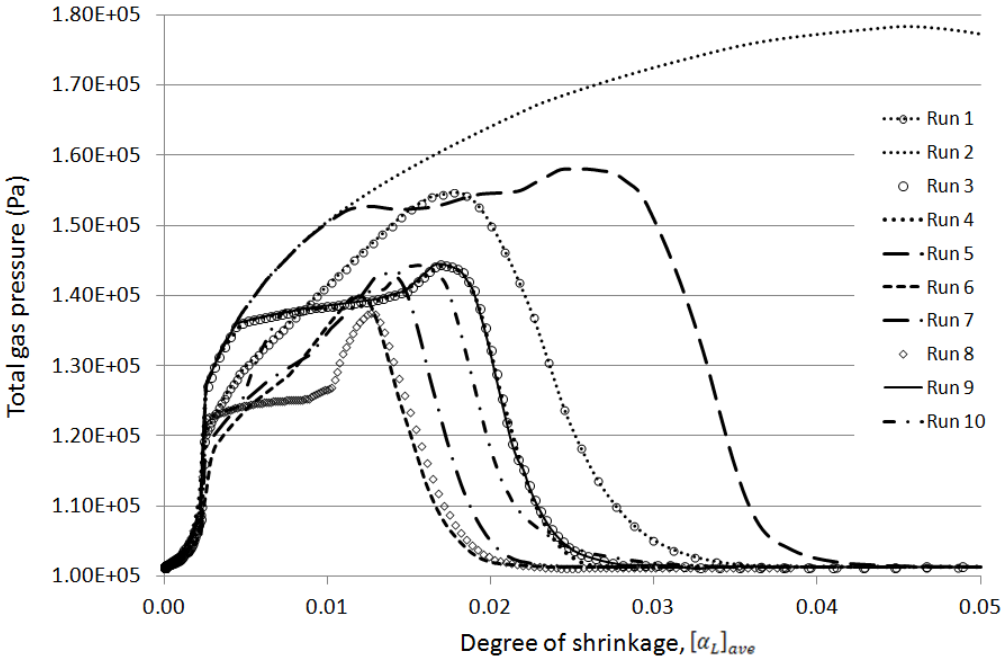

Figure 5-6 Modelling result plots of total gas pressure with degree of LTCC sintering.

Table 5-2 Modelling results based on total gas pressure in carbon layer at estimated onset point of substantial glass flow (pore closure). Run number with asterisk indicates selected optimised firing profile for actual sample testing.

Run No.	Total gas pressure at $[\alpha_L]_{ave}$ = 0.02, (Pa)
1	1.50×10^5
2	1.65×10^5
3	1.29×10^5
4	1.29×10^5
5	1.55×10^5
6*	1.02×10^5
7	1.05×10^5
8*	1.03×10^5
9	1.29×10^5
10	1.18×10^5

The two profiles with the lowest pressure values were selected for the actual sample runs, namely Runs 6 and 8. In addition to the sample fired at the 2 optimised firing profiles (Runs 6 and 8), samples fired at the standard profiles 5 K/min and 10 K/min were used for comparison. As shown in Figures 5-7 and 5-8, these samples (fired at 5 K/min and 10 K/min) had swelled cavity with cracks developed at the outer edge of the embedded cavity. Sample fired at 10 K/min showed severe cracking as shown in Figure 5-7. At 5 K/min, the cracks were only observed after cross-sectioning. This shows that a high heating rate could increase cavity swelling.

The quality of cavity formations was assessed by cross-sectioning. The cavity height of the cavity was measured across the diameter. The sample cross-sectioning images of the 5 K/min (Run 1), Run 6 and Run 8 are shown in Figures 5-8, 5-9 and 5-10 respectively. No cracks were observed on samples of Runs 6 and 8.

The result of the cavity measurements for maximum cavity height variation over the cavity diameter of 32 mm by cross-sectioning was compiled in Figure 5-11. Measurements were done on 3 samples each for Run 6 & Run 8. Sample fired at 10 K/min was excluded from measurement as it had obvious cracks. Samples fired at 5 K/min (Run 1) were employed as a reference for the optimised firing profiles. Using the 5 K/min standard profile, for a 32 mm diameter fully embedded cavity using 0.15 mm carbon tape, the average maximum cavity height variation was 2 mm. In contrast, with the multi-step firing profile (Run 6), an average maximum cavity height variation of 75 ± 41 μm was obtained, a significant improvement.

Figure 5-7 HL2000 embedded carbon sample after sintering at 10 K/min showing obvious cracks at edges of embedded cavity. No cross-sectioning was done as the defect is obvious.

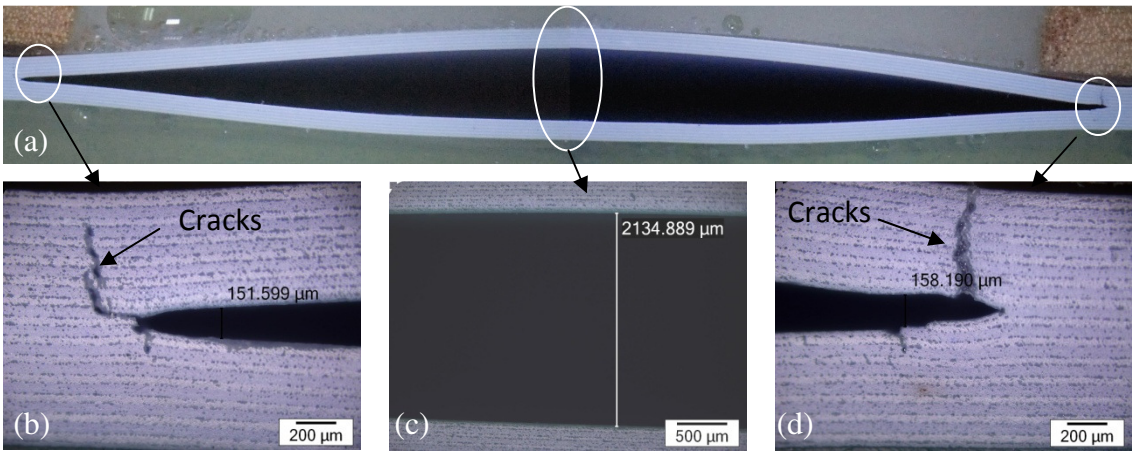

Figure 5-8 Sample cross-sectioning view of HL2000 embedded carbon sample after sintering at standard Run 1 (5 K/min) firing profile – (a) overall stitched images, (b) close-up left corner view, (c) close-up centre view, (d) close-up right corner view.

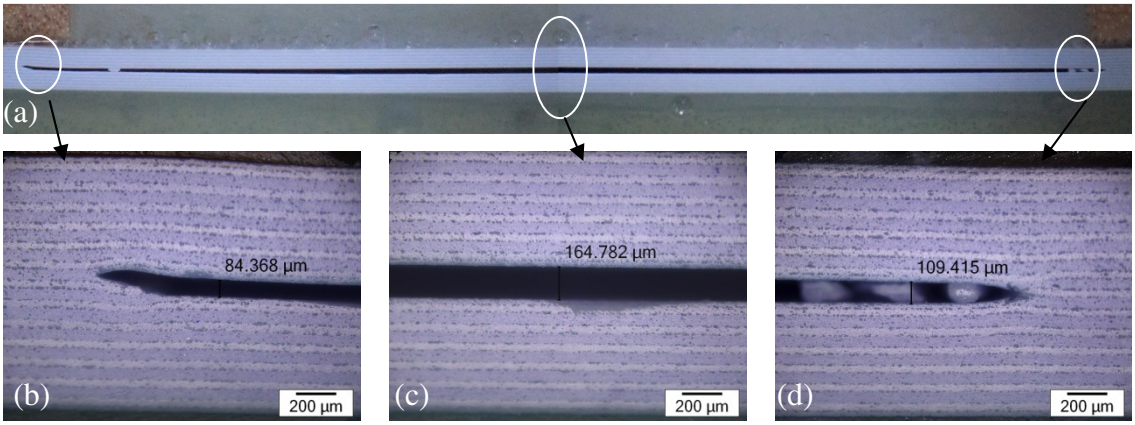

Figure 5-9 Sample cross-sectioning view of HL2000 embedded carbon sample after sintering at optimised firing profile of Run 6 – (a) overall stitched images, (b) close-up left corner view, (c) close-up centre view, (d) close-up right corner view.

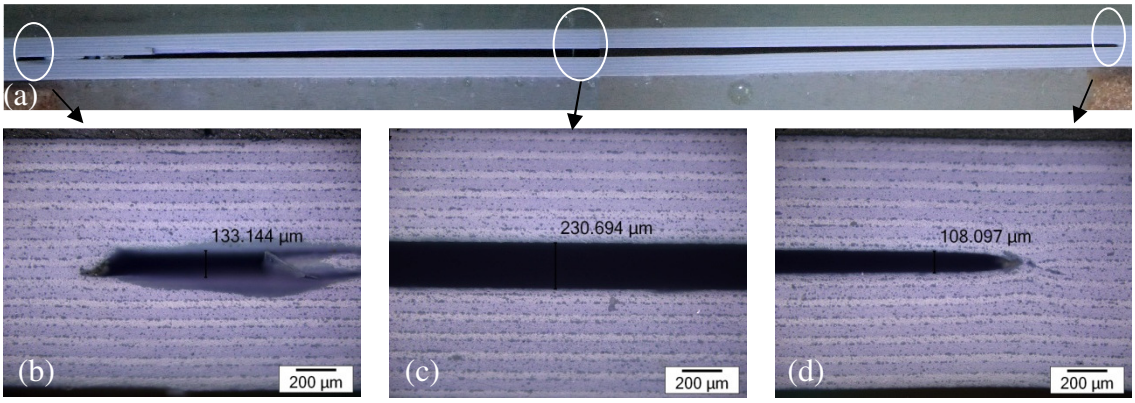

Figure 5-10 Sample cross-sectioning view of HL2000 embedded carbon sample after sintering at optimised firing profile of Run 8 – (a) overall stitched images, (b) close-up left corner view, (c) close-up centre view, (d) close-up right corner view.

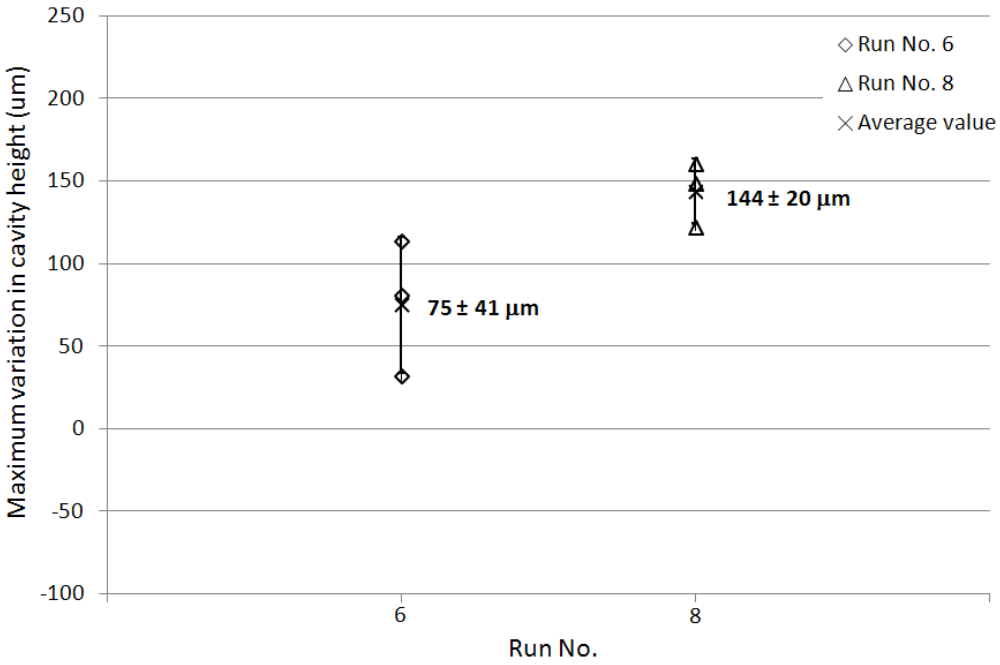

Figure 5-11 Cavity measurements of maximum variation of cavity height along cavity width of 32 mm.

5.4.3 Fracture Surface of Fired Samples

To assure the quality of the fired samples using the optimised firing profile with multiple steps of isothermal holds and slow ramp rates, the fired samples from Run 6 together with the standard profile 5 K/min were fractured and examined under Scanning Electron Microscope (SEM) at high magnifications. The SEM micrographs are shown in Figures 5-12 and 5-13. No "staircase" liked fractured surface was observed for both samples indicating that the layers were well laminated and inter-fused after sintering as one monolithic body. The LTCC layers for both samples were fully sintered and shown clean normal brittle fracture (glass liked fracture) with tiny voids of size in micro range populated evenly in the LTCC layers. A higher void density at the interface between the LTCC and constrained layer was observed. The interfacial voiding was always observed when dissimilar layers (LTCC and refractory constrained layers) were integrated. The fracture surfaces for both samples at 5 K/min

and multi-step profile (Run 6) show no significant micro-structurally difference. Thus, the optimised firing profile with multiple isothermal hold and ramp was not significantly affecting the sintering property of the LTCC structure.

Furthermore, the optimised sintering profile (Run 6) achieved less distorted samples with no loss in sintering time. The total sintering time, as shown in Figure 5-14, excluding the debinding and cooling cycles, is quite comparable with the recommended standard sintering at a constant heating rate of 5 K/min.

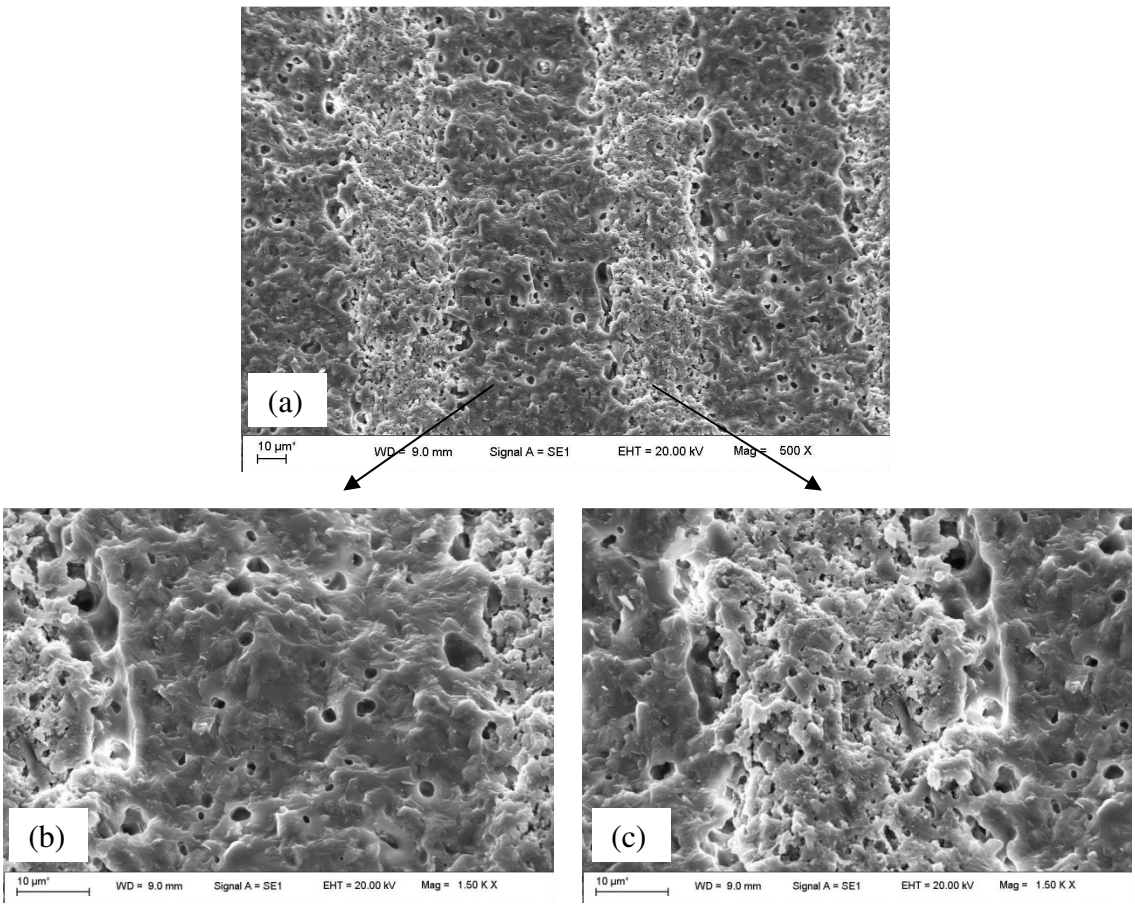

Figure 5-12 Fired at standard 5 K/min profile, fracture surface of fired HL2000 carbon embedded structured sample taken by SEM micrographs showing a) unique layered self constrained layer structure, b) LTCC layer and c) constrained refractory layers.

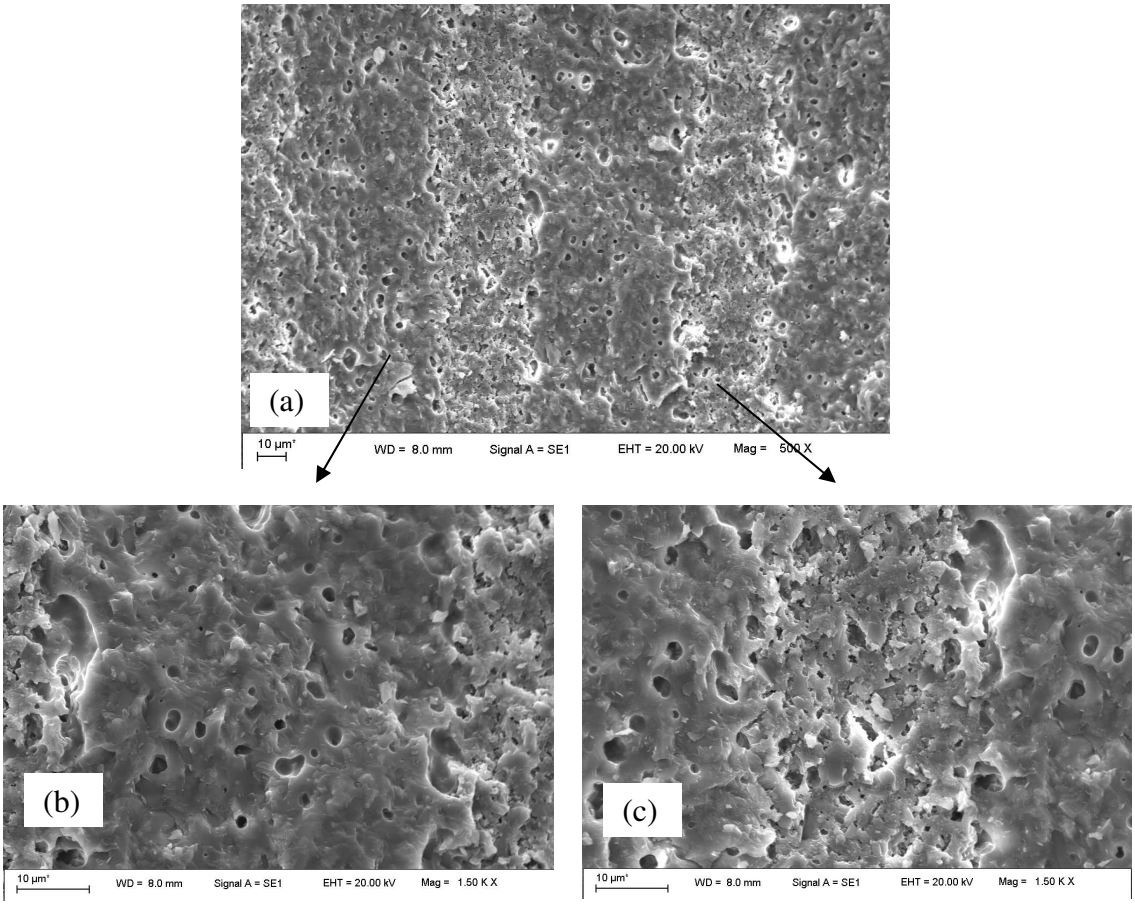

Figure 5-13 Fired at optimised Run No 6 firing profile, fracture surface of fired HL2000 carbon embedded structured sample taken by SEM micrographs showing a) unique layered self constrained layer structure, b) LTCC layer and c) constrained refractory layers.

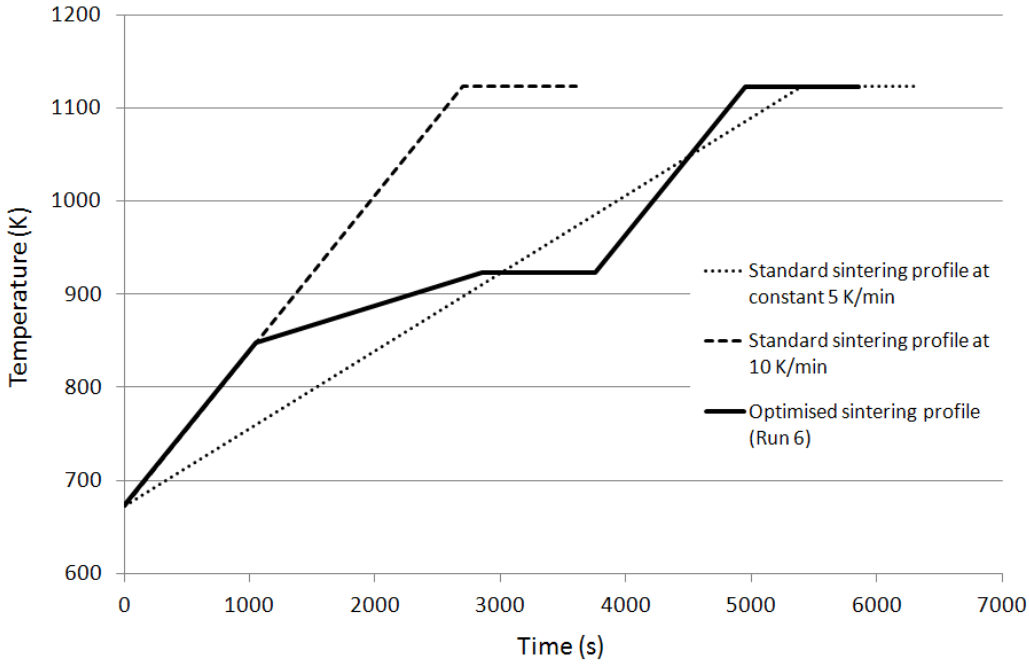

Figure 5-14 Optimised sintering profile excluding debinding cycle and cooling cycles of Run 6 with multi-step isothermal dwell and slow ramp rate.

5.4.4 Other LTCC Materials

The same approach was applied to other common commercial LTCC systems such as Dupont 951 and Ferro A6M. The sample configuration remains the same as that for HL2000. However, as the LTCC tape systems of Dupont 951 and Ferro A6M are not self constrained, these samples after sintering will experience shrinkage of 8 – 20 % in all directions. The cavity dimension is expected to shrink to approximately ∅26 mm after sintering due to the inherent shrinkage property.

The samples tested on Dupont showed minimal swelling or sagging of cavity which is comparable to HL2000, see Figure 5-15. For Ferro A6M, as it retarded the carbon burn-off by almost 20 %, it requires a much longer hold time that may not be favourable for sintering. The fired samples for Ferro A6M are shown in Figure 5-16, and the results obtained are not encouraging. Indeed, to achieve Ferro embedded

structure, one may have to consider combining Ferro A6M with other LTCC system that could catalyse the carbon burn-off, for example Dupont 951. By integrating a layer of Dupont 951 over the embedded carbon layer, the result of using multiple step sintering profile is significantly improved, with the fired sample having minimum deformation as shown in Figure 5-17. However, both LTCC systems have to be matched with respect to the sintering shrinkage to avoid severe cracking or distortion due to differential sintering stress.

Figure 5-15 Dupont 951 embedded samples sintered at a) standard firing profile 10 K/min, b) standard firing profile at 5 K/min, c) multi-step firing profile.

Figure 5-16 Ferro A6M embedded samples sintered at a) standard firing profile 10 K/min, b) standard firing profile at 5 K/min, c) multi-step firing profile.

Figure 5-17 Embedded sample of composite layer of Ferro A6M/Dupont 951 firing at multi-step profile.

5.5 Concluding Remarks

The process model developed was successfully applied for the optimisation of sintering profile for a fully embedded cavity structure using fugitive carbon layer. On HL2000 LTCC system, with the assistance of process modelling, multi-step firing profile with steps of isothermal dwells and slow ramp rate steps was demonstrated to reduce pressure build-up. Physical samples demonstrated that minimum cavity swelling and sagging can be achieved. A relatively flat fully embedded cavity with an average maximum cavity height variation of just 75 ± 41 μm over a span of 32 mm is possible. The same optimisation approach could also be applied to other LTCC embedded systems such as Dupont and Ferro with comparable results.

Chapter 6

CONCLUSIONS AND FUTURE WORK

6.1 Conclusions

Every process model is unique to its specific process requirements. In this investigation, a model was proposed, formulated and implemented for the modelling of embedded carbon burn-off in LTCC for embedded structure fabrication. This was achieved by implementing mass transport equations to two computation domains of carbon and LTCC layers coupled with carbon burn-off and sintering reaction models.

The process based 2D axisymmetry model on a fabrication of a simple cavity structure in LTCC using fugitive carbon was successfully developed and first validated experimentally in TGA environment. Though the model predicted faster initial burn-off for a thick carbon layer at low heating rates, the differences between the predicted and experimentally observed burn-off curves at near burn-off completion ($[\alpha_C]_{ave} = 0.99$) were less than 5%. This is a notable achievement as it paves the way for the optimisation of processing conditions for carbon burn-off and LTCC sintering through simulation.

Solid catalysed reaction was revealed in embedded carbon burn off in LTCC which hitherto has not been reported. The carbon kinetic analysis conducted showed carbon burn-off rate was significantly affected by the intimate contact of inorganic metal oxides contained in LTCC. Among the tested LTCCs, Dupont 951 is a strong catalyst followed by HL2000, while Ferro A6M inhibits the carbon burn-off. Isoconversion method fitted with a first order reaction model for variable activation energy and pre-

exponential factor was shown to be a good estimation method with sufficient accuracy for embedded carbon burn-off kinetic analysis.

The kinetic parameters for HL2000 sintering were determined based on solid-state first order reaction model. A single value activation energy and pre-exponential factor determined by linear regression over multiple heating rates from different LTCC configurations proved to be appropriate for the sintering of different layer configurations of LTCC in spite of the complex sintering mechanisms which involve viscous flow. This adopted method also avoids the ambiguity on the reaction rate parameters resulted from the single non-isothermal analysis at different constant heating rates. In addition, this mathematically simple model could be easily integrated into the process model.

The process model developed, which was first validated in laboratory scale (TGA environment), was subsequently demonstrated to be equally applicable for the optimisation of sintering profile for a fully embedded cavity structure using fugitive carbon layer in production scale. Using a furnace, a large embedded cavity was fabricated using HL2000 LTCC system with fugitive carbon. With the assistance of process modelling, multi-step firing profile with steps of isothermal dwells and slow ramp rate steps was demonstrated to reduce pressure build-up and thus resulted minimal swelling and sagging of the cavity. A near free distortion fully embedded cavity with average maximum cavity height variation of just 75 ± 41 μm over a span of 32 mm was achieved. The same optimisation approach was also demonstrated on other LTCC embedded systems such as Dupont and Ferro with comparable results.

The successful development of the process model will greatly reduce the time required on process trials for process troubleshooting, improvement and also for new products introduction. The process model will provide a better understanding of the competing effects of various processing parameters in the fabrication of LTCC embedded structures. It could be used as a reference model for process improvement and optimisation. The approach and model developed could well be extended to other processes involving the burn off of embedded fugitive components.

6.2 Future Work

A simple carbon burn-off could be complex when embedded in different LTCC systems. The carbon burn-off could be catalysed or inhibited. The mechanism of carbon burn-off could be further complicated when the carbon surface has intimate contact with the LTCC. In this study, a simple homogeneous volume reaction was considered for burn-off which could be appropriate when the carbon layer is relatively thin. Though the catalytic reaction is occurring at the surface, it is of sufficient accuracy to assume that the reaction is uniformly throughout the whole carbon layer for a thin carbon layer. When the carbon layer becomes thicker, the reaction mechanism may be different as the interaction of surface catalytic reaction at LTCC/carbon interface and non-catalytic carbon reaction will be dominant as the reaction proceeds into the depth of the layer. A more thorough understanding of the solid catalysed carbon burn-off mechanism with possible internal oxidation by close contact of metal oxides is necessary. An improved model could be anticipated which could capture the expected deceased reactivity profile away from the surface of the carbon layer. The "break-off" point as mentioned in Chapter 4 has to be physically determined and theoretically modelled. A shrinking grain model of reducing external size with reaction

may be applicable. A mixture of homogeneous volume reaction model and heterogeneous shrinking grain reaction model will be more realistic to describe the carbon burn-off if a thick carbon layer is involved.

LTCC pore or porosity model was presently estimated from the combined TGA and TMA curves. For better estimation, more rigorous and systematic approach could be employed. Detailed microstructure and pore measurement for pore evolution during the course of sintering in different sintering environment could be performed. The challenges are to measure the pore change during the sintering especially at the instant of the onset of glass flow for viscous sintering. A good estimation translates to a better and more accurate model for LTCC sintering. This will be an added advantage for predicting the interesting competing kinetics of carbon burn-off and pore closure during LTCC sintering. This will provide a more accurate prediction for any incomplete burn-off or when the application required tailored amount of carbon burn-off or carbon residue to be trapped. LTCC thickness effect could also be included in the present model, for the effect on the porosity and pore formation.

To extend the scope of the applicability of the model, a stress/strain model could be included for the prediction of the deformation of the cavity structure i.e. sagging/swelling of the cavity structure. This will be particularly useful for the prediction of the probability of cracking of the structure as observed in Figure 5-8 in Chapter 5. To achieve this, other physical in-situ measurements of material mechanical properties essential for deformation predictions such as Young modules at various degree of LTCC sintering will be required.

LTCC sintering shrinkage is known to be large. For example, self-constrained tape HL2000 has a Z-axis shrinkage of more than 30 %. The cavity volume containing fugitive carbon is the burn-off reaction volume, which shrinks progressively during sintering. This effect is considered second order and has not been considered in the present study. However, for a large embedded cavity, the shrinking reaction volume may have some effect in the pressure build-up in the cavity. Shrinkage of LTCC interacting with carbon burn-off could induce structural change. This could be an interesting area of research to investigate if it could be exploited for controlling the deformation of the cavity formed.

Last but not least, the model could be extended from axisymmetric modelling to full 3D modelling for complex 3D structures.

REFERENCES

1. Y Imanaka, “Multilayered Low Temperature Cofired Ceramics (LTCC) Technology”, Springer Science Inc, 2005.

2. R M German, “Liquid phase sintering”, Plenum Press, 1985.

3. R R Tummala, “Ceramic and glass-ceramics packaging in the 1990s”, Journal of American Ceramics Society, 74, 5, 895-908, 1991.

4. P W McMillan, “Glass-Ceramics”, Second Printing, Academic Press Inc, 1969.

5. D L Wilcox, S J W Burdon, R Changrani, C F Chou, S Dai, R Koripella, M Oliver, D Sadler, P V Allmen, F Zenhausern, “Add ceramic “MEMS to the pallet of Microsystems technologies”, Material and Research Society Symposium Proceeding, Volume 687, B7.1.1-B7.1.18, 2001.

6. I G Nuria, M C S Cynthia, F Valdes, J Alonsa, “Green-tape ceramics. New technological approach for integrating electronics and fluidics in microsystems”, Trends in Analytical Chemistry, 27, 1, 24-33, 2008.

7. M R Gongora-Rubio, P Espinoza-Vallejos, L Sola-Laguna, J J Santiago-Aviles, “Overview of low temperature co-fired ceramics tape technology for meso-system technology (MsST)”, Sensors and Actuators A, 89, 222-241, 2001.

8. K A Peterson, R T Kundson, E J Garcia, K D Patel, M Okandan, C K Ho, C D James, B R Rohrer, F Smith, L R Zawicki, B D Wroblewski, “LTCC in microelectronics, Microsystems, and sensors”, 15th International Conference of Mixed Design, MIXDEC 2008, 23-37, 2008.

9. H H Bau, S G K Ananthasuresh., J J Santiago-Aviles, J Zhong, M Kim, M Yi, P Espinoza-Vallejos, L Sola-Laguna, “Ceramic tape based meso systems technology”,

Proceedings of the ASME International Mechanical Engineering Congress and Exposition, 491-498, 1988.

10. R K Yamamoto, M R Gongora-Rubio, R S Pessoa, M R Cunha, H S Maciel, "Mixed LTCC and LTTT technology for microplasma generator fabrication", Journal of Microelectronics and Electronic Packaging, 6, 1-7, 2009.

11. J Youngsman, B Marx, M Schimpf, S Wolter, J Glass, A Moll, "Low Temperature Co-fired Ceramics for Micro-Fluidics", Proceedings 56th Electronic Components and Technology Conference, 699-704, 2006.

12. Y C Lee, C S Park, "LTCC stripline resonator using embedded air cavity for millimeter wave applications", Microwave and Optical Technology Letters, 50(3), 658 – 661, 2008.

13. M E Richard, "Tape casting: theory and practice", American Ceramic Society, 2000.

14. G Natarajan, J N Humenik, "3D ceramics microfluidic device manufacturing", Journal of Physics: Conference Series 34, 533-539, 2006.

15. T Rabe, W A Schiller, T Hochheimer, C Modes, A Kipka, "Zero shrinkage of LTCC by self-constrained sintering", International Journal of Applied Ceramic Technology", 2(5), 374-382, 2005.

16. C R Needes, M F Barker, P T Ollivier, K W hang, K F Souders, C B Wang, M A Smith, "Constrained-sintered, low temperature co-fired ceramics for IC packaging applications", Proceedings 53rd Electronic Components and Technology Conference, 30-35, 2003.

17. K R Mikeska, D T Schaefer, "Method for reducing shrinkage during firing of ceramic bodies", U S Patent, 5,474,741, 1995.

18. F P Lautzenhiser, E M Amaya, J T Hochheimer, “Methods for making and using self-constrained low temperature glass-ceramic unfired tape for microelectronics”, U S Patent, 6,949,156 B2, 2005.

19. II K Kim, N Kidera, S Oinel, J Papapolymerou, J Laskar, J G Yook, M M Tentzeris, “Linear tapered cavity-backed slot antenna for millimetre-wave LTCC modules”, IEEE Antennas and Wireless Propagation Letters, 5, 175-178, 2006.

20. Y C Lee, “CPW-to-Stripline vertical via transitions for 60GHz LTCC SOP applications”, Progress in Electromagnetics Research Letters, 2 37-44, 2008.

21. M A Piwonski, A Roosen, “Low pressure lamination of ceramic green tapes by gluing at room temperature”, Journal of the European Society, 19, 263-270, 1999.

22. J W Burdon, R F Huang, D Wilcox, N J Naclerio, “Method for fabricating a multilayered structure and the structures formed by the method”, U.S Patent, 6,592,696 B1, 2003.

23. A Roosen, “New lamination technique to join ceramic green tapes for the manufacturing of multilayer devices”, Journal of the European Ceramics Society, 21, 1993-1996, 2001.

24. K. Karthikeyan, S K Chou, L E Khoong, Y M Tan, C W Lu, W M Yang, “Low temperature co-fired ceramic vaporizing liquid microthruster for microspacecraft applications”, Applied Energy, 97, 577-583, 2012.

25. R L Wahlers, S J Stein, M A Stein, A H Feingold, P W Bless, “Ceramics tapes for wireless applications”, Presented at Annual Meeting of American Ceramic Society, 2000, Cincinnati.

26. R Bauer, M Luniak, L Rebenklau, K J Wolter, W Sauer, “Realization of LTCC-Multilayer with special cavity applications”, Proceedings 30th International Symposium on Microelectronics, ISHM, 659-664, 1997.

27. C W Berry, A E Bailey, “Method of laminating low temperature co-fired ceramics (LTCC) materials”, U.S Patent, 7,240,424 B2, 10 July 2007.

28. P Epsinoza-Vallejos, J H Zhong, M R Gongora-Rubio, L Sola-laguna, J J Santiago-Aviles, “Meso (Intermediate)-scale electromechanical systems for the measurement and control of sagging in LTCC structures”, Materials Research Society Symposium Proceedings, 518, 3-79, 1998.

29. K A Peterson, K D Patel, C K Ho, C D Nordquist, C A Walker, B D Wroblewski, M Okandan, “Novel Microsystem Applications with new techniques in low-temperature co-fired ceramics”, International Journal of Applied Ceramic Technology, 2, 345-363, 2005.

30. J H Alexander, “Method of making ceramic article with cavity using LTCC tape”, U.S Patent, 5,601,673, 1997.

31. J I Kuo, S J Da, S S Jen, “Lamination process of packaging substrate”, U.S Patent Application Publication, US2004/0108058 A1, 2004.

32. J D Cawley, A H Heuer, W S Newman, “Methods for constructing three dimensional bodies from laminations”, U.S Patent, 5,779,833, 1998.

33. B R Smith, R T Pike, M Newton, “Embedded hermetic cavity formation in low temperature cofired ceramic”, U.S Patent, 6,733,607 B2, 2004.

34. H Birol, T Maeder, P Ryser, “Application of graphite-based sacrificial layers for fabrications of LTCC (Low temperature co-fired ceramic) membranes and microchannels”, Journal of Micromechanics and Microengineering, 17, 50-60, 2007.

35. J Szekely, J W Evans, H Y Sohn, “Gas-solid reactions”, Academic press. 1976.

36. S Yagi, D Kunii, “Studies on combustion of carbon particles in flames and fluidized beds”, Symposium (International) on Combustion, 5(1), 231-244, 1955.

37. C Y Wen, “Noncatalytic heterogeneous solid fluid reaction models”, Industrial and Engineering Chemistry, 60(9), 34 – 54, 1968.

38. E W Thiele, “Relation between catalytic activity and size of particle”, industrial Engineering & Chemistry”, 31(7), 916-920, 1939.

39. J Szekely, J W Evans, “A structural model for gas-solid reactions with moving boundary”, Chemical Engineering Science, 25, 1091-1107, 1970.

40. J Szekely, J W Evans, “A structural model for gas-solid reactions with moving boundary II – The effect of grain size, porosity and temperature on the reaction of porous pellets”, Chemical Engineering Science, 26, 1901-1913, 1971.

41. A B M Heesink, W Prins, W P M Van Swaaij, “A grain size distribution model for non-catalytic gas-solid reactions”, The Chemical Engineering Journal, 53, 25-37, 1993.

42. P V Ranade, D P Harrison, “The grain model applied to porous solids with varying structural properties”, Chemical Engineering Science, 34, 427-432, 1979.

43. S Stendardo, P U Foscolo, “Carbon dioxide capture with dolomite: A model for gas-solid reaction within the grains of a particulate sorbent”, Chemical Engineering Science, 64(10), 2343-2352, 2009.

44. E E Petersen, “Reaction of porous solids”, AIChE, 3(4), 443-448, 1957.

45. S K Bhatia, D D Perlmutter, ”A random pore model for fluid-solid reaction: I Isothermal, kinetic control”, AIChE, 26(3), 379-386, 1980.

46. S K Bhatia, D D Perlmutter, ”A random pore model for fluid-solid reaction: II Diffusion and transport effects”, AIChE, 27(2), 247-254, 1981.

47. M Avrami, “Kinetics of phase change. I General theory”, Journal of Chemical Physics, 7, 1103-1112, 1939.

48. C R Clarkson, R M Bustin, “The effect of pore structure and gas pressure upon the transport properties of coal: a laboratory and modelling study. I Isotherms and pore volume distributions”, Fuel, 78, 1333-1344, 1999.

49. P Ghetti, U D Robertis, S D’Antone, M Villani, E Chiellini, “Coal combustion, correction between surface area and thermogravimetric analysis data”, Fuel, 64, 950-955, 1985.

50. A R Kerstein, B F Edwards, “Percolation model for simulation of char oxidation and fragmentation time-histories”, Chemical Engineering Science, 42(7), 1629-1634, 1987.

51. M Sahimi, T T Tsotsis, “Statistical modeling of gas-solid reaction with pore volume growth: Kinetic regime”, Chemical Engineering Science, 43(1), 113-121, 1988.

52. F Y Wang, S K Bhatia, “A generalised dynamic model for char particle gasification with structure evolution and peripheral fragmentation”, Chemical Engineering Science, 56, 3683-3697, 2001.

53. B Feng, S K Bhatia, “Percolative fragmentation of char particles during gasification”, Energy & Fuels, 14, 297-307, 2000.

54. P B Weisz, R D Goodwin, “Combustion of carbonaceous deposits within porous catalyst particles I. Diffusion-controlled kinetics”, Journal of Catalysis, 2, 397-404, 1963.

55. P L Walker, F Rusinko, L G Austin, “Gas reactions of Carbon”, Advances in Catalysis, V11, 133-221, 1959.

56. P A Ramachandran, M P Dudukovic, “Reactions of solid particles with nonuniform distribution of solid reactant – The volume reaction model”, Chemical Engineering Science, 39(4), 669-680, 1984.

57. P L Walker, M Shelef, R A Anderson, “Catalysis of carbon gasification”, Chemistry and Physics of Carbon, 4, 287-383, 1968.

58. D W Mckee, “Metal oxides as catalysts for the oxidation of graphite”, Carbon, 8, 623-635, 1970.

59. J P A Neeft, M Makkee and J A Moulijn, “Catalytic oxidation of carbon black – I. Activity of catalysts and classification of oxidation profiles”, Fuel, 77(3), 111-119, 1998.

60. C R Maier, L E Jones, “The Influence of aluminum phosphates on graphite Oxidation”, Carbon, 43, 2272-2276, 2005.

61. P A Ramachandran, L K Doraiswamy, “Modeling of noncatalytic gas-solid reactions”, AIChE, 28(6), 881-900, 1982.

62. H H Lee, “Effectiveness factors for solid-catalyzed gas-solid reactions”, Chemical Engineering Science, 34, 5-9, 1979.

63. G L Guzman, E E Wolf, “Effect of nonuniform activity distribution on catalyzed gas-solid reactions”, Industrial Engineering & Chemistry Fundamentals, 18(1), 7-11, 1979.

64. N M Laurendeau, “Heterogeneous kinetics of coal char gasification and combustion”, Progress in Energy Combustion Science, 4, 221-270, 1978.

65. J E Hustad, D Vareide, O K Sonju, “Burning rates of coke particles in the freeboard above a fluidized bed reactor”, Combustion and Flame, 85, 232-240, 1991.

66. J Ballester, S Jimenez, “Kinetic parameters for the oxidation of pulverized coal as measured from drop tube tests”, Combustion and Flame, 142, 210-222, 2005.

67. R C Everson, H W J P Neomagus, D Njapha, “Kinetic analysis of non-isothermal thermogravimetric analyser results using a new method for the evaluation of the temperature integral and multi-heating rates”, Fuel, 85, 418-422, 2006.

68. M M Patel, D T Grow, B C Young, “Combustion rates of lignite char by TGA”, Fuel, 67, 165-169, 1988.

69. M A Serageldin, W P Pan, “Coal: Kinetic analysis of thermogravimetric data”, Thermochimica Acta, 71, 1-14, 1983.

70. A G Barea, P Ollero, R Arjona, “Reaction-diffusion model of TGA gasification experiments for estimating diffusional effects”, Fuel, 84, 1695-1704, 2005.

71. I W Smith, “The combustion rates of coals chars: A review”, 19th Symposium (International) on Combustion, The Combustion Institute, 1045-1065, 1982.

72. B Feng, S K Bhatia, “On the validity of thermogravimetric determination of carbon gasification kinetics”, Chemical Engineering Science, 57, 2907-2920, 2002.

73. A Jess, A Andresen, “Influence of mass transfer on thermogravimetric analysis of combustion and gasification reactivity of coke”, Fuel, 89, 1541-1548, 2010.

74. W Holand, G Beall, “Glass-ceramic technology”, The American Ceramic Society, 2002.

75. W D Kingery, “Densification during sintering in the presence of a liquid phase. I. Theory”, Journal of Applied Physics, 30(3), 301-306, 1959.

76. W D Kingery, M D Narasimhan, “Densification during sintering in the presence of a liquid phase. II. Experimental”, Journal of Applied Physics, 30(3), 307-310, 1959.

77. S M Lee, S J Kang, “Theoretical analysis of liquid-phase sintering: Pore filling theory”, Acta mater, 46(9) 3191-3202, 1998.

78. S J L Kang, “Sintering – Densification, grain growth & microstructure”, Elsevier Butterworth-Heinemann, 2005.

79. K G Ewsuk, “Sintering maps for ceramic-filled-glass composites”, International Ceramic Science and Technology Congress Symposium on Glass for Electronic Applications, Orlando USA, 1990.

80. S Kemethmuller, M Hagymasi, A Stiegelschmitt, A Roosen, “Viscous flow as the driving force for the densification of low-temperature co-fired ceramics”, Journal of American Ceramic Society, 90(1), 64-70, 2007.

81. S X Dai, R F Huang, D L Wilcox, “Use of titanates to achieve a temperature-stable loe-temperature cofired ceramic dielectric for wireless applications”, Journal of American Ceramic Society, 85(4), 828-832, 2002.

82. H Su, D L Johnson, “Master sintering curve: A practical approach to sintering”, Journal of American Ceramic Society, 79(12), 3211-3217, 1996.

83. J D Hansen, R P Rusin, M H Teng, D L Johnson, “Combined-stage sintering model”, Journal of American Ceramic Society, 75(5), 1129-1135, 1992.

84. A Mohanram, G L Messing, D J Green, “Densification and sintering viscosity of low-temperature co-fired ceramics”, Journal of American Ceramic Society, 88(10), 2681-2689, 2005.

85. J Opfermann, J Blumm, W D Emmerich, “Simulation of the sintering behavior of a ceramic green body using advanced thermokinetic analysis”, Thermochimica Acta, 318, 213-220, 1998.

86. A C Muller, J R Opfermann, E I Tiffee, ”Modelling and optimization of solid electrolyte sintering behavior by thermokinetic analysis”, Thermochimica Acta, 414, 11-17, 2004.

87. A F Mills, “Mass Transfer”, Prentice Hall, 2001.

88. J Bear, Y Bachmat, “Introduction to modeling of transport phenomena in porous media”, Kluwer Academic Publishers, 1991.

89. S Whitaker, “Diffusion and dispersion in porous media”, AIChE Journal, 13(3), 420-427, 1967.

90. W G Gray, “A derivation of the equations for multi-phase transport”, Chemical Engineering Science, 30, 229-233, 1975.

91. J M Nordbotten, M A Celia, H K Dahle, S M Hassanizadeh, “On the definition of macroscale pressure for multiphase flow in porous media”, Water Resources Research, 44, W06S02, 2008

92. J Hager, S Whitaker, “The thermodynamic significance of the local volume averaged temperature”, Transport in Porous Media, 46, 19-35, 2002.

93. S Korteland, S Bottero, S M Hassanizadeh, C W J Berentsen, “What is the correct definition of average pressure ?”, Transport in Porous Media, 84, 153-175, 2010.

94. W G Gray, C T Miller, “Thermodynamically constrained averaging theory approach for modelling flow and transport phenomena in porous medium systems: I. Motivation and overview”, Advances in Water Resources, 28, 161-180, 2005.

95. C T Miller, W G Gray, “Thermodynamically constrained averaging theory approach for modelling flow and transport phenomena in porous medium systems: 2. Foundation”, Advances in Water Resources, 28, 181-202, 2005.

96. C T Miller, W G Gray, “Thermodynamically constrained averaging theory approach for modelling flow and transport phenomena in porous medium systems: 4. Species transport fundamentals”, Advances in Water Resources, 31, 577-597, 2008.

97. C F Curtiss, R B Bird, “Multicomponent diffusion”, Industrial and Engineering Chemistry Research, 38(7), 2515-2522, 1999.

98. R B Bird, W E Stewart, E N Lightfoot, “Transport phenomena”, 2nd Edition, John Wiley & Sons, Inc. 2007.

99. R Taylor, R Krishna, “Multicomponent mass transfer”, John Wiley & Sons, Inc. 1993.

100. C R Wilke, “A viscosity equation for gas mixtures”, The journal of chemical physics”, 18, 4, 517-519, 1950.

101. P A Morgan, S D Robertson, J F Unsworth, “Combustion studies by thermogravimetric analysis. 1. Coal oxidation”, Fuel, V65, 1546-1551, 1986.

102. B R Stanmore, “Modeling the combustion behavior of petroleum coke”, Combustion and Flame, 83, 221-227, 1991.

103. M J Biggs, P K Agarwal, “The CO/CO2 product ratio for a porous char particle within an incipiently fluidized bed: a numerical study”, Chemical Engineering Science, Vol 52, No 6, p 941-952, 1997.

104. L Tognotti, J P Longwell and A F Sarofim, “The products of the high temperature oxidation of a single char particle in an electrodynamic balance”, Proceedings of the 23rd International Symposium on Combustion, The Combustion Institute, Pittsburgh, USA, p 1207, 1990.

105. O Levenspiel, “Chemical Reaction Engineering”, 3rd Edition, John Wiley & Sons, 1999.

106. H L Friedman, “Kinetics of Thermal Degradation of Char-forming Plastics from Thermogravimetry - Application to a Phenolic Plastic”, Journal of Polymer Science : Polymer Symposia, 6 [1], 183-195, 1964.

107. S Vyazovkin, A Lesnikovich, “Estimation of the Pre-exponential Factor in the Isoconversional Calculation of Effective Kinetic Parameters”, Thermochimica Acta, 128, 297-300, 1988.

108. S Vyazovkin, “Advanced Isoconversional Method”, Journal of Thermal Analysis, 49, 1493-1499, 1997.

109. S Vyazovkin, D Dollimore, “Linear and Nonlinear Procedures in Isoconversional Computation of the Activation Energy of Nonisothermal Reaction in Solids”, Journal of Chemical Information Computational Science, 36, 42-45, 1996.

110. P Budrugeac, “Differential Non-linear Isoconversional Procedure for Evaluating the Activation Energy of Non-Isothermal Reaction”, Journal of Thermal Analysis and Calorimetry, 68, 131-139, 2002.

111. A Khawam, D R Flanagan, “Role of Isoconversional Methods in Varying Activation Energies of Solid-state Kinetics, I. Isothermal Kinetic Studies”, Thermochimica Acta, 429, 93-102, 2005.

112. A Cuesta, A M Alonso, J M D Tascon, “Correlation between Arrhenius kinetic parameters in the reaction of different carbon materials with oxygen”, Energy & Fuels, 7, 1141-1145, 1993.

113. L H Sorensen, E Gjernes, T Jessen J Fjellerup, “Determination of reactivity parameters of model carbons, cokes and flame-chars”, Fuel, V7, 31-38, 1996.

114. F Lautzenhiser, E Amaya, “Self-constrained LTCC Tape”, American Ceramics Society Bulletin, 81 (10), 27-32, 2002.

115. M Godinho, Jr. E longo, E R Leite, “In Situ Observation of Glass Particle Sintering”, Journal of Chemical Education, 83(3), 410 – 413, 2006.

116. R K Bordia, G W Scherer, “On Constrained Sintering – I. Constitutive Model for a Sintering Body”, Acta Metallurgy, 36 (9), 2393-2397, 1988.

117. G W Scherer, “Viscous Sintering under a Uniaxial Load”, Journal of American Ceramic Society, 69 (9), C-206 – C-207, 1986.

118. J C Chang, J H Jean, “Self-constrained Sintering of Mixed Low-Temperature-Co-fired Ceramic Laminates”, Journal of American Ceramic Society, 89(3), 829-835, 2006.

119. W D Emmerich, J Hayhurst, E Kaisersberger, “High Temperature Dilatometer Study of Special Ceramics and their Sintering Kinetics”, Thermochimica Acta, 106, 71 – 78, 1986.

120. O Dernovsek, A Naeini, G Preu, W Wersing, M Eberstein, W A Schiller, “LTCC Glass-Ceramic Composites for Microwave Application”, Journal of the European Ceramic Society, 21, 1693-1697, 2001.

121. R Karmazin, O Dernovsek, N Ilkov, W Wersing, A Roosen, M Hagymasi, “New LTCC-hexaferrites by using Reaction Bonded Glass ceramics”, Journal of the European Ceramic Society, 25, 2029-2032, 2005.

122. P J Haines, “Principles of Thermal Analysis and Calorimetry”, The Royal Society of Chemistry, 2002.

123. J W Veldsink, R M J van Damme, G F Versteeg, W P M van Swaaij, ”The use of the dusty-gas model for the description of mass transport with chemical reaction in porous media”, The Chemical Engineering Journal, 115-125, 1995

124. E L Cussler, “Diffusion, mass transfer in fluid systems”, 2nd edition, Cambridge University Press, 2003.

125. M S Valipour, Y Saboohi, “Modelling of multiple noncatalytic gas-solid reactions in a moving bed of porous pellets based on finite volume method”, Heat and Mass Transfer, 43, 881-894, 2007.

126. W M Deen, “Analysis of transport phenomena”, Oxford University Press, 1998.

10:99. R Taylor, R Krishna, “Multicomponent mass transfer”, John Willey & Sons Inc, 1993.

127. A Faghri, Y Zhang, “Transport phenomena in multiphase systems”, Elsevier, 2006.

128. R Krishna, J A Wesselingh, “The Maxwell-stefan approach to mass transfer”, Chemical Engineering Science, 52 (6), 861-911, 1997.

129. K Matsui, H TsuJi, “An aerothermochemical analysis of solid carbon combustion in the stagnation flow accompanied by homogeneous CO oxidation”, Combustion and Flame, 70, 79-99, 1987.

130. S V Sotirchos, N R Amundson, “Diffusion and reaction in a char particle and in the surrounding gas phase. A continuous model”, Industrial Engineering and chemistry (Fundamental)”, 23, 191-201, 1984.

131. S V Sotirchos, N R Amundson, “Dynamic behavior of a porous char particle burning in an oxygen-containing environment, Part 1: Constant particle radius”, AIChE, 30(4), 537-549, 1984.

132. D W Green, “Perry’s Chemical Engineers’ Handbook, 8th edition, McGraw-Hill, 2007.

133. E N Fuller, P D Schettler, J C Giddings, “A new method for prediction of binary gas-phase diffusion coefficients”, Industrial Engineering of Chemistry”, 58 (5), 18-27, 1966

134. S C Carniglia, “Construction of the tortuosity factor from porosimetry”, Journal of catalysis, 102, 401-418, 1986.

135. S Lowell, J E Shields, M A Thomas, M Thommes, “Characterization of porous solids and powders: Surface area, pore size and density”, Kluwer Academic Publications, 2003.

136. DIPPR®801Database, AIChe.

137. X Zhang, E Bar-Ziv, “A novel approach to determine thermal conductivity of micron-sized fuel particles”, Combustion Science and Technology, 130, 79-95, 1997.

138. H K Versteeg, W Malalasekera, “An introduction to computational fluid dynamics: The finite volume method”, 2nd Edition, Pearson Education Limited, 2007.

139. Design guidelines for Heralock® HL2000 Materials System, Preliminary Guideline Release 1.0, Heraus Inc, Circuit Materials Division.

140. L Golonka, P Bembnowicz, D Jurkow, K Malecha, H Roguszczak, R Tadaszak, “ Low temperature co-fired ceramics (LTCC) Microsystems”, Optica Applicata, 41(2), 383-388, 2011

141. H Birol, T Maeder, C Jacq, G Corradini, Y Fournier, I Saglini, S Straessler, P Ryser, “Structuration of micro-fluidic devices based on low temperature co-fired ceramic (LTCC) technology”, EMPC 2005, Brugge, Belgium.

142. D J Sadler, R Changrani, P Roberts, C F Chou, F Zenhausern, ”Thermal management of bioMEMS: Temperaturecontrol for ceramic-based PCR and DNA detection devices”, IEEE Transactions on Components and Packaging Technologies, 26(2), 309-316, 2003.

143. D Plumlee, J Steciak, “Development and simulation of an embedded hydrogen peroxide catalyst chamber in low-temperature co-fired ceramics”, International Journal of Applied Ceramic Technology, 4(5), 406-414, 2007.

144. A Baker, C Randall, R Stewart, R Fantazier, F Wise, “Fabrication of a multilayered low-temperature cofired ceramic micro-plasma-generating device”, International Journal of Applied Ceramic Technology, 3(6), 413-418, 2006.

145. K Zhang, S K Chou, S S Ang, “A low temperature co-fired ceramic solid propellant microthruster for micropropulsion applications”, The 13th International Conference on Solid-State Sensors, Actuators and Microsystems, Seoul, Korea, 672-675, 2005.

146. H Birol, T Maeder, P Ryser, “Processing of graphite-based sacrificial layer for mircofabrication of low temperature co-fired ceramics (LTCC)”, Sensors and Actuators A, 130-131, 560-567, 2006.

147. A Simchi, F Petzoldt, “Cosintering of powder injection molding parts made from ultrafine WC-Co and 316L stainless steel powders for fabrication of novel composite structures”, Metallurgical and Materials transactions, 41A, 233-241, 2010.

148. Y Boonyongmaneerat, C A Schuh, “Contributions to the interfacial adhesion in co-sintered bilayers”, Metallurgical and Materials Transactions, 37A, 1435-1442, 2006.

149. C Pascal, A Thomazic, A A Zdziobek, J M Chaix, “Co-sintering and microstructural characterization of steel/cobalt base alloy biomaterials”, Journal of Material Science, 47, 1875-1886, 2012.

150. C H Hsueh, A G Evans, R M Cannon, R J Brook, “Viscoelastic stresses and sintering damage in heterogeneous powder compacts”, Acta Metallurgica, 34(5), 927-936, 1986.

151. A G Evans, “Consideration of inhomogeneity effects in sintering”, Journal of the American Ceramic Society, 65(10), 497-501, 1982.

152. J C Chang, J H Jean, “Camber development during the cofiring of bi-layers glass-based dielectric laminate”, Journal of American Ceramic Society, 88(5), 1165-1170, 2005.

153. P Suri, D F Heaney, R M German, “Defect-free sintering of two material powder injection molded components”, Journal of Materials Science, 38, 4875-4881, 2003.

154. C R Chang, J H Jean, “Effects of silver-paste formulation on camber development during the cofiring of a silver-based, low-temperature-cofired ceramic package”, Journal of American Ceramic Society, 81(11), 2805-2814, 1998.

155. J H Jean, C R Chang, “Cofiring kinetics and mechanisms of an Ag-metalized ceramic-filled glass electronic package”, Journal of American Ceramic Society, 80(12), 3084-3092, 1997.

156. J H Jean, T K Gupta, “Isothermal and nonisothermal sintering kinetics of glass-filled ceramics”, Journal of Materials Research, 7(12), 3342-3347, 1992.

157. D Plumlee, J Steciak, “Development and simulation of an embedded hydrogen peroxide catalyst chamber in low-temperature co-fired ceramics”, International Journal of Applied Ceramic Technology, 4(5), 406-414, 2007.

158. D J Sadler, R Changrani, P Roberts, C F Chou, F Zenhausern, “Thermal management of BioMEMS: Temperature control for ceramic-based PCR and DNA detection devices”, IEEE Transactions on Components and Packaging Technologies, 26(2), 309-316, 2003.

159. W K Jones, Y Liu, M Gao, “Micro heat pipe in low temperature cofire ceramic (LTCC) substrates”, 2002 Inter Society on Thermal Phenomena, 230-235, 2002.

APPENDIX A

Constants, Empirical Coefficients and Expressions for the Estimation of Physical Properties

---

(i) Molar Diffusion Volume

Species	Molar Diffusion Volume (m^3/mol)	Remarks
O_2	16.6 x 10^{-6}	Perry's Chemical Engineering Handbook [132]
CO_2	26.9 x 10^{-6}	
CO	18.9 x 10^{-6}	
N_2	17.9 x 10^{-6}	

(ii) Empirical coefficients and expressions for temperature-dependent vapour viscosity of gas species

$$\mu_i = \frac{AT^B}{1+{}^{C}/_{T}}, (Pa\ s)$$

Species	Coefficients			Remarks
	A	B	C	
O_2	1.1010x10^{-6}	0.5634	96.3	DIPPR®801Database [136]
CO_2	2.1480x10^{-6}	0.4600	290	
CO	1.1127x10^{-6}	0.5338	94.7	
N_2	6.5592x10^{-7}	0.6081	54.714	

(iii) Empirical coefficients and expressions for temperature-dependent Ideal Gas heat capacity of gas species

$$C_{pi} = A + B\left[\frac{{}^{C}/_{T}}{\sinh({}^{C}/_{T})}\right]^2 + D\left[\frac{{}^{E}/_{T}}{\cosh({}^{E}/_{T})}\right]^2, \left(\frac{J}{kmol\ K}\right)$$

Species (i)	Coefficients					Remarks
	A	B	C	D	E	
O_2	2.9103x10^4	1.0040x10^4	2.5265x10^3	9.3560x10^3	1.1538x10^3	DIPPR®801 Database [136]
CO_2	2.9370x10^4	3.4540x10^4	1.4280x10^3	2.6400x10^4	5.8800x10^2	
CO	2.9108x10^4	8.7730x10^3	3.0851x10^3	8.4553x10^3	1.5382x10^3	
N_2	2.9105x10^4	8.6149x10^3	1.7016x10^3	1.0347x10^2	9.0979x10^2	

(iv) Empirical coefficients and expressions for temperature-dependent vapour thermal conductivity of gas species

$$k_i = \frac{AT^B}{1+{}^{C}/_{T}+{}^{D}/_{T^2}}, \left(\frac{W}{m\,K}\right)$$

Species (i)	Coefficients				Remarks
	A	B	C	D	
O_2	4.4994×10^{-4}	0.7456	56.699		DIPPR®801 Database [136]
CO_2	3.69	-0.3838	964	1.8600×10^{6}	
CO	5.9882×10^{-4}	0.6863	57.130	501.92	
N_2	3.3143×10^{-4}	0.7722	16.323	373.72	

(v) Empirical coefficients and expressions for temperature-dependent specific heat capacity of carbon (graphite)

$$C_p = A + BT - \frac{C}{T^2}, \left(\frac{J}{mol\,K}\right)$$

Solid	Coefficients			Remarks
	A	B	C	
C (graphite)	11.1838	1.0950×10^{-2}	4.8911×10^{5}	Perry's Chemical Engineering Handbook [132]

(vi) Empirical coefficients and expressions for temperature-dependent heat conductivity of synthetic char (Spherocarb)

$$k_c = A + BT, \left(\frac{W}{m\,K}\right)$$

Solid	Coefficients		Remarks
	A	B	
C (Synthetic Char)	0.06	0.0011	Zhang et al, 1997 [137]

APPENDIX B

Measurement of Open Pore Size and Porosity by Mercury Porosimetry

---

Mercury porosimetry can be employed for pore size analysis in various fields such as chemical, pharmaceutical, paper, textile, petroleum and powder industries [B1-B4]. It relies on the physical phenomenon that a non-wetting liquid such as mercury will not penetrate into a relatively small pore without the application of sufficient pressure.

The relationship between the pore size and the applied pressure of the non-wetting liquid penetration for cylindrical pore geometry could be described by Washburn equation as,

$$D = -\frac{4}{P}\gamma\cos\theta \qquad \text{(B.1)}$$

where D is the open pore diameter (μm), P the pressure applied to force mercury into the pores (MPa) , γ the surface tension of mercury (N/m), and θ the contact angle between the mercury and the samples.

Mercury porosimetry which operates on the basis of the Washburn equation could provide analysis of mesopore to macropore, i.e. pore size ranging from about 1.8 nm to 200 μm. Its practical range is limited by the instrument pressure range. Thus, for micropore (less than 2 nm) size analysis, gas adsorption techniques may have to be

employed instead. The measurement obtained from a mercury porosimeter is highly dependent on the accuracy of the values of the contact angle employed in the Washburn equation. The typical range of contact angle for most of the surfaces is 112° to 142°. However, contact angle of 130° is frequently used if the actual wetting angle value is not available. Surface tension of the mercury varies with impurity; a widely used value is 0.480 N/m.

The open pore porosity measured by the mercury porosimetry is defined as the ratio of the pore volume over the apparent sample volume (bulk volume). The pore volume is determined directly by the total mercury intrusion volume and the bulk volume is obtained by the low-pressure intrusion (filling cycle) data at 3.45 kPa intrusion pressure.

$$\text{Open pore porosity} = \frac{Total\ mercury\ intrusion\ volume}{Bulk\ volume\ of\ sample} \quad \text{(B.2)}$$

For open pore size, the average pore size can be expressed as,

$$\text{Average open pore diameter} = \frac{4 * Total\ Intrusion\ Volume}{Total\ Pore\ Area} \quad \text{(B.3)}$$

Other physical parameters for mass transport in porous media analysis such as permeability, tortuosity and tortuosity factor [B1, B5-B6] could also be derived from the mercury porosimetry measurement.

Experimental Setup

Mercury porosimeter, Micromeritics AutoPore IV 9500, was used to measure the initial open pore size and porosity for both the carbon and LTCC tape before sintering but after debinding. The LTCC green sheets (150 mm x 150 mm) were first laminated under hydrostatic hot laminator at 100 kg/cm^2 and 348 K for 10 minutes into a 6-layer structure. The sample preparation for carbon tape was very much the same as the LTCC, but a single 0.25 mm (10 mil) tape was used. Both samples were cut into about 8 mm x 8 mm square for ensuring the consistency of geometrical shape and size. To determine the initial open pore size and porosity, samples were heated at 1 K/min to 773 K and soaked for 120 minutes for debinding.

Three measurements were repeated for each LTCC and carbon tape. The measurement steps strictly followed the recommended operating procedure by the instrument supplier [B7]. The detailed procedure of operation was lengthy and thus only the important aspects for measurement are described in the following sections.

i) Calibration of equipment

Major components such as pump, valves and transducers are periodically (yearly) calibrated and maintained by the Service Engineer.

ii) Blank and Sample Compression Corrections for Baseline Errors

For data accuracy and consistency, compression correction is to be conducted. Specific build-in formulae based on large number of blank runs from the accumulated data provided by the instrument supplier could be used for data correction. For validation, additional few blank runs would be useful. For the current investigation, blank run

correction adopted has the same penetrometer and parameters to be used in the measurement. The blank run reveals baseline error resulted by the compressibility and thermal effects of the mercury and penetrometer due to the high compression pressure of up to 60,000 psi. The blank run file or baseline file could then be stored and used for the correction of the actual run.

iii) Critical measurement parameters:

- Penetrometer: 3 ml type
    - Penetrometer Constant : 11.007 µl/pF
    - Stem Volume : 0.4120 ml
    - Penetrometer Volume : 3.6691 ml
    - Penetrometer weight: 61.8726 g
- Evaluation pressure : 50 µmHg
- Evaluation Time : 5 mins
- Mercury filling pressure : 0.5 psi
- Equilibration Time : 10 s
- Intrusion pressure : 0.1 - 60,000 psi
- Data recording : Intrusion/Extrusion volume and pressure

The typical intrusion and extrusion for an unfired LTCC tape is shown in Figure B-1.

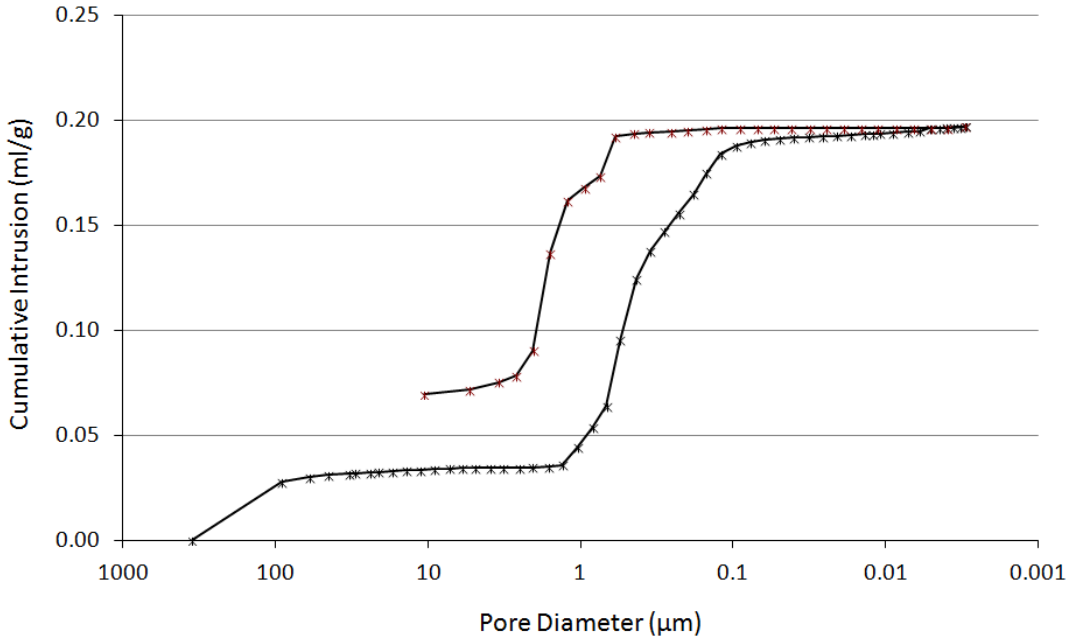

Figure B-1Typical mercury intrusion and extrusion curves for the 6-layer LTCC (after debinding).

References

B1. A J Katz and A H Thompson, Quantitative prediction of permeability in porous rock, Physical Review B, 34, 11, 8179-8181, 1986.

B2. V Nagy and L M Vas, Pore characteristic Determination with mercury porosimetry in polyester staple yarns, Fibres and Textiles in Eastern Europe, 13, 3, 21-26, 2005.

B3. S Westermarck, A M Juppo, K Koiranen and J Yliruusi, Mercury porosimetry of pharmaceutical powders and granules, Journal of Porous Materials, 5, 77-86, 1998

B4. C Orr, Jr, Application of mercury penetration to materials analysis, Powder B5. Technology, 3, 117-123, 1969/70.

B5. A J Katz and A H Thompson, Prediction of rock electrical conductivity from mercury injection measurements, Journal of Geophysical Research, 92, B1, 599-607, 1987

B6. P N Henrion, F Greenen and A Leurs, Knudsen diffusion in powders, Part II, Effect of pore size dribution on surface area obtained from diffusion measurements and correction with mercury porosimetry, Powder Technology, 16, 167-177, 1977.

B7. Micromeritics Inc. AutoPore IV 9500, Operating Manual.

Appendix C

Calibration of Thermal Gravitational Analyser (TGA)

TGA was used extensively for the determining of carbon burn-off kinetic parameters as reported in Chapter 3, Section 3.2. The TGA equipment employed, (TA instrument Q500) has an isothermal temperature accuracy and precision of ± 1 °C and ± 0.1 °C respectively, and weighting precision of ± 0.1 % and sensitivity of 0.1 μg. Though the instrument was fully calibrated during the installation at site, regular recalibration of temperature and weight are necessary to ensure that the data obtained are within the instrument accuracy and resolution. The TGA which was used for the analysis is recalibrated quarterly for temperature and weight.

Temperature Calibration

The temperature calibration technique recommended by TA instruments, which is based on ASTM standard E1582, is employed. The temperature calibration is based on the Curie point of paramagnetic metals. In this technique, a magnetic transition standard such as Nickel is heated in an Alumina sample pan. A magnet is placed outside the TGA furnace so that it is just below the sample pan as shown in Figure C-1. As the Nickel goes through its Curie transition temperature or Curie point, it loses its magnetism and causes a reduction in attraction to the magnet. In the TGA, it appears as a weight loss. The onset of the weight loss is known as the Curie point. Its value is used as the calibration offset as compared with the material's known Curie point temperature. List of materials which are listed in the ASTM standard is shown in Table C-1.

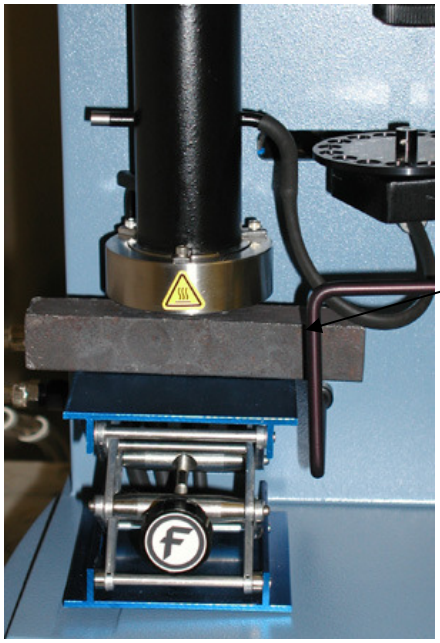

Figure C-1 Temperature calibration of TGA using Curie temperature of magnetic transition standard by placing a permanent magnetic under the sample pan [C2].

Table 1 List of standard magnetic transition materials for TGA temperature calibration [C1]

Metal	Curie Point (Magnetic) Transition, °C
ALUMEL™[A]	152.6
Nickel[B]	358.2
Nickel (83%)-Cobalt (17%)	554.4
Nickel (63%)-Cobalt (37%)	746.4
Nickel (37%)-Cobalt (63%)	930.8
Cobalt	1116

One or two magnetic transition standards encompass the experimental range are to be chosen. Use of multiple points of calibration will be required for best accurate results. The recent calibration check on the instrument is shown in Figure C-2. The Curie point measured is lower by 4 °C from the stated Curie point in the ASTM. There will be some deviation from the Curie point based on the purity and structure of the standards used. Thus the standard metals provided have to be tested and certified by authorised laboratory for the exact Curie point to be followed.

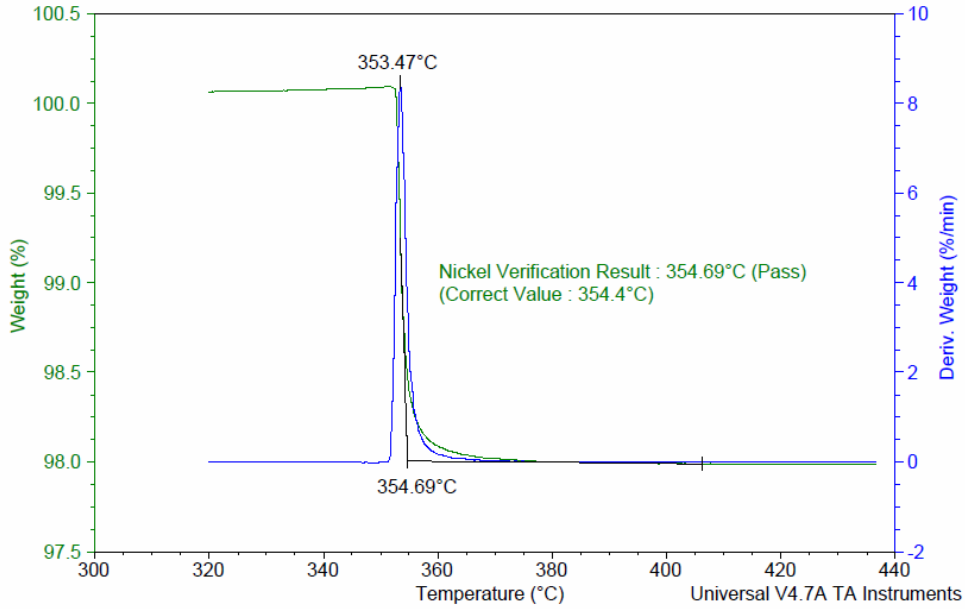

Figure C-2 TGA plot of most recent temperature calibration check before actual testing of Ni Curie point.

Weight Calibration

TA Q500 TGA's thermobalance works on a null-balance principle based on light intensity on a photo-detector system. The weight balance construction is shown in Figure C-3. At "zero" or "null" position, equal amounts of light received on the 2 photodiodes. If the balance arm moves out of the null position, an unequal amount of light intensity detected by the photodiodes causes a current applied to the meter movement to return the balance arm back to the zero position. The amount of current applied to the meter movement is proportional to the weight loss or gain resulted from the experiment. This amount of current has to be calibrated to relate to the weight scale. Since TGA is heavily based on weight change, weight calibration on TGA was performed quite regularly or at least once a month for normal operation usage.

Q500 has two weight ranges (200 mg & 1000 mg) to be calibrated. The range to be used is based on the sample weight to be tested. On screen instruction is useful when

the weight calibration routine is activated. However, the important points to be noted are summarized as follows,

- Both the sample pan (experiment pan) must be of the same type and size as the tare pan
- Use 100 mg class 1 standard weight for 200 mg range calibration
- Use 1000 mg class 1 standard weight for 1000 mg range calibration
- Run TGA weight calibration routinely
- Follow screen instructions to tare and mass calibrate using two calibration weights
- The calibrated weight information is automatically saved by the instrument.

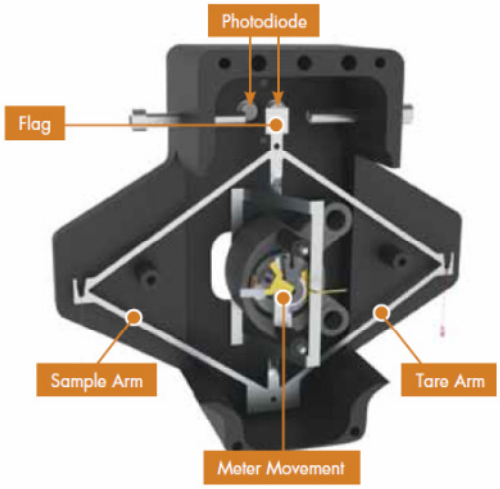

Figure C-3 Schematic drawing of TA instrument thermobalance mechanism using optical photodiode.

Calibration Check

Calcium Oxalate Monohydrate (CaC2O4•H2O) is a useful industrial compound used to make oxalic acid, organic oxalates, and glazes. It has good storage stability which does not adsorb humidity in normal laboratory storage condition. Its 3 distinct steps of

decomposition under heating in inert condition make it a good reference material for functionality check of a thermobalance.

The calibration check of Calcium Oxalate monohydrate was conducted regularly in the laboratory. The recent calibration check is shown in Figure C-4. The first mass loss corresponds to loss of water of hydration ($CaC_2O_4 \cdot H_2O \rightarrow CaC_2O_4 + H_2O$). The second mass loss corresponds to decomposition of dehydrated calcium oxalate to calcium carbonate and carbon monoxide ($CaC_2O_4 \rightarrow CaCO_3 + CO$). The last mass loss is due to the decomposition of calcium carbonate to calcium oxide and carbon dioxide ($CaCO_3 \rightarrow CaO + CO_2$). The mass loss at each step of decomposition was determined and compared to the theoretical values. The ceramic yield of CaO determined as residue is 38.2% which is near to the theoretical value of 38.4%.

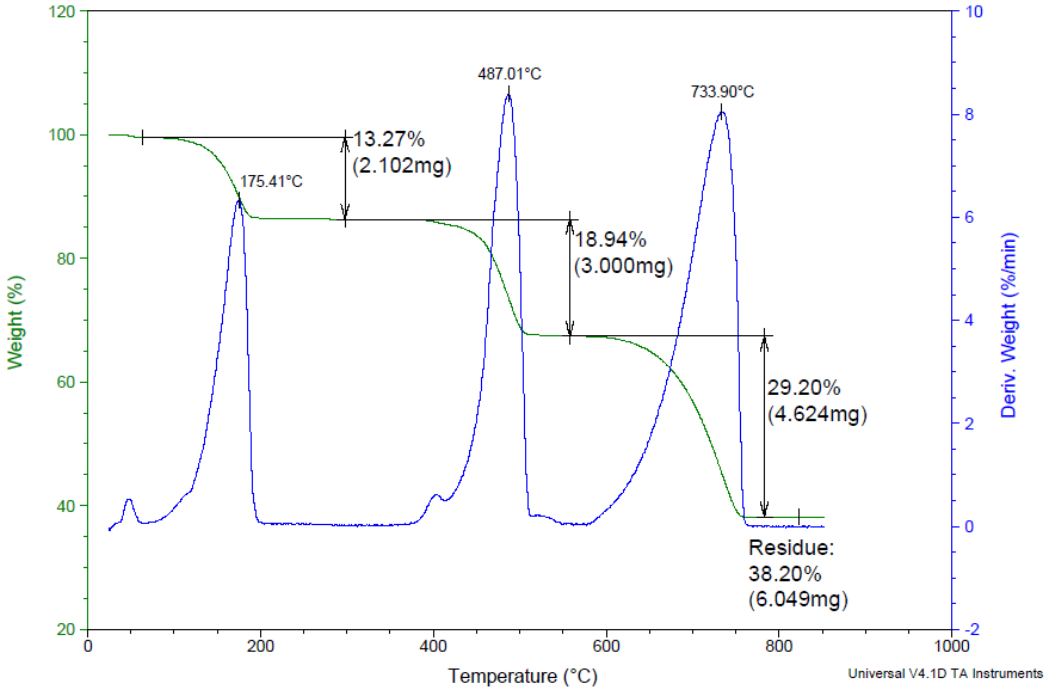

Figure C-4 Calibration check on Calcium Oxalate (sample mass = 15.84mg) with Nitrogen purging.

Baseline Correction

For best results, baseline correction for all experiments were conducted on the same empty sample pan at identical experimental parameters i.e. Air/Nitrogen flow rate, and heating programmed profile. With embedded carbon LTCC sample, correction was also performed with LTCC sample of the same layer configuration but without the embedded carbon layer. This is to further reduce or eliminate the possible polymer residue effect after debinding, which could affect the actual carbon burn-off kinetics.

References

C1. ASTM E1582-10, "Standard practice for calibration of temperature scale for thermogravimetry", American Society of Testing and Materials, 2010.

C2. TA instruments Inc, TGA Q500 User's Manual.

Appendix D

Calibration of Thermomechanical Analyser (TMA)

TMA was used extensively for the determining of LTCC sintering kinetic parameters as reported in Chapter 3, Section 3.2. The TMA equipment employed is TA instruments Q400 TMA. The basic construction of the Q400 TMA is shown in Figure D-1. It has an isothermal temperature precision of ± 1 °C, a length change precision of ± 0.1 % and sensitivity of 15 nm, with a force resolution of 0.001 N. Though the instrument was fully calibrated during the installation at site, regular temperature and length change recalibration are necessary to ensure that the data recorded is within the instrument accuracy and resolution. The following calibrations are necessary for the proper setup of TMA for accurate measurements.

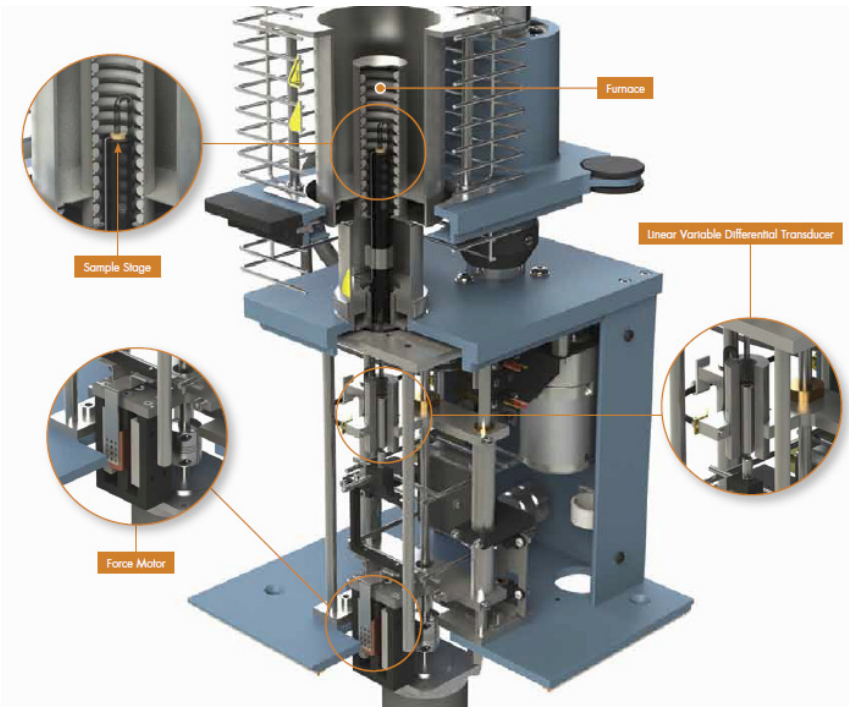

Figure D-1 Construction of TA Instruments, Q400 TMA [D1].

Probe Calibration

TMA equips with different probes which are shown in Figure D-2. Probe calibration is paramount for any probe change before any experiment. In fact, the instrument will not start if a probe change without probe calibration was detected. This procedure is used to calibrate the Linear Variable Differential Transducer (LVDT) for zero length of the probe's compliance and adjust force calibration factor to compensate for the mass of various probe types.

Figure D-2 Various standard probes available for the TMA [D1].

Force Calibration

Force calibration is necessary as TMA apply load on the specimen during the experiment. The load applied on the specimen could be in the range of 0.001 N to 2 N. Force calibration was done using three different mass values (0, 50, and 100 g) with any standard probes available. In the current investigation, the standard expansion probe for the LTCC sintering kinetics analysis was used for the calibration. The first calibration point is 0 g. Standard weights other than the recommended weights are also possible depending on the specific requirement in the experiments. For example, a 10 g

standard weight for force calibration will be appropriate if only low force will be used in subsequent experiments.

Temperature Calibration

Temperature calibration is based on ASTM E1363 [D2]. A temperature standard such as Indium is heated through its melting point. The recorded melting point of this standard is compared to the known melting point of the standard reference materials. The difference of the melting points is used for temperature calibration.

Multiple point temperature calibration was used in the current investigation. Two standard materials were selected from the list of standard materials recommended by ASTM E1363, see Table D-1. Indium and Aluminium were used for the calibration which covers the temperature range of the current investigation. The calibration TMA curve of Indium is shown in Figure D-3. This calibration should be performed when the sample thermocouple is changed and/or when the temperature range of interest is changed. To protect the stage from amalgamation with the metal, a thin quartz is placed between the stage and the metal standard.

Table D-1 recommended metal standard for TMA tempertaure calibration [D1].

Calibration Material[B]	Melting Temperature	
	(°C)	(K)
Mercury	−38.8344	234.3156
Water	0.01	273.16
Gallium	29.7646	302.9146
Indium	156.5985	429.7485
Tin	231.928	505.078
Zinc	419.527	692.677
Aluminum	660.323	933.473
Silver	961.78	1234.93
Gold	1064.18	1337.33
Copper	1084.62	1357.77

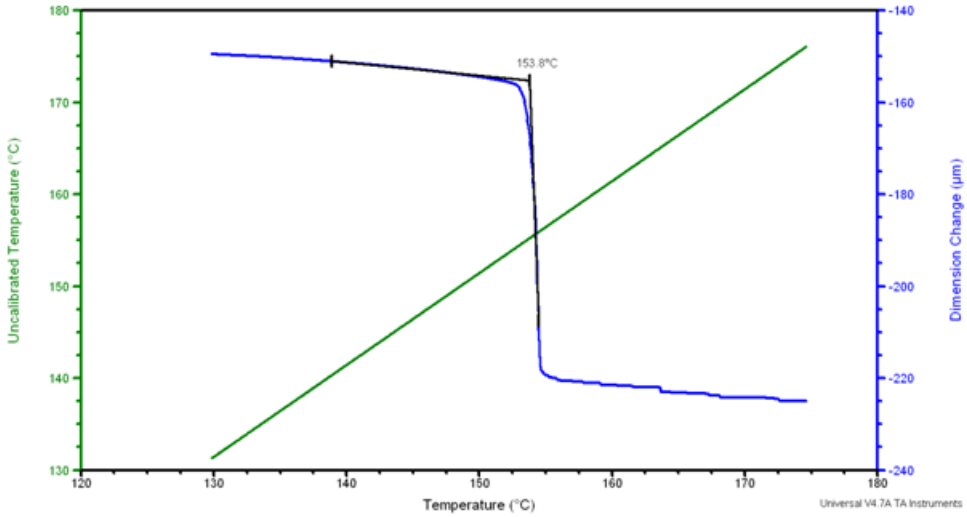

Figure D-3 Temperature calibration using melting point of Indium.

Cell Constant Calibration

Length change calibration in TMA was done by conducting a Coefficient of Thermal Expansion (CTE) measurement on a known standard material. This calibration procedure is referring as cell constant calibration. The test method of measuring CTE of a solid material was based on ASTM E2113 [D3] and ASTM 831[D4]. The calibration specimen used for this calibration is a reference Aluminium and the calibration TMA curve is shown in Figure D-4. The cell constant is calculated by dividing the actual CTE of the standard by the measured CTE. The cell constant calculated is then stored in the instrument control software as cell constant calibration factor.

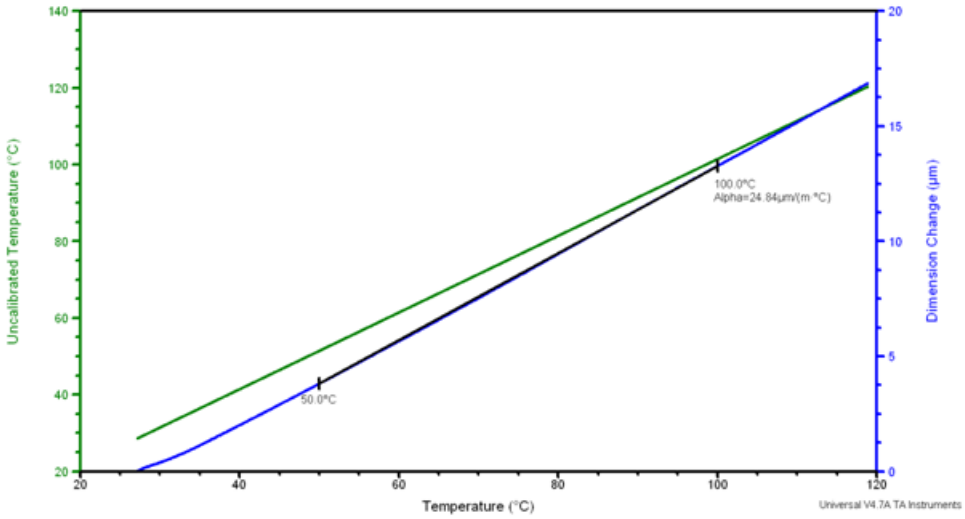

Figure D-4 CTE measurement of a 8 mm Aluminium standard.

Baseline Corrections

The TMA experiment for LTCC sample was conducted by placing 2 thin quartz discs between the stage and probe to prevent them from possible fusing together at high temperature. Thus, for best results, baseline corrections for all experiments were conducted on the same thin quartz discs (without LTCC sample) at the identical experimental parameters to eliminate possible effect from the length change resulted from the thin quartz at high temperature.

References

D1. TA instruments Inc, TMA Q400 User's Manual.

D2. ASTM E1363, "Standard test method for temperature calibration of thermomechanical analyzer", American Society of Testing and Materials, 2008.

D3. ASTM E2113, "Standard test method for length change calibration of thermomechanical analyzer", American Society of Testing and Materials, 2009.

D4. ASTM E831, “Standard test method for linear thermal expansion of solid materials by thermomechanical analysis” American Society of Testing and Materials, 2012.